

박사학위논문

Ph.D. Dissertation

페이즈 필드 모델을 위한 효율적인
수치적 방법 개발

Development of efficient numerical methods
for the phase field model

2023

김기환 (金起煥 Kim, Gihwan)

한국과학기술원

Korea Advanced Institute of Science and Technology

박 사 학 위 논 문

페이즈 필드 모델을 위한 효율적인
수치적 방법 개발

2023

김 기 환

한 국 과 학 기 술 원

기계항공공학부/기계공학과

페이지 필드 모델을 위한 효율적인 수치적 방법 개발

김 기 환

위 논문은 한국과학기술원 박사학위논문으로
학위논문 심사위원회의 심사를 통과하였음

2022년 09월 23일

심사위원장 이 필 승 (인)

심사위원 윤 정 환 (인)

심사위원 김 성 수 (인)

심사위원 유 승 화 (인)

심사위원 김 산 (인)

Development of efficient numerical methods for the phase field model

Gihwan Kim

Advisor: Phill-Seung Lee

A dissertation/thesis submitted to the faculty of
Korea Advanced Institute of Science and Technology in
partial fulfillment of the requirements for the degree of
Doctor of Philosophy in Mechanical Engineering

Daejeon, Korea
September 23, 2022

Approved by

Phill-Seung Lee
Professor of Mechanical Engineering

The study was conducted in accordance with Code of Research Ethics¹⁾.

1) Declaration of Ethical Conduct in Research: I, as a graduate student of Korea Advanced Institute of Science and Technology, hereby declare that I have not committed any act that may damage the credibility of my research. This includes, but is not limited to, falsification, thesis written by someone else, distortion of research findings, and plagiarism. I confirm that my dissertation contains honest conclusions based on my own careful research under the guidance of my advisor.

DME

김기환. 페이즈 필드 모델을 위한 효율적인 수치적 방법 개발. 기계공학과. 2023년. 81+vii 쪽. 지도교수: 이필승. (영문 논문)

Gihwan Kim. Development of efficient numerical methods for the phase field model. Department of Mechanical Engineering. 2023. 81+vii pages. Advisor: Phill-Seung Lee. (Text in English)

초 록

파괴 해석을 위한 다양한 수치적 방법들이 제안됐지만, 여러 문제점들로 인해 한계에 직면하였고, 최근 페이즈 필드 모델이 새롭게 제시되었다. 그러나, 균열 선단 근처의 미세 격자로 인한 급격한 자유도 증가와 뉴턴-랩슨 방법과 같은 반복적 해법으로 인해 높은 전산 비용을 요구한다. 다양한 적응적 격자 세분화 기법들이 페이즈 필드 모델에 적용되었지만 전산 효율성 개선은 여전히 해결해야 할 문제점으로 남아있다.

본 학위 논문에서는 취성 파괴를 위한 페이즈 필드 모델의 전산 효율성을 향상시키기 위한 새로운 수치적 방법을 제안한다. 먼저, 계산 시간을 줄이기 위해, 적응적 업데이트 기법을 제안한다. 전체 영역은 균열 선단 주위의 영역과 나머지 영역으로 나뉜다. 균열 선단 주위의 영역의 구조적 특성을 자주 업데이트하고 나머지 영역의 구조적 특성을 간간히 업데이트함으로써, 전산 효율성을 개선시킨다. 추가적인 효율성 향상을 위해 변절점 유한 요소를 사용한 적응적 격자 세분화가 적용된다. 제안된 방법은 다양한 수치 예제들을 통해 계산 비용이 크게 절감됨을 보여준다.

또한, 유령 절점 방법을 사용한 격자 조대화도 제안된다. 균열 선단이 이미 지나간 영역의 미세 격자는 유령 절점 방법이 적용된 성긴 격자로 대체 되며, 이로 인해 자유도가 급격히 감소된다. 여러 수치 예제들을 통하여 제안된 방법의 성능이 검증된다. 제안된 방법들은 페이즈 필드 모델을 사용한 파괴 해석에 효과적으로 활용 될 것으로 기대한다.

핵심 낱말 페이즈 필드 모델, 유한요소법, 취성 파괴, 균열 진전, 적응적 업데이트, 적응적 격자 세분화, 변절점 유한 요소, 유령 절점 방법, 격자 조대화

Abstract

Various numerical methods for fracture analysis have been proposed, but they faced limitations due to several problems, and a new phase field model was recently proposed. However, it requires a high computational cost due to the rapid increase in degrees of freedom caused by the fine mesh near the crack tip and due to iterative solution procedure such as the Newton-Raphson method. Although various adaptive mesh refinement schemes have been applied to the phase field model, improvement of the computational efficiency still remains a problem

to be solved.

In this dissertation, new numerical methods to improve the computational efficiency of the phase field model for brittle fracture are proposed. First, in order to reduce the computation time, an adaptive update scheme is proposed. The whole domain is divided into the domain around the crack tip and the rest domain. By frequently updating the structural properties of the domain around the crack tip and occasionally updating the structural properties of the remaining domain, the computational efficiency is improved. For further efficiency improvement, the adaptive mesh refinement scheme using variable-node finite elements is applied. The proposed method shows that the computational cost is greatly reduced through various numerical examples.

In addition, mesh coarsening using the phantom-node method is also proposed. The fine mesh in the domain where the crack tip has already passed is replaced by the coarse mesh to which the phantom-node method is applied, which drastically reduces the degrees of freedom. The performance of the proposed method is verified through several numerical examples. It is expected that the proposed methods will be effectively utilized for fracture analysis using the phase field model.

Keywords Phase field model, Finite element method, Brittle fracture, Crack propagation, Adaptive update, Adaptive mesh refinement, Variable-node finite element, Phantom-node method, Adaptive mesh coarsening

Contents

Contents	i
List of Tables	iii
List of Figures	iv
Chapter 1. Introduction	1
1.1. Research background	1
1.2. Research objective	2
Chapter 2. Phase field model	3
2.1. Phase field approximation	3
2.2. Finite element discretization	6
Chapter 3. Domain decomposition	11
3.1. Crack tip domain	11
3.2. Domain of crack propagation path	11
3.3. Near-tip domain	12
Chapter 4. Adaptive mesh refinement	13
4.1. Variable-node elements	13
4.2. Mesh connection	14
4.3. Adaptive mesh refinement during crack propagation	15
4.4. Hole boundary handling procedure	16
Chapter 5. Adaptive update	17
5.1. Motivation	17
5.2. Key idea	17
5.3. Numerical examples	19
5.3.1. Single-edge notched tension problem	20
5.3.2. Single-edge notched shear problem	25
5.3.3. Symmetric three-point bending problem	29
5.3.4. Notched plate with three holes	32
5.3.5. Single-edge notched shear plate with diamond-shaped holes	36
5.3.6. L-shaped panel	39
5.3.7. Single-edged notched branching problem	43
Chapter 6. Mesh coarsening using the phantom-node method in the phase field model	48
6.1. Review of the phantom-node method	48

6.2. Mesh coarsening using the phantom-node method.....	50
6.3. Numerical examples	52
6.3.1. Single-edged notched tension problem.....	53
6.3.2. L-shaped panel.....	56
6.3.3. Notched cruciform plate	59
6.3.4. Double-edged notched tension problem	63
Chapter 7. Conclusions.....	67
Bibliography.....	68
Appendix A. Phase field formulations.....	76
A.1. Isotropic formulation	76
A.2. Anisotropic formulation.....	76
A.3. Hybrid formulation	77
Appendix B. Patch test of variable-node finite elements.....	78
Appendix C. Study on the update parameter	79
Appendix D. Study on the critical damage parameter in the case of crack initiation	81

List of Tables

Table 5.1. Specific computation times required for the single-edge notched tension problem in Fig. 5.2 for the local mesh refinement scheme.....	24
Table 5.2. Specific computation times required for the single-edge notched tension problem in Fig. 5.2 for the adaptive mesh refinement scheme.....	24
Table 5.3. Computation times required for the single-edge notched shear problem in Fig. 5.5.....	28
Table 5.4. Computation time ratios for the single-edge notched shear problem in Fig. 5.5.....	28
Table 5.5. Computation times required for the symmetric three-point bending problem in Fig. 5.9.....	32
Table 5.6. Computation times required for the notched plate with three holes in Fig. 5.12.	36
Table 5.7. Computation times required for the single-edge notched shear with diamond-shaped holes in Fig. 5.17.	39
Table 5.8. Computation times required for the L-shaped panel in Fig. 5.20.....	43
Table 5.9. Computation times required for the single-edge notched branching problem in Fig. 5.24.	47
Table 6.1. Normalized computation times required for the single-edge notched tension problem in Fig. 6.5. (Case 1) Adaptive mesh refinement + Adaptive update, (Case 2) Adaptive mesh refinement+ Adaptive update+ Mesh coarsening.....	56
Table 6.2. Normalized computation times required for the L-shaped panel in Fig. 6.9. (Case 1) Adaptive mesh refinement + Adaptive update, (Case 2) Adaptive mesh refinement+ Adaptive update+ Mesh coarsening.	59
Table 6.3. Normalized computation times required for the notched cruciform plate in Fig. 6.12. (Case 1) Adaptive mesh refinement + Adaptive update, (Case 2) Adaptive mesh refinement+ Adaptive update+ Mesh coarsening.	62
Table 6.4. Normalized computation times required for the double notched tension problem in Fig. 6.19. (Case 1) Adaptive mesh refinement + Adaptive update, (Case 2) Adaptive mesh refinement+ Adaptive update+ Mesh coarsening.....	65
Table 6.5. Relative computation times for five analysis cases in the double-edged notched tension problem.	65
Table C.1. Computation times required according to the update parameter η for the notched plate with three holes.....	79

List of Figures

Fig. 2.1. Schematics of a linear elastic body Ω including (a) a sharp crack surface Γ , and (b) a diffusive crack surface $\Gamma_0(\phi)$	3
Fig. 2.2. Crack topologies in (a) the sharp crack model and (b) the diffusive crack model.....	4
Fig. 2.3. Numerical procedure for the phase field model.	10
Fig. 3.1. Identification of the mesh refinement domains (a) at time t and (b) at time $t + \Delta t$. The crack tip domain is colored yellow, the domain of the crack propagation path is colored red, and the near-tip domain is colored green.	12
Fig. 4.1. Examples of variable-node elements: (a) 11-node element, (b) 18-node element, and (c) 25-node element.	13
Fig. 4.2. Use of variable-node elements to connect the coarse and fine meshes.	14
Fig. 4.3. Mesh geometry and domain Ω' divided into Ω'_{cm} , Ω'_{fm} and Ω'_{m}	14
Fig. 4.4. Mesh geometry of adaptive mesh refinement (a) at time t and (b) at time $t + \Delta t$. The crack tip domain is colored yellow, the domain of the crack propagation path is colored red, and the near-tip domain is colored green.	15
Fig. 4.5. Schematics of the hole boundary handling procedure: (a) a domain Ω with a hole boundary Γ_h , (b) mesh geometry when Ω'_m penetrates into Ω_h , (c) mesh geometry at time t , and (d) mesh geometry at time $t + \Delta t$	16
Fig. 5.1. Near-tip domain Ω'_m and domain far from the crack tip Ω'_f . While the structural properties in Ω'_m change rapidly during the simulation, those in Ω'_f rarely vary.....	17
Fig. 5.2. Single-edge notched tension problem: (a) geometry and boundary conditions, (b) mesh used for the local mesh refinement scheme, (c) initial mesh used for the adaptive mesh refinement scheme, and (d) load history curve.	21
Fig. 5.3. Mesh geometries and crack patterns for the single-edge notched tension problem when (a) $\delta = 0.005399$ mm (3452 nodes and 3256 elements), (b) $\delta = 0.005549$ mm (4103 nodes and 3886 elements), and (c) $\delta = 0.005859$ mm (5699 nodes and 5398 elements).	22
Fig. 5.4. Load-displacement curves on the single-edge notched tension problem: (a) when the adaptive update scheme is used and when it is not used, and (b) when compared with previous results.	23
Fig. 5.5. Single-edge notched shear problem: (a) geometry and boundary conditions, (b) mesh used for the local mesh refinement scheme, and (c) initial mesh used for the adaptive mesh refinement scheme.	25
Fig. 5.6. Mesh geometries and crack patterns for the single-edge notched shear problem when (a) $\delta = 0.00869$ mm (3578 nodes and 3382 elements), (b) $\delta = 0.01129$ mm (4838 nodes and 4579 elements) and (c) $\delta = 0.01299$ mm (7225 nodes and 6847 elements).	26
Fig. 5.7. Load-displacement curves on the single-edge notched shear problem: (a) when the adaptive update scheme is used and when it is not used, and (b) when compared with previous results.	27
Fig. 5.8. Computational efficiency curves for the single-edge notched shear problem in Fig. 5.5.....	29
Fig. 5.9. Symmetric three-point bending problem: (a) geometry and boundary conditions, (b) mesh geometry for	

the local mesh refinement scheme, (c) initial geometry for the adaptive mesh refinement scheme, and (d) load history curve.	30
Fig. 5.10. Mesh geometries and crack patterns for the symmetric three-point bending problem when (a) $\delta = 0.04699$ mm (2615 nodes and 2442 elements), (b) $\delta = 0.04799$ mm (3133 nodes and 2946 elements) and (c) $\delta = 0.05439$ mm (3798 nodes and 3576 elements).	30
Fig. 5.11. Load-displacement curves on the symmetric three-point bending problem: (a) when the adaptive update scheme is used and when it is not used, and (b) when compared with previous results.	31
Fig. 5.12. Notched plate with three holes: (a) geometry and boundary conditions, (b) mesh geometry for the local mesh refinement scheme, and (c) initial mesh geometry for the adaptive mesh refinement scheme.	33
Fig. 5.13. Mesh geometries and crack patterns for the notched plate with three holes when (a) $\delta = 0.379$ mm (4794 nodes and 4554 elements), (b) $\delta = 0.599$ mm (7699 nodes and 7200 elements), and (c) $\delta = 1.039$ mm (6985 nodes and 6633 elements).	34
Fig. 5.14. Load-displacement curves on the notched plate with three holes when the adaptive update scheme is used and when it is not used.	35
Fig. 5.15. Load-displacement curves on the notched plate with three holes when compared with results in previous studies.	35
Fig. 5.16. Calculated crack path compared with the numerical and experimental results by Ambati et al. [60]. The numerical solution is obtained by using the adaptive update scheme with the adaptive mesh refinement scheme.	36
Fig. 5.17. Single-edge notched shear plate with diamond-shaped holes: (a) geometry and boundary conditions, (b) mesh geometry for the local mesh refinement scheme, and (c) initial geometry for the adaptive mesh refinement scheme.	37
Fig. 5.18. Mesh geometries and crack patterns for the single-edge notched shear plate with diamond-shaped holes when (a) $\delta = 0.01139$ mm (6933 nodes and 6457 elements), (b) $\delta = 0.01249$ mm (7941 nodes and 7465 elements) and (c) $\delta = 0.01449$ mm (12771 nodes and 12064 elements).	38
Fig. 5.19. Load-displacement curves on the single-edge notched shear plate with diamond-shaped holes when the adaptive update scheme is used and when it is not used.	38
Fig. 5.20. L-shaped panel: (a) geometry and boundary conditions, (b) mesh geometry for the local mesh refinement scheme and (c) initial mesh geometry for the adaptive mesh refinement scheme.	40
Fig. 5.21. Mesh geometries and crack patterns for the L-shaped panel when (a) $\delta = 0.0995$ mm (3847 nodes and 3718 elements), (b) $\delta = 0.3245$ mm (5982 nodes and 5734 elements), and (c) $\delta = 0.4495$ mm (10224 nodes and 9830 elements).	41
Fig. 5.22. Load-displacement curves on the L-shaped panel: (a) when the adaptive update scheme is used and when it is not used, and (b) when compared with previous results.	42
Fig. 5.23. Calculated crack path compared with the experimental result [71]. The numerical solution is obtained by using the adaptive update scheme with the adaptive mesh refinement scheme.	43
Fig. 5.24. Single-edge notched branching problem: (a) geometry and boundary conditions, (b) mesh geometry for the local mesh refinement scheme and (c) initial mesh geometry for the adaptive mesh refinement scheme.	44
Fig. 5.25. Mesh geometries and crack patterns for the single-edge notched branching problem when (a) $\delta_0 = 0.0099$ mm (5634 nodes and 5441 elements), (b) $\delta_0 = 0.0299$ mm (12830 nodes and 12245 elements), and (c) $\delta_0 = 0.0849$ mm (22679 nodes and 21632 elements).	45
Fig. 5.26. Crack paths calculated by (a) the full model and, (b) the half model with symmetric boundary conditions	

compared with those by the full models by Muixi et al. in (c) Ref. [44] and (d) Ref. [46]. The crack paths with the proposed method are obtained by using the adaptive update scheme with the adaptive mesh refinement scheme.	46
Fig. 5.27. Load-displacement curves on the single-edge notched branching problem when the adaptive update scheme is used and when it is not used.	47
Fig. 6.1. Two superimposed elements having (E1 and E2) two real domains (Ω_R^{E1} and Ω_R^{E2}) and two virtual domains (Ω_V^{E1} and Ω_V^{E2}), respectively.	49
Fig. 6.2. Mesh geometries: (a) before and (b) after mesh coarsening.	50
Fig. 6.3. Schematics of mesh connection modeled by the phantom-node method and phase field model, respectively.	51
Fig. 6.4. Schematics of superimposed elements model by phantom-nodes.	51
Fig. 6.5. Single-edge notched tension problem: (a) geometry and boundary conditions, (b) initial mesh geometry, and (c) load history curve.	53
Fig. 6.6. Mesh geometries and crack patterns for the single-edge notched tension problem when (a) $\delta = 0.00555$ mm, (b) $\delta = 0.0057$ mm, and (c) $\delta = 0.0059$ mm.	54
Fig. 6.7. Mesh geometries: (a) without and (b) with mesh coarsening.	55
Fig. 6.8. Load-displacement curves on the single-edge notched tension problem.	55
Fig. 6.9. L-shaped panel: (a) geometry and boundary conditions and (b) initial mesh geometry.	56
Fig. 6.10. Mesh geometries and crack patterns for the L-shaped panel when (a) $\delta = 0.35$ mm, (b) $\delta = 0.4$ mm, and (c) $\delta = 0.95$ mm.	57
Fig. 6.11. Load-displacement curves on the L-shaped panel.	58
Fig. 6.12. Calculated crack path compared with the experimental result [71]. The numerical solution is obtained by mesh coarsening with the adaptive update and mesh refinement schemes.	58
Fig. 6.13. Histories of the total number of degrees of freedom for the L-shaped panel.	59
Fig. 6.14. Notched cruciform plate: (a) geometry and boundary conditions, (b) initial mesh geometry, and (c) load history curve.	60
Fig. 6.15. Mesh geometries and crack patterns for the notched cruciform plate when (a) $\delta = 0.02625$ mm, (b) $\delta = 0.02645$ mm, and (c) $\delta = 0.02685$ mm.	61
Fig. 6.16. Load-displacement curves on the notched cruciform plate.	61
Fig. 6.17. Calculated crack path compared with the numerical results by Hirshikesh et al. [79] and Mandal et al. [80]. The numerical solution is obtained by mesh coarsening with the adaptive update and mesh refinement schemes.	62
Fig. 6.18. Histories of the total number of degrees of freedom for the notched cruciform plate.	62
Fig. 6.19. Double-edged notched tension problem: (a) geometry and boundary conditions, (b) initial mesh geometry, and (c) load history curve.	63
Fig. 6.20. Mesh geometries and crack patterns for the double-edged notched tension problem when (a) $\delta = 0.0121975$ mm, (b) $\delta = 0.0125225$ mm, and (c) $\delta = 0.0134725$ mm.	64
Fig. 6.21. Load-displacement curves on the double-edged notched tension problem.	64

Fig. 6.22. Calculated crack paths in Case 1 (Adaptive mesh refinement + Adaptive update) and Case 2 (Adaptive mesh refinement + Adaptive update + Mesh coarsening).....	64
Fig. 6.23. Mesh geometries used for five analysis cases in Table 6.5: (a) the local mesh refinement and (b) the adaptive mesh refinement.	66
Fig. B.1. Patch test of variable-node finite elements: (a) geometry and boundary conditions and (b) mesh geometries for (b) 11-node, (c) 18-node and (d) 25-node variable-node finite elements.	78
Fig. B.2. Stress distributions of the patch test for (a) 11-node, (b) 18-node and (c) 25-node variable-node finite elements.	78
Fig. C.1. Load-displacement curves according to the update parameter η for the notched plate with three holes.	80
Fig. D.1. Load-displacement curves for the L-shaped panel for four different ϕ_c from 0.1 to 0.4.	81

Chapter 1. Introduction

1.1. Research background

Fracture is one of the most important phenomena in solid and structural mechanics because it can lead to catastrophic failures. Understanding and analyzing fracture behaviors are fundamental to avoiding such failures. Griffith [1] and Irwin [2] played a leading role in understanding the fracture behavior of materials from an engineering point of view. They introduced a term called “energy release rate” to represent the fracture behavior in thermodynamic aspects; thus, Linear Elastic Fracture Mechanics (LEFM), the foundation of fracture mechanics, was born.

In addition to the theoretical development of fracture mechanics, many researchers have tried to simulate fracture behaviors through numerical analysis. The main tool used for fracture analysis has been the finite element method (FEM) [3-13]. The finite element analysis of crack propagations requires re-meshing near the crack tip for the modeling of moving crack tips. This is a very tedious process with high computational cost. Alternative methods were developed to deal with discontinuities caused by cracks without re-meshing: the element free Galerkin method (EFGM) [14-16], the extended finite element method (XFEM) [17-19], the phantom node method [20, 21], and various other methods [22, 23]. However, since explicitly tracking the crack surface is a very difficult task, there are still challenges in dealing with complex and arbitrary crack paths.

The phase field model (PFM) based on the variational approach has been proposed [24-28]. Recently, it has been applied on problems of ductile fracture, [29] dynamic fracture [30] and so on [31, 32]. It is capable of handling complex fracture behaviors such as crack initiation and branching. Using a damage parameter as a nodal degree of freedom allows the model to easily handle complex crack behaviors without crack tracking algorithms. This is indeed the most advantageous feature of the phase field model. However, it requires an iterative procedure to solve nonlinear equations such as Newton-Raphson method, and mesh refinement to deal with high gradient values in the phase field transition zone, which largely increase the computational cost.

To resolve this problem, various adaptive mesh refinement schemes have been successfully employed in the phase field model [33-47]. In the refinement schemes, displacement compatibility from coarse mesh to fine mesh should be satisfied. At non-matching mesh interface between coarse and fine meshes, the compatibility is enforced using

Nitsche's method [44, 46], the hybridizable discontinuous Galerkin method [45] and the global-local approach [47]. Also, mesh transitions can be implemented adopting layers of triangular and quadrilateral elements [36, 41-43]. A multiscale approach could be useful [38-39].

1.2. Research objective

In this dissertation, we focus on further improving the computational efficiency of the phase field model for brittle fracture. We propose the adaptive update scheme. The computational efficiency can be greatly improved without mesh refinement, and can be further improved when used in conjunction with the adaptive mesh refinement schemes. In this numerical scheme, the entire domain is divided into two domains: one near the crack tip and one far from the crack tip. Since structural properties such as stiffness, strain energy, and damage rarely vary in the domain far from the crack tip, those properties are occasionally updated in the iterative solution procedure.

To maximize the computational efficiency, the local and adaptive mesh refinement schemes can be adopted together. The adaptive update scheme reduces computation time by 40% to 50% while maintaining the desired solution accuracy. To implement the adaptive mesh refinement scheme in this study, the use of variable-node elements [48, 49] is adopted for the mesh transition [50-55]. A fine mesh near the crack tip is directly connected to the coarse mesh far from the crack tip through only one layer of variable-node elements. The use of variable-node elements is effective compared to other adaptive mesh refinement schemes in crack tip modeling [33-47]. We also introduce a methodology for the adaptive mesh refinement when the crack tip encounters a hole.

In the following sections, the formulation of the phase field model is reviewed in brief. Then, the adaptive mesh refinement scheme using variable-node elements and the adaptive update scheme are presented. The effectiveness of the proposed numerical schemes is demonstrated through several numerical examples. Finally, conclusions are drawn.

The paper including the works in Chapter 2, 3, 4 and 5 is accepted and will be appear in Ref. [48]. In this dissertation, the contents contained in Ref. [48] have been written with minor modifications.

Chapter 2. Phase field model

In this section, we briefly review the formulation of the phase field model proposed by Miehe et al. [27] from the variational approach to numerical implementation. In the following sections, t is a variable representing the incremental load step instead of the actual time generally used in dynamic analysis [4] because quasi-static analysis is considered in this study.

2.1. Phase field approximation

A linear elastic body of volume V including a sharp crack surface Γ is considered as shown in Fig. 2.1(a). In Fig. 2.1, S_d and S_f indicate the displacement and force boundaries, respectively.

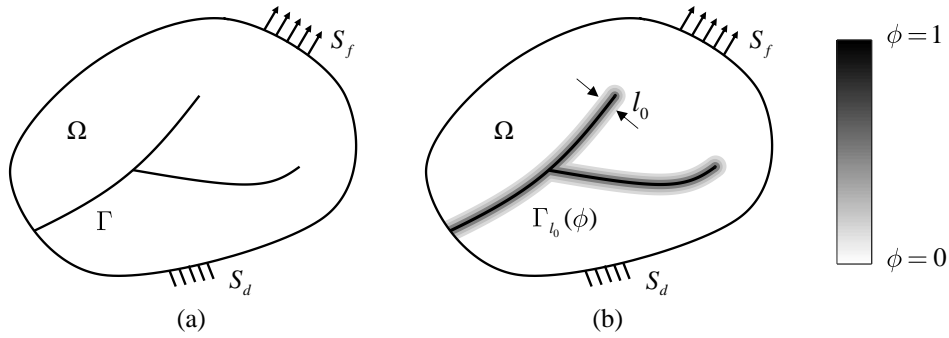


Fig. 2.1. Schematics of a linear elastic body Ω including (a) a sharp crack surface Γ , and (b) a diffusive crack surface $\Gamma_0(\phi)$.

The potential energy functional considering the fracture surface energy based on the Griffith's theory [1] is given as

$$\Pi(\mathbf{u}, \Gamma) = \int_V \psi_e(\boldsymbol{\varepsilon}) dV + G_c \int_{\Gamma} d\Gamma - \int_V \mathbf{f}_b \cdot \mathbf{u} dV - \int_{S_f} \mathbf{f}_s \cdot \mathbf{u} dS, \quad (2.1)$$

where \mathbf{u} is the displacement vector, ψ_e denotes the elastic strain energy density, $\boldsymbol{\varepsilon} = \boldsymbol{\varepsilon}(\mathbf{u})$ is the small strain tensor and G_c denotes the critical energy release rate, \mathbf{f}_b and \mathbf{f}_s denote the externally applied body and surface force vectors, respectively.

In Eq. (2.1), the elastic strain energy density function is expressed as

$$\psi_e(\boldsymbol{\varepsilon}) = \frac{1}{2} \lambda \text{tr}(\boldsymbol{\varepsilon})^2 + \mu \text{tr}(\boldsymbol{\varepsilon}^2), \quad (2.2)$$

in which λ and μ are Lamé constants.

From the idea presented by Ambrosio and Tortorelli [57-58], the fracture surface energy term on the right-hand side in Eq. (2.1) is approximated by

$$G_c \int_{\Gamma} d\Gamma \approx G_c \int_V \gamma(\phi, \nabla \phi) dV. \quad (2.3)$$

In Eq. (2.3), γ denotes the crack surface density function per unit volume

$$\gamma(\phi, \nabla \phi) = \frac{1}{2} l_0 \nabla \phi \cdot \nabla \phi + \frac{\phi^2}{2l_0}, \quad (2.4)$$

with

$$\nabla \phi = \frac{\partial \phi}{\partial x} \mathbf{e}_x + \frac{\partial \phi}{\partial y} \mathbf{e}_y + \frac{\partial \phi}{\partial z} \mathbf{e}_z,$$

where l_0 denotes the regularization parameter to control the width of crack diffusion with a diffusive crack surface $\Gamma_{l_0}(\phi)$ and ϕ is a damage parameter or phase field variable: a normalized value ranging from 0 (undamaged) to 1 (fully cracked), see Fig. 2.1(b). $\nabla \phi$ denotes the gradient of ϕ , and \mathbf{e}_x , \mathbf{e}_y and \mathbf{e}_z are the basis vectors of the Cartesian coordinate system. Fig. 2.2 shows the crack topologies with the distance from a crack surface (x_{Γ}) in the sharp crack model and the diffusive crack model.

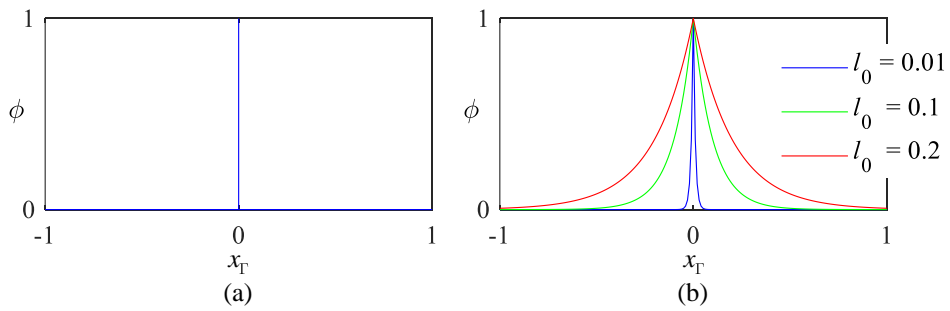


Fig. 2.2. Crack topologies in (a) the sharp crack model and (b) the diffusive crack model.

The spectral decomposition of the strain tensor is performed [27]

$$\boldsymbol{\varepsilon} = \boldsymbol{\varepsilon}_- + \boldsymbol{\varepsilon}_+, \quad (2.5)$$

with

$$\boldsymbol{\varepsilon}_{\pm} = \sum \langle \varepsilon_p \rangle_{\pm} \mathbf{n}_p \otimes \mathbf{n}_p \quad \text{and} \quad \langle x \rangle_{\pm} = \frac{1}{2} x \pm |x| ,$$

in which $\boldsymbol{\varepsilon}_{-}$ and $\boldsymbol{\varepsilon}_{+}$ denote the negative and positive components of the strain tensor, respectively, \mathbf{n}_p and ε_p denote the eigenvectors and eigenvalues of the strain tensor, respectively, and $\langle \cdot \rangle_{\pm}$ denotes the Macaulay bracket operator.

In addition to the decomposition of the strain tensor, the strain energy density function is also separated as

$$\psi_e(\boldsymbol{\varepsilon}) = \psi_e^{-}(\boldsymbol{\varepsilon}) + \psi_e^{+}(\boldsymbol{\varepsilon}) , \quad (2.6)$$

with

$$\psi_e^{\pm}(\boldsymbol{\varepsilon}) = \frac{1}{2} \lambda \langle \text{tr}(\boldsymbol{\varepsilon}) \rangle_{\pm}^2 + \mu \text{tr}(\boldsymbol{\varepsilon}_{\pm}^2) ,$$

where ψ_e^{-} and ψ_e^{+} are the negative and positive parts of the strain energy density function, respectively.

Using Eqs. (2.3) and (2.4) in Eq. (2.1), the following equation is obtained

$$\begin{aligned} \Pi(\mathbf{u}, \phi) = & \int_V [(1-\phi)^2 + k] \psi_e(\boldsymbol{\varepsilon}) dV + \int_V G_c \left[\frac{1}{2} l_0 \nabla \phi \cdot \nabla \phi + \frac{\phi^2}{2l_0} \right] dV \\ & - \int_V \mathbf{f}_b \cdot \mathbf{u} dV - \int_{S_f} \mathbf{f}_s \cdot \mathbf{u} dS , \end{aligned} \quad (2.7)$$

in which $(1-\phi)^2 + k$ denotes the quadratic function to control the strain energy degradation and k is a very small parameter to prevent numerical singularities ($k = 10^{-7}$ is used in this study).

Strong form governing equations are given by

$$\nabla \cdot \boldsymbol{\sigma} + \mathbf{f}_b = 0 , \quad (2.8)$$

$$\boldsymbol{\sigma} = [(1-\phi)^2 + k] \frac{\partial \psi_e(\boldsymbol{\varepsilon})}{\partial \boldsymbol{\varepsilon}} , \quad (2.9)$$

$$\left[\frac{G_c}{l_0} + 2\psi_e^{+} \right] \phi - G_c l_0 \nabla \phi \cdot \nabla \phi = 2\psi_e^{+} , \quad (2.10)$$

$$\mathbf{u} = \mathbf{u}_d \quad \text{on} \quad S_d , \quad (2.11)$$

$$\boldsymbol{\sigma} \cdot \mathbf{n} = \mathbf{f}_s \quad \text{on} \quad S_f , \quad (2.12)$$

$$\nabla \phi \cdot \mathbf{n} = 0 \quad \text{on} \quad S , \quad (2.13)$$

in which $\boldsymbol{\sigma}$ is the stress tensor, \mathbf{n} is the unit normal vector outward from the body, \mathbf{u}_d is the prescribed displacement, and $S = S_d \cup S_f$.

To consider the irreversibility of crack growth [59], the positive part of the strain energy density function ψ_e^+ in Eq. (2.10) is replaced as

$$H(\mathbf{x}, t) = \max_{s \in [0, t]} \psi_e^+(\boldsymbol{\varepsilon}(\mathbf{x}, s)), \quad (2.14)$$

in which t denotes time, s is time ranging from 0 to t , and $H(\mathbf{x}, t)$ denotes the local history field.

In Eqs. (2.9), (2.10) and (2.14), the hybrid formulation proposed by Ambati et al. [60] is adopted in this study (see Appendix A). Various formulations exist [27, 28, 61], and more advanced formulations have been recently proposed [62-69]. Note that the numerical schemes presented in the following sections can be used for other phase field formulations.

2.2. Finite element discretization

The first variation of Eq. (2.5) with Eqs. (2.8), (2.10) and (2.14) results in the following weak form governing equations

$$\int_V \boldsymbol{\sigma} : \delta \boldsymbol{\varepsilon} \, dV - \int_V \mathbf{f}_b \cdot \delta \mathbf{u} \, dV - \int_{S_f} \mathbf{f}_s \cdot \delta \mathbf{u} \, dS = 0, \quad (2.15)$$

$$\int_V -2(1-\phi)H\delta\phi \, dV + \int_V \left(G_c l_0 \nabla \phi \cdot \nabla \delta \phi + \frac{G_c}{l_0} \phi \delta \phi \right) dV = 0. \quad (2.16)$$

The displacement field of a 2D q -node finite element m is interpolated by

$$\mathbf{u}^{(m)} = \mathbf{H}_u^{(m)} \hat{\mathbf{u}}, \quad (2.17)$$

with

$$\mathbf{H}_u^{(m)} = \begin{bmatrix} h_1 & \cdots & h_q & \mathbf{0} \\ \mathbf{0} & & h_1 & \cdots & h_q \end{bmatrix} \text{ and } \hat{\mathbf{u}} = [u_1 \quad \cdots \quad u_q \quad v_1 \quad \cdots \quad v_q]^T,$$

where h_i is the shape function at node i , $\hat{\mathbf{u}}$ denotes the element nodal displacement vector, and u_i and v_i denote displacements in the x - and y -directions at node i , respectively.

The damage field of the finite element m is also interpolated by

$$\phi^{(m)} = \mathbf{H}_\phi^{(m)} \hat{\Phi}, \quad (2.18)$$

with

$$\mathbf{H}_\phi^{(m)} = [h_1 \quad \dots \quad h_q] \quad \text{and} \quad \hat{\Phi} = [\phi_1 \quad \dots \quad \phi_q]^T,$$

in which $\hat{\Phi}$ is the nodal damage parameter vector and ϕ_i is the nodal damage parameter at node i .

The interpolation of the local history field is given by

$$H^{(m)} = \mathbf{H}_h^{(m)} \hat{\mathbf{H}}, \quad (2.19)$$

with

$$\mathbf{H}_h^{(m)} = [h_1 \quad \dots \quad h_q] \quad \text{and} \quad \hat{\mathbf{H}} = [H_1 \quad \dots \quad H_q]^T,$$

where $\hat{\mathbf{H}}$ is the nodal local history vector and H_i denotes the local history at node i .

Applying the strain-displacement relation to Eq. (2.17), the strain vector for the element m is written as

$$\boldsymbol{\varepsilon}^{(m)} = \mathbf{B}_u^{(m)} \hat{\mathbf{u}}, \quad (2.20)$$

with

$$\boldsymbol{\varepsilon}^{(m)} = \begin{bmatrix} \varepsilon_{xx}^{(m)} \\ \varepsilon_{yy}^{(m)} \\ 2\varepsilon_{xy}^{(m)} \end{bmatrix}, \quad \mathbf{B}_u^{(m)} = \begin{bmatrix} \frac{\partial h_1}{\partial x} & \dots & \frac{\partial h_q}{\partial x} & & \mathbf{0} \\ & \mathbf{0} & & \frac{\partial h_1}{\partial y} & \dots & \frac{\partial h_q}{\partial y} \\ \frac{\partial h_1}{\partial y} & \dots & \frac{\partial h_q}{\partial y} & \frac{\partial h_1}{\partial x} & \dots & \frac{\partial h_q}{\partial x} \end{bmatrix}. \quad (2.21)$$

Note that $\boldsymbol{\varepsilon}^{(m)}$ is small deformation strain tensor and linear elastic material is considered in this study.

The damage gradient field of the element m is obtained as

$$\nabla \phi^{(m)} = \mathbf{B}_\phi^{(m)} \hat{\Phi}, \quad (2.22)$$

with

$$\mathbf{B}_\phi^{(m)} = \begin{bmatrix} \frac{\partial h_1}{\partial x} & \dots & \frac{\partial h_q}{\partial x} \\ \frac{\partial h_1}{\partial y} & \dots & \frac{\partial h_q}{\partial y} \end{bmatrix}. \quad (2.23)$$

The damage gradient field of the element m ($\nabla \phi^{(m)}$) denotes the gradient of the damage field of the element m ($\phi^{(m)}$) in x -, and y -directions.

Substituting Eqs. (2.17), (2.18) and (2.20) into Eq. (2.15), the following incremental equilibrium equation is obtained for the displacement field at time t

$${}^t \mathbf{K}_u^{(n)} \Delta \mathbf{U}^{(n)} = {}^t \mathbf{R} - {}^t \mathbf{F}_u^{(n)}, \quad (2.24)$$

with

$${}^t \mathbf{K}_u^{(n)} = \mathbf{A}_{m=1}^e {}^t \mathbf{K}_u^{(m)(n)}, \quad {}^t \mathbf{R} = \mathbf{A}_{m=1}^e {}^t \mathbf{R}^{(m)} \quad \text{and} \quad {}^t \mathbf{F}_u^{(n)} = \mathbf{A}_{m=1}^e {}^t \mathbf{F}_u^{(m)(n)},$$

$${}^t \mathbf{K}_u^{(m)(n)} = \int_{V^{(m)}} [(1 - {}^t \phi^{(m)})^2 + k] (\mathbf{B}_u^{(m)})^T \mathbf{C}^{(m)} \mathbf{B}_u^{(m)} dV^{(m)},$$

$${}^t \mathbf{R}^{(m)} = \int_{V^{(m)}} (\mathbf{H}_u^{(m)})^T {}^t \mathbf{f}_b^{(m)} dV^{(m)} + \int_{S_f^{(m)}} (\mathbf{H}_u^{(m)})^T {}^t \mathbf{f}_s^{(m)} dS^{(m)},$$

$${}^t \mathbf{F}_u^{(m)(n)} = \int_{V^{(m)}} [(1 - {}^t \phi^{(m)})^2 + k] (\mathbf{B}_u^{(m)})^T {}^t \boldsymbol{\sigma}^{(m)(n)} dV^{(m)},$$

$${}^t \boldsymbol{\sigma}^{(m)(n)} = \begin{bmatrix} {}^t \sigma_{xx}^{(m)(n)} & {}^t \sigma_{yy}^{(m)(n)} & {}^t \sigma_{xy}^{(m)(n)} \end{bmatrix}^T,$$

in which $\mathbf{A}_{m=1}^e \cdot$ is the FE assembly operator, e denotes the number of finite elements, n denotes the iteration number, $\Delta \mathbf{U}^{(n)}$ is the incremental displacement vector, ${}^t \mathbf{K}_u^{(n)}$ denotes the tangential stiffness matrix, ${}^t \mathbf{R}$ is the external force vector, ${}^t \mathbf{F}_u^{(n)}$ denotes the internal force vector, ${}^t \mathbf{K}_u^{(m)(n)}$ is the tangential stiffness matrix of the element m , $\mathbf{C}^{(m)}$ is the material law matrix for the element m , ${}^t \mathbf{R}^{(m)}$ is the external force vector for the element m , ${}^t \mathbf{f}_b^{(m)}$ and ${}^t \mathbf{f}_s^{(m)}$ are the externally applied body and surface force vectors for the element m , respectively, ${}^t \mathbf{F}_u^{(m)(n)}$ is the internal force vector for the element m , and ${}^t \boldsymbol{\sigma}^{(m)(n)}$ denotes the stress vector for the element m .

Using Eqs. (2.18), (2.19) and (2.22) in Eq. (2.16), the incremental equilibrium equation for the phase field at time t is obtained as

$${}^t \mathbf{K}_\phi^{(n)} \Delta \Phi^{(n)} = -{}^t \mathbf{F}_\phi^{(n)}, \quad (2.25)$$

with

$${}^t \mathbf{K}_\phi^{(n)} = \mathbf{A}_{m=1}^e {}^t \mathbf{K}_\phi^{(m)(n)} \quad \text{and} \quad {}^t \mathbf{F}_\phi^{(n)} = \mathbf{A}_{m=1}^e {}^t \mathbf{F}_\phi^{(m)(n)},$$

$${}^t \mathbf{K}_\phi^{(m)(n)} = \int_{V^{(m)}} \left(G_c l_0 (\mathbf{B}_\phi^{(m)})^T \mathbf{B}_\phi^{(m)} + \left[\frac{G_c}{l_0} + 2 {}^t H^{(m)} \right] (\mathbf{H}_\phi^{(m)})^T \mathbf{H}_\phi^{(m)} \right) dV^{(m)},$$

$$\begin{aligned} {}^t \mathbf{F}_\phi^{(m)(n)} = & - \int_{V^{(m)}} 2 {}^t H^{(m)} (\mathbf{H}_\phi^{(m)})^T dV^{(m)} \\ & + \int_{V^{(m)}} \left(G_c l_0 (\mathbf{B}_\phi^{(m)})^T \nabla {}^t \phi^{(m)(n)} + \left[\frac{G_c}{l_0} + 2 {}^t H^{(m)} \right] (\mathbf{H}_\phi^{(m)})^T {}^t \phi^{(m)(n)} \right) dV^{(m)}, \end{aligned}$$

where $\Delta \Phi^{(n)}$ is the incremental damage vector, ${}^t \mathbf{K}_\phi^{(n)}$ denotes the tangential stiffness matrix for the phase field,

${}^t \mathbf{F}_\phi^{(n)}$ denotes the internal force vector for the phase field, ${}^t \mathbf{K}_\phi^{(m)(n)}$ denotes the tangential stiffness matrix of the element m for the phase field, ${}^t \mathbf{F}_\phi^{(m)(n)}$ denotes the internal force vector for the element m for the phase field, ${}^t H^{(m)}$ is the local history field of the element m , and ${}^t \phi^{(m)(n)}$ is the damage field of the element m .

To solve the incremental equilibrium equations in Eqs. (2.24) and (2.25), the standard full Newton-Raphson method is employed. The iteration continues until the following convergence criteria are satisfied

$$\frac{\|\Delta \mathbf{U}^{(n)}\|_2}{\left\| \sum_{k=1}^n \Delta \mathbf{U}^{(k)} \right\|_2} \leq \varepsilon_u \quad \text{and} \quad \frac{\|\Delta \Phi^{(n)}\|_2}{\left\| \sum_{k=1}^n \Delta \Phi^{(k)} \right\|_2} \leq \varepsilon_\phi, \quad (2.26)$$

in which ε_u and ε_ϕ are the error tolerances for the displacement and phase fields, respectively.

The whole numerical procedure employed in this study for the phase field model is presented in Fig. 2.3. The incremental load step t is $t=0, 1, 2, \dots$ with $\Delta t=1$ in the load incremental loop. Force control is applied by

$${}^t \mathbf{R} = \alpha(t) {}^0 \mathbf{R}, \quad (2.27)$$

in which $\alpha(t)$ denotes the load parameter function for force control, and ${}^0 \mathbf{R}$ is the external force vector at the final load step.

Imposing the prescribed displacement at each load step, displacement control is applied by

$${}^t \mathbf{U} = \beta(t) {}^0 \mathbf{U}, \quad (2.28)$$

where ${}^t \mathbf{U}$ is the prescribed displacement vector at load step t , $\beta(t)$ is the load parameter function for displacement control and ${}^0 \mathbf{U}$ is the prescribed displacement vector at the final load step. Note that only displacement control is considered in this study.

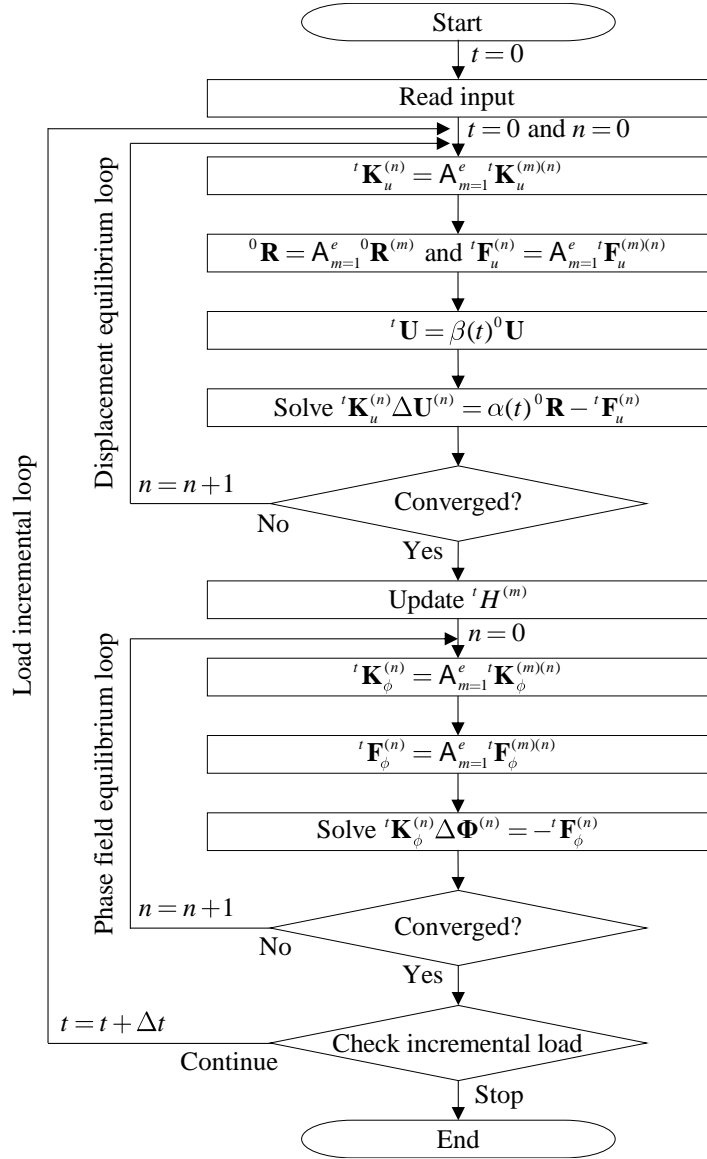


Fig. 2.3. Numerical procedure for the phase field model.

Chapter 3. Domain decomposition

To apply the adaptive update and adaptive mesh refinement schemes, the entire domain should be decomposed into several domains. The domain decomposition method is presented in this section.

Let us consider the domain of the crack propagation path (Ω_{cpp}^t) at time t , the crack tip domain (Ω_{ct}^t) at time t , and the near-tip domain (Ω_{nt}^t) at time t as shown in Fig. 3.1(a). When the three domains at time t are given, we search the three domains at time $t + \Delta t$. The searching procedure is presented in this section.

3.1. Crack tip domain

The crack tip domain $\Omega_{ct}^{t+\Delta t}$ is defined as a region belonging to Ω_{nt}^t and consisting of elements whose one or more nodal damage parameters are less than ϕ_c at time t and greater than ϕ_c at time $t + \Delta t$, see Figs. 3.1(a) and (b). The condition to define $\Omega_{ct}^{t+\Delta t}$ is expressed as

$$\Omega_{ct}^{t+\Delta t} = \{\mathbf{x}_i \mid \mathbf{x}_i \in \Omega_{nt}^t, \phi_i^t < \phi_c, \phi_i^{t+\Delta t} \geq \phi_c\}, \quad (3.1)$$

in which \mathbf{x}_i denotes the position vector of node i , ϕ_i^t and $\phi_i^{t+\Delta t}$ are the damage parameters of node i at time t and $t + \Delta t$, respectively, and ϕ_c denotes the critical value of the damage parameter.

3.2. Domain of crack propagation path

The domain of crack propagation path $\Omega_{cpp}^{t+\Delta t}$ is a region where the crack tip has already passed. This domain is defined as a region not belonging to $\Omega_{ct}^{t+\Delta t}$ and consisting of elements whose one or more nodal damage parameters are greater than ϕ_c at time $t + \Delta t$, see Fig. 3.1(b). The condition to define $\Omega_{cpp}^{t+\Delta t}$ is expressed as

$$\Omega_{cpp}^{t+\Delta t} = \{\mathbf{x}_i \mid \mathbf{x}_i \notin \Omega_{ct}^{t+\Delta t}, \phi_i^{t+\Delta t} \geq \phi_c\}. \quad (3.2)$$

3.3. Near-tip domain

The near-tip domain $\Omega_{nt}^{t+\Delta t}$ is defined as a region consisting of elements within a shorter distance than R_c from all the nodal positions belonging to $\Omega_{ct}^{t+\Delta t}$, see Fig. 3.1(b). The condition to define $\Omega_{nt}^{t+\Delta t}$ is expressed as

$$\Omega_{nt}^{t+\Delta t} = \{\mathbf{x}_i \mid \|\mathbf{x}_i - \mathbf{x}_c\| \leq R_c, \mathbf{x}_c \in \Omega_{ct}^{t+\Delta t}\}, \quad (3.3)$$

where \mathbf{x}_c is the position vector of a node belonging to $\Omega_{ct}^{t+\Delta t}$.

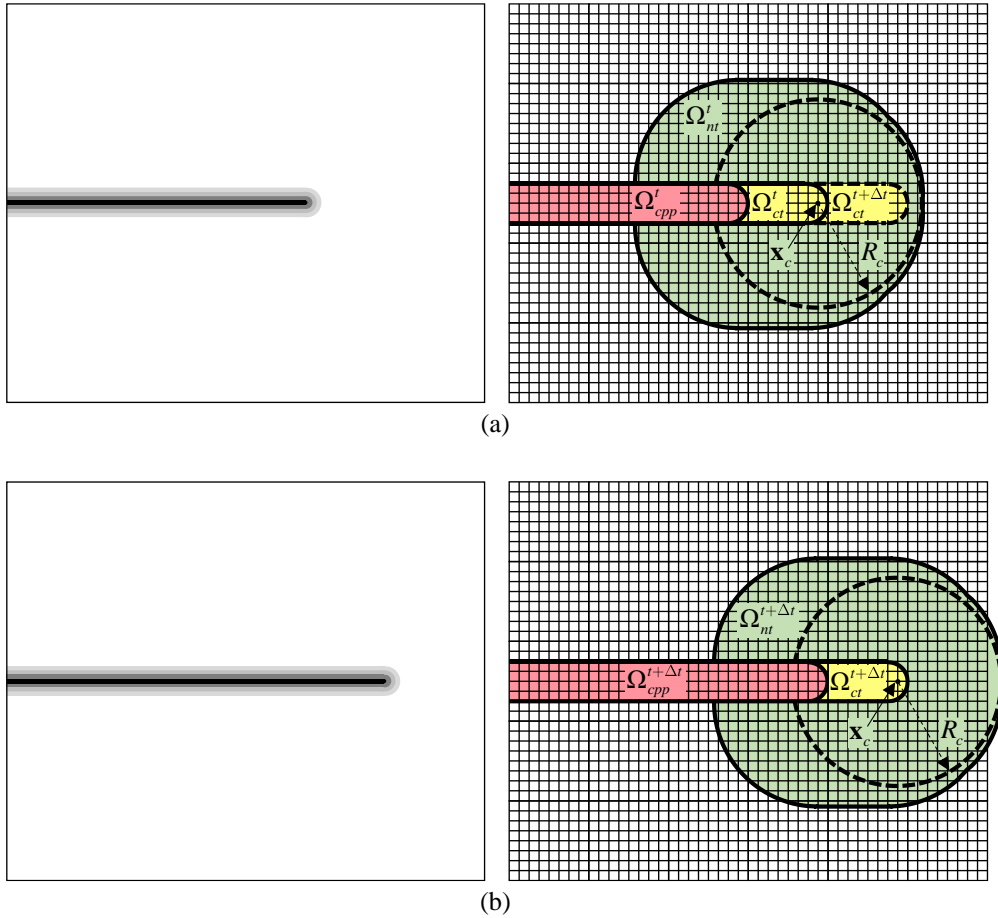


Fig. 3.1. Identification of the mesh refinement domains (a) at time t and (b) at time $t + \Delta t$. The crack tip domain is colored yellow, the domain of the crack propagation path is colored red, and the near-tip domain is colored green.

When the crack does not propagate, we use $\Omega_{ct}^{t+\Delta t} = \Omega_{ct}^t$. The identification of the mesh refinement domains is performed at each load step. The coarse meshes in $\Omega_{ct}^{t+\Delta t}$, $\Omega_{cpp}^{t+\Delta t}$ and $\Omega_{nt}^{t+\Delta t}$ are adaptively converted into fine meshes.

Chapter 4. Adaptive mesh refinement

Recently, several adaptive mesh refinement schemes were proposed to improve the computational efficiency of the phase field model [33-47]. We also employ an adaptive mesh refinement scheme using variable-node elements, which is different from the schemes previously proposed. In this section, we explain the adaptive mesh refinement scheme utilized in this study.

4.1. Variable-node elements

In order to implement the adaptive mesh refinement scheme, variable-node elements are employed in transient regions where mesh density varies. Their shape functions are obtained using the moving least square (MLS) (see Refs. [51-56] for detailed derivations). To examine the performance of variable-node elements, the patch test is performed (see Appendix B). It is shown that variable-node elements passes the patch test. A 4-node element in a coarse mesh can be connected to eight 4-node elements in a fine mesh through element edges. For this connection, three variable-node elements are employed in this study: 11-node elements with 8 sub-domains, 18-node elements with 64 sub-domains, and 25-node elements with 64 sub-domains as described in Fig. 4.1. To perform numerical integration, the 2×2 Gauss quadrature is adopted in each sub-domain. The mesh connection between the coarse and fine meshes is illustrated in Fig. 4.2.

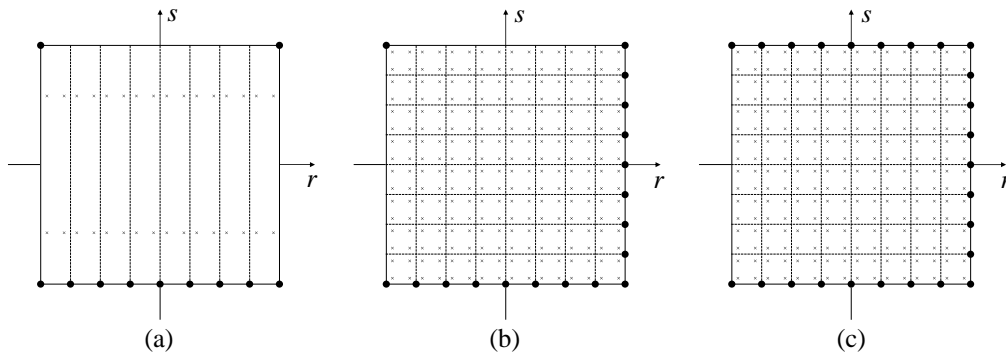


Fig. 4.1. Examples of variable-node elements: (a) 11-node element, (b) 18-node element, and (c) 25-node element.

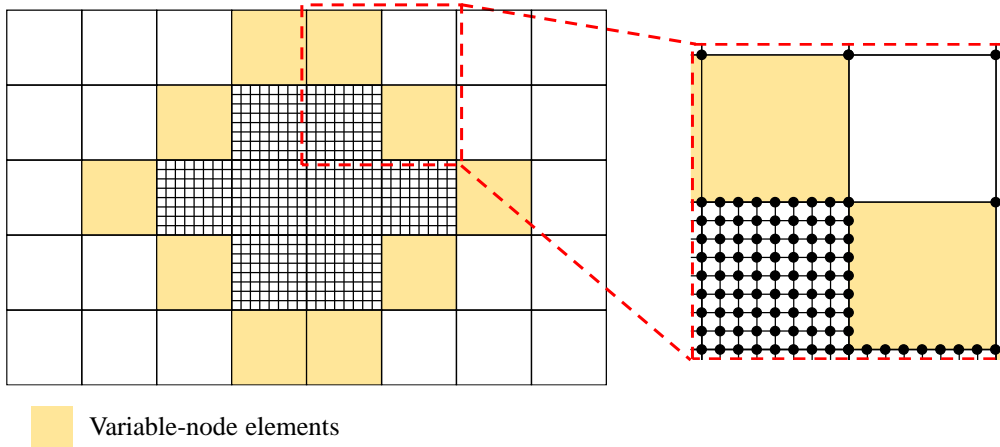
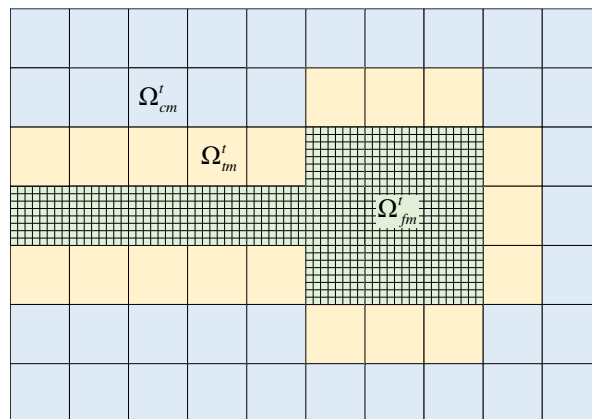


Fig. 4.2. Use of variable-node elements to connect the coarse and fine meshes.

4.2. Mesh connection

To apply the adaptive mesh refinement, it is necessary to identify the mesh refinement domains. The domain of the whole body Ω' at time t is divided into the coarse mesh domain (Ω'_{cm}), the fine mesh domain (Ω'_{fm}) and the transient mesh domain (Ω'_{tm}) between them as shown in Fig. 4.3.



Ω'_{cm} : Coarse mesh domain at time t
 Ω'_{fm} : Fine mesh domain at time t
 Ω'_{tm} : Transient mesh domain at time t

Fig. 4.3. Mesh geometry and domain Ω' divided into Ω'_{cm} , Ω'_{fm} and Ω'_{tm} .

4.3. Adaptive mesh refinement during crack propagation

The coarse meshes in $\Omega_{ct}^{t+\Delta t}$, $\Omega_{cpp}^{t+\Delta t}$ and $\Omega_{nt}^{t+\Delta t}$ are adaptively converted into fine meshes, as shown in Fig. 4.4. Note that the fine meshes away from $\Omega_{ct}^{t+\Delta t}$, $\Omega_{cpp}^{t+\Delta t}$ and $\Omega_{nt}^{t+\Delta t}$ are also adaptively recovered into coarse meshes. When the coarse mesh is converted into the transient or fine mesh, the displacement, damage parameter and local history fields of additional nodes are mapped utilizing nodal displacements, damage parameters and local history fields of the coarse mesh.

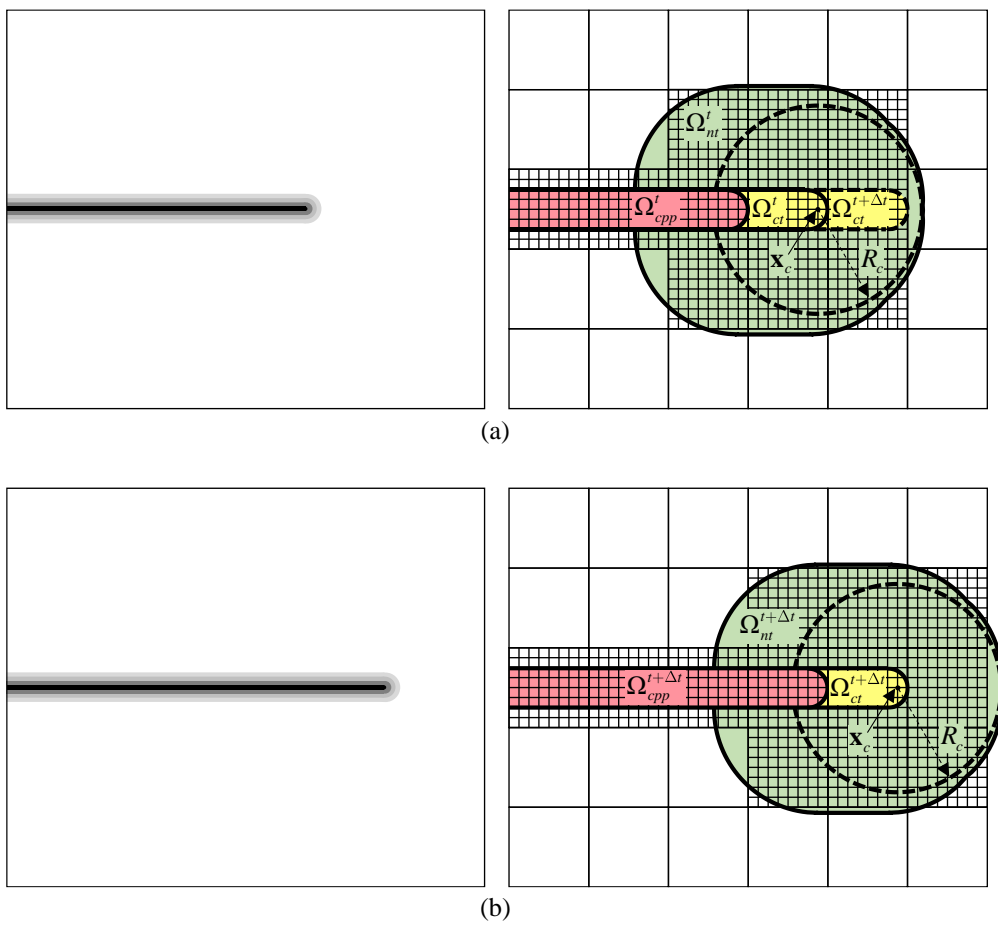


Fig. 4.4. Mesh geometry of adaptive mesh refinement (a) at time t and (b) at time $t + \Delta t$. The crack tip domain is colored yellow, the domain of the crack propagation path is colored red, and the near-tip domain is colored green.

4.4. Hole boundary handling procedure

When the crack tip encounters a hole or void during the simulation, it is not easy to predict crack propagation. Thus, we introduce a methodology for the adaptive mesh refinement in case that the crack tip encounters a hole. If there is a hole boundary Γ_h in the body as shown in Fig. 4.5(a), the domain of elements adjacent to Γ_h are defined as Ω_h described in Fig. 4.5(b). When the near-tip domain Ω_{nt}^t penetrates into the hole domain Ω_h as depicted in Fig. 4.5(b), Ω_h is added into Ω_{nt}^t to consider Ω_h as a region where the crack propagation is expected. The coarse meshes on Ω_h are converted into fine meshes, as shown in Fig. 4.5(c). When the near-tip domain $\Omega_{nt}^{t+\Delta t}$ leaves the domain Ω_h , the meshes on Ω_h are recovered into the coarse meshes for improving the computational efficiency, as illustrated in Fig. 4.5(d).

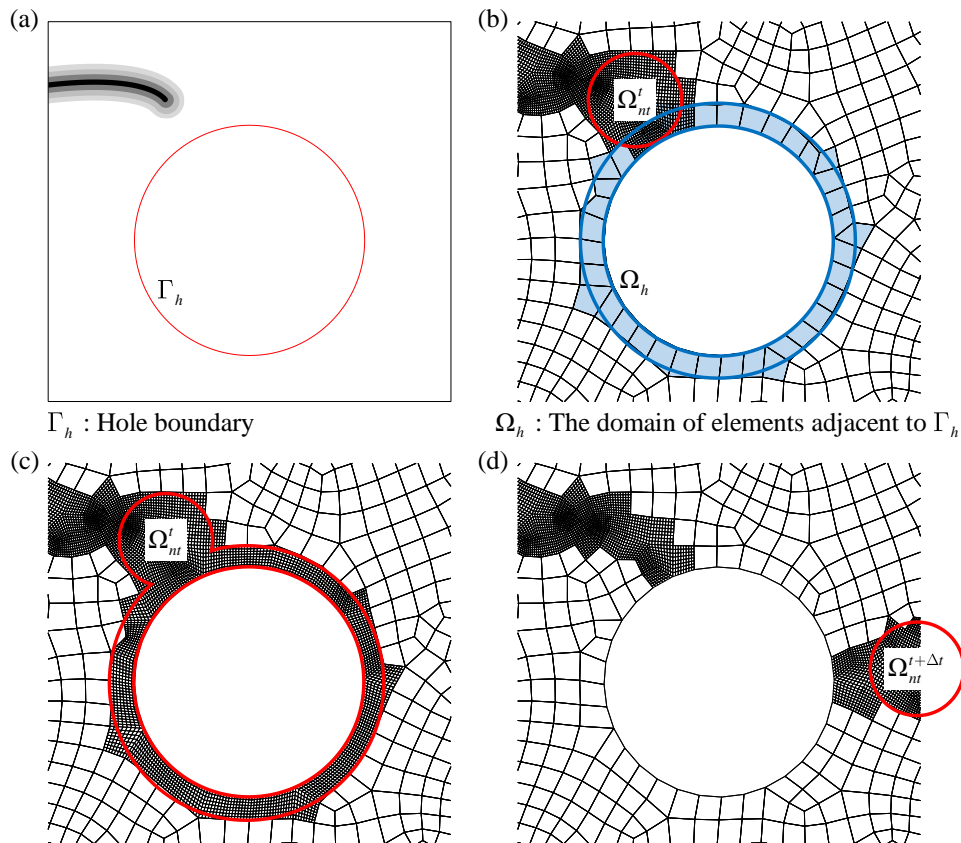


Fig. 4.5. Schematics of the hole boundary handling procedure: (a) a domain Ω with a hole boundary Γ_h , (b) mesh geometry when Ω_{nt}^t penetrates into Ω_h , (c) mesh geometry at time t , and (d) mesh geometry at time $t + \Delta t$.

Chapter 5. Adaptive update

5.1. Motivation

To obtain the solution of the phase field model, the incremental equilibrium equations for the displacement and phase fields in Eqs. (2.24) and (2.25) are iteratively solved, where the tangential stiffness matrices, displacement vector, phase field vector, internal force vectors, local history field and so on are updated.

During the simulation, the structural properties used in the computation such as stiffness, strain energy and damage change rapidly only in the near-tip domain Ω_{nt}^t , shown in Fig. 5.1. However, such properties rarely vary in the domain far from the crack tip (Ω_{ft}^t), as seen in Fig. 5.1. The key idea of this study is that the computational efficiency of the phase field model can be improved by avoiding computations related with the structural properties in Ω_{ft}^t . We call this the adaptive update scheme.

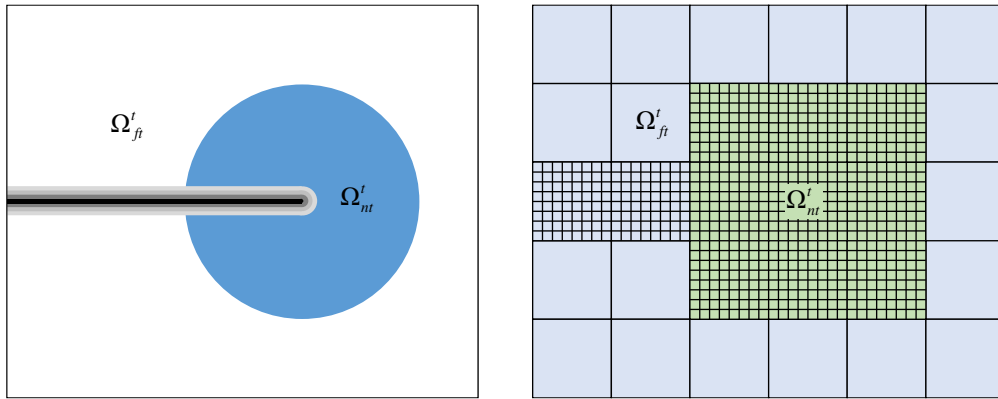


Fig. 5.1. Near-tip domain Ω_{nt}^t and domain far from the crack tip Ω_{ft}^t . While the structural properties in Ω_{nt}^t change rapidly during the simulation, those in Ω_{ft}^t rarely vary.

5.2. Key idea

To apply the adaptive update scheme in the displacement and phase fields equilibrium procedures, the global tangential stiffness matrices for the displacement and phase fields in Eqs. (2.24) and (2.25) are divided as

$${}^t \mathbf{K}_u^{(n)} = {}^t \mathbf{K}_u^{nt(n)} + {}^t \mathbf{K}_u^{ft(n)} \quad \text{and} \quad {}^t \mathbf{K}_\phi^{(n)} = {}^t \mathbf{K}_\phi^{nt(n)} + {}^t \mathbf{K}_\phi^{ft(n)}, \quad (5.1)$$

with

$${}^t \mathbf{K}_u^{nt(n)} = \mathbf{A}_{m=1}^{e^{nt}} {}^t \mathbf{K}_u^{(m)(n)}, \quad {}^t \mathbf{K}_u^{ft(n)} = \mathbf{A}_{m=1}^{e^{ft}} {}^t \mathbf{K}_u^{(m)(n)},$$

$${}^t \mathbf{K}_\phi^{nt(n)} = \mathbf{A}_{m=1}^{e^{nt}} {}^t \mathbf{K}_\phi^{(m)(n)}, \quad {}^t \mathbf{K}_\phi^{ft(n)} = \mathbf{A}_{m=1}^{e^{ft}} {}^t \mathbf{K}_\phi^{(m)(n)},$$

in which e^{nt} and e^{ft} are the number of elements within Ω_{nt} and Ω_{ft} , respectively, ${}^t \mathbf{K}_u^{nt(n)}$ and ${}^t \mathbf{K}_u^{ft(n)}$ denote the tangential stiffness matrices for the displacement field of elements in Ω_{nt} and Ω_{ft} , respectively, and ${}^t \mathbf{K}_\phi^{nt(n)}$ and ${}^t \mathbf{K}_\phi^{ft(n)}$ are the tangential stiffness matrices for the phase field of elements in Ω_{nt} and Ω_{ft} , respectively. Note that in actual computations all matrices in Eq. (5.1) are stored in sparse matrix form to save memory space.

In the standard numerical procedure for the phase field model as shown in Fig. 2.3, ${}^t \mathbf{K}_u^{(n)}$ and ${}^t \mathbf{K}_\phi^{(n)}$ are updated at every load step ($t=0, 1, 2, \dots$). However, in the adaptive update scheme, ${}^t \mathbf{K}_u^{ft(n)}$ and ${}^t \mathbf{K}_\phi^{ft(n)}$ are occasionally updated, while ${}^t \mathbf{K}_u^{nt(n)}$ and ${}^t \mathbf{K}_\phi^{nt(n)}$ are updated at every load step ($t=0, 1, 2, \dots$). ${}^t \mathbf{K}_u^{ft(n)}$ and ${}^t \mathbf{K}_\phi^{ft(n)}$ are adaptively updated at specific load steps satisfying the following criteria

$$\frac{\sum_{k=t_u}^t \max_{\phi_i^k \in \Omega_{ct}^k} (\phi_i^k)}{\max_{\phi_i^t \in \Omega_{ct}^t} (\phi_i^t)} \geq \eta, \quad (5.2)$$

in which t_u denotes the initial update load step and η is the update parameter. After the criteria in Eq. (5.2) is satisfied, t_u is set to the next load step. Note that $\eta = 10$ was used in this study (see Appendix C). The stiffness update is additionally performed when the crack propagates ($\Omega_{ct}^t \neq \Omega_{ct}^{t-\Delta t}$).

For the history update procedure in Eq. (2.14), the adaptive update scheme is also considered in the same manner. The local history ${}^t H^{(m)}$ of elements in Ω_{ft} is adaptively updated when the criteria in Eq. (5.2) is satisfied, and also when the crack propagates ($\Omega_{ct}^t \neq \Omega_{ct}^{t-\Delta t}$). However, ${}^t H^{(m)}$ of the elements in Ω_{nt} is updated at every load step ($t=0, 1, 2, \dots$).

5.3. Numerical examples

In this section, we investigate the performance of the adaptive update scheme through various numerical examples: the single-edge notched tension problem, the single-edge notched shear problem, the symmetric three-point bending problem, the notched plate with three holes, the single-edge notched shear plate with diamond-shaped holes, the L-shaped panel, and the single-edged notched branching problem.

In the local mesh refinement scheme, a fine mesh is employed in the domain where crack propagation is expected, and a coarse mesh is used in the remaining domain. Also, re-meshing is not performed during simulation. In the adaptive mesh refinement scheme, a coarse mesh is used in the entire domain at the beginning of the simulation. During the simulation, the coarse mesh in the domain where a crack propagates is adaptively converted into a fine mesh using variable-node elements.

To show the performance of the adaptive update scheme combined with the local and adaptive mesh refinement schemes, four cases are considered: the local mesh refinement scheme by itself and, with the adaptive update scheme, and the adaptive mesh refinement scheme by itself, and with the adaptive update scheme.

In all the numerical examples, the dimensions shown in the figures are in mm. We use 4-node quadrilateral element with unit thickness. The plane strain condition is considered. The convergence criterions ε_u and ε_ϕ are 10^{-5} .

The critical damage parameter is taken as $\phi_c = 0.5$.

The phase field model do not require additional criteria for when/where cracks initiate, grow, and how much and in what direction they propagate. Therefore, the phase field model is basically capable of analyzing even when pre-crack does not exist. In that case, in order to catch crack initiation early and define the domain of crack initiation as a refinement domain, the critical damage parameter is considered as $\phi_c = 0.1$ until the crack propagates (see Appendix D). After identifying the domain of crack initiation, the critical damage parameter is taken as $\phi_c = 0.5$.

To ensure the solution accuracy, it is necessary to satisfy the condition of the element characteristic length ($l_e = \sqrt{A_e}$ with an element area A_e) that is smaller than half of the regularization parameter in the crack propagation domain, which is, $l_e \leq 0.5l_0$ [28]. For the adaptive mesh refinement scheme, the element characteristic length of the initial mesh geometry is taken as $l_e = 4l_0$. The numerical procedure was implemented in MATLAB 2017a and the computation was performed on a PC with an Intel(R) Core(TM) i7-7700 CPU @ 3.60GHz and 64GB RAM.

5.3.1. Single-edge notched tension problem

Let us consider a square plate including a single-edge crack as described in Fig. 5.2(a) [27, 39, 43, 48]. The plate is subjected to a prescribed vertical displacement along the top edge, and the bottom edge of the plate is fixed. Young's modulus, Poisson's ratio, and the critical energy release rate are given by $E = 210$ GPa, $\nu = 0.3$, and $G_c = 2.7 \times 10^{-3}$ kN/mm, respectively. The regularization parameter is $l_0 = 0.0075$ mm. The radius R_c to determine the near-tip domain is 0.04 mm.

We use the mesh geometry (21791 elements) in Fig. 5.2(b) for the local mesh refinement scheme, and the regular mesh of 50×50 elements in Fig. 5.2(c) is used for the adaptive mesh refinement scheme. The prescribed displacement δ increases up to 0.0063 mm for displacement control. The number of the total incremental load step is 1800 and $\beta(t)$ is given in Fig. 5.2(d).

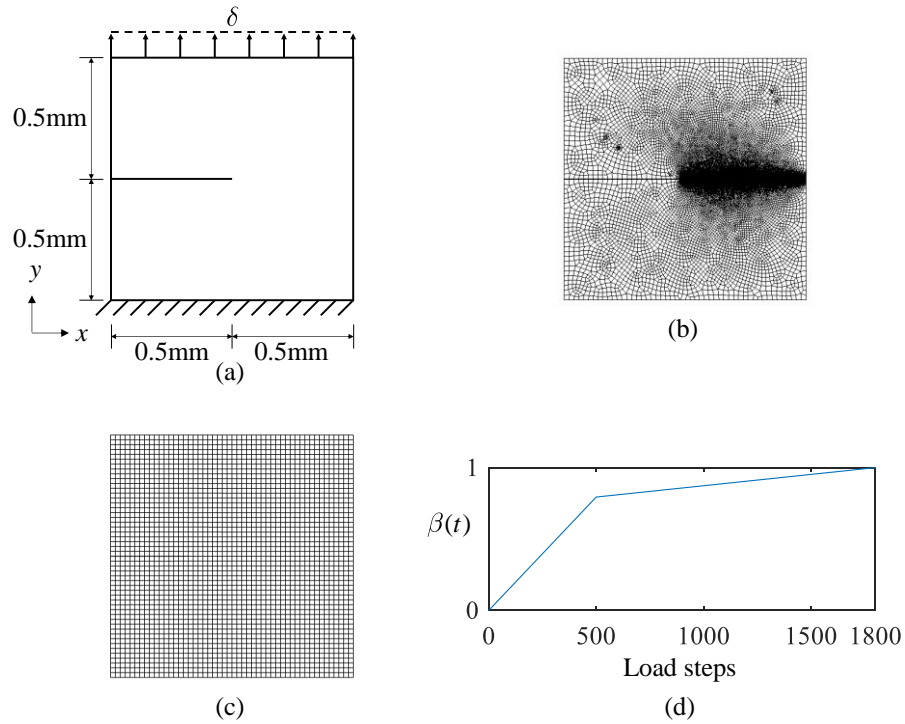


Fig. 5.2. Single-edge notched tension problem: (a) geometry and boundary conditions, (b) mesh used for the local mesh refinement scheme, (c) initial mesh used for the adaptive mesh refinement scheme, and (d) load history curve.

When the adaptive mesh refinement scheme is applied, the changes in mesh geometry and crack pattern during crack propagation are illustrated in Fig. 5.2. For the four analysis cases, the load-displacement curves are plotted in Fig 5.3(a). In the curves, the load is the total reaction force in the y -direction along the top edge. The curves are also compared with those of Miehe et al. [27], Patil et al. [39], and Tian et al. [43], see Fig. 5.4(b). Table 5.1 and Table 5.2 show the specific computation times corresponding to the four cases. It is observed that the adaptive update scheme significantly reduces the solution time with almost no change in solutions. As expected, the adaptive mesh refinement scheme is much more computationally effective than the local mesh refinement scheme.

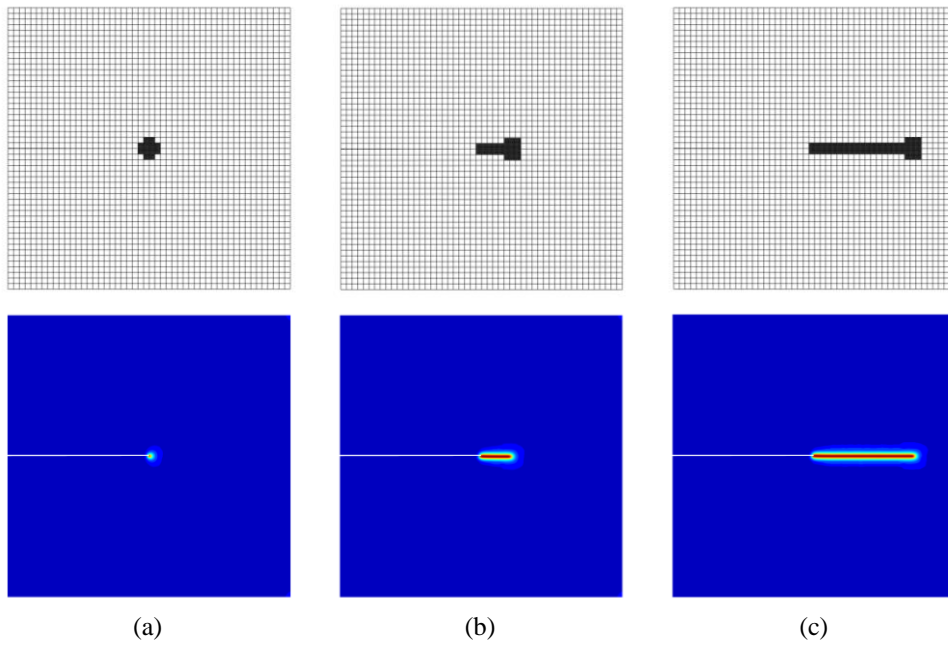


Fig. 5.3. Mesh geometries and crack patterns for the single-edge notched tension problem when (a) $\delta = 0.005399$ mm (3452 nodes and 3256 elements), (b) $\delta = 0.005549$ mm (4103 nodes and 3886 elements), and (c) $\delta = 0.005859$ mm (5699 nodes and 5398 elements).

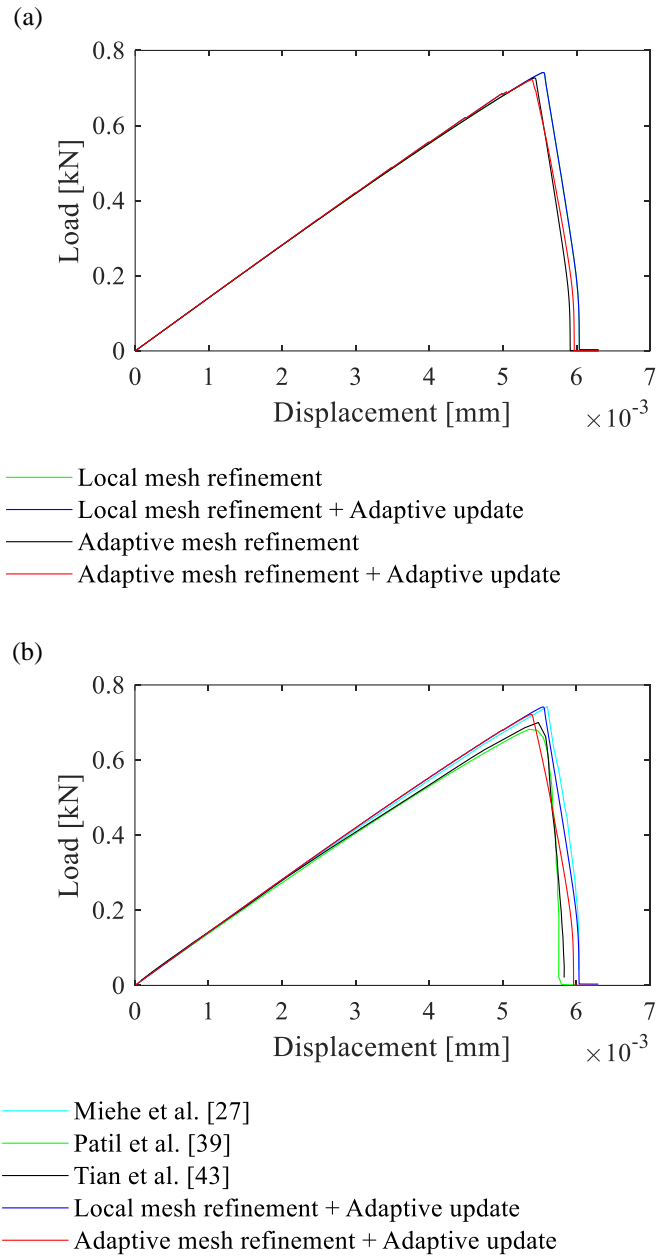


Fig. 5.4. Load-displacement curves on the single-edge notched tension problem: (a) when the adaptive update scheme is used and when it is not used, and (b) when compared with previous results.

Table 5.1. Specific computation times required for the single-edge notched tension problem in Fig. 5.2 for the local mesh refinement scheme.

Numerical schemes applied	Items	Computation time	
		[sec]	Ratio [%]
Local mesh refinement	History field update	6863.18	21.36
	Stiffness construction	22250.76	69.23
	Equation solving	2928.56	9.11
	Etc	97.00	0.30
	Total	32139.50	100.00
Local mesh refinement + Adaptive update	History field update	2132.38	6.01
	Stiffness construction	16034.04	45.12
	Equation solving	4535.24	12.76
	Etc	364.32	1.02
	Total	23065.98	64.91

Table 5.2. Specific computation times required for the single-edge notched tension problem in Fig. 5.2 for the adaptive mesh refinement scheme.

Numerical schemes applied	Items	Computation time	
		[sec]	Ratio [%]
Adaptive mesh refinement	Mesh refinement	25.99	0.54
	History field update	1025.52	21.24
	Stiffness construction	3504.25	72.59
	Equation solving	252.97	5.24
	Etc	18.68	0.39
	Total	4827.41	100.00
Adaptive mesh refinement + Adaptive update	Mesh refinement	19.68	0.41
	History field update	154.94	3.21
	Stiffness construction	1886.50	39.08
	Equation solving	343.08	7.11
	Etc	15.83	0.32
	Total	2420.03	50.13

5.3.2. Single-edge notched shear problem

Here, a square plate with a single-edge crack is considered as illustrated in Fig. 5.5(a) [27, 30, 39, 42, 43, 48]. A horizontal displacement is uniformly applied along the top edge of the plate, and the bottom edge of the plate is fixed. Young's modulus, Poisson's ratio, and the critical energy release rate are given by $E = 210$ GPa, $\nu = 0.3$, and $G_c = 2.7 \times 10^{-3}$ kN/mm, respectively. The regularization parameter is $l_0 = 0.0075$ mm. The radius to determine the near-tip domain (R_c) is 0.04 mm.

The mesh geometry (22413 elements) shown in Fig. 5.5(b) is used for the local mesh refinement scheme, and the regular mesh of 50×50 elements used for the adaptive mesh refinement scheme is shown in Fig. 5.5(c). The prescribed displacement δ is applied until 0.015 mm, the number of the total incremental load step is 1500, and $\beta(t)$ increases uniformly.

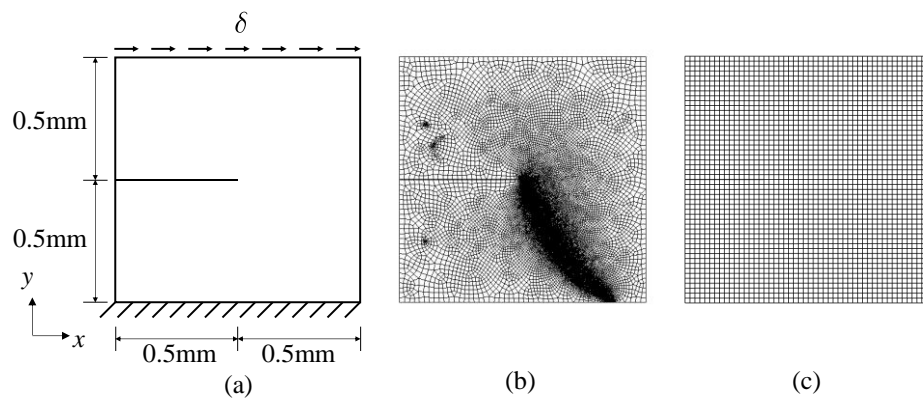


Fig. 5.5. Single-edge notched shear problem: (a) geometry and boundary conditions, (b) mesh used for the local mesh refinement scheme, and (c) initial mesh used for the adaptive mesh refinement scheme.

When the adaptive mesh refinement scheme is adopted, the mesh geometries and crack patterns formed during crack propagation are described in Fig. 5.6. Fig. 5.7(a) shows the load-displacement curves obtained for the four analysis cases, in which the load is the total reaction force in the x -direction along the top edge. Fig. 5.7(b) shows the curves by Miehe et al. [27], Patil et al. [39] and Borden et al. [30]. The computation times for the four analysis cases are listed in Table 5.3. When the adaptive update scheme is employed, the computation time is reduced by about 40% to 50% but there is almost no change in solutions.

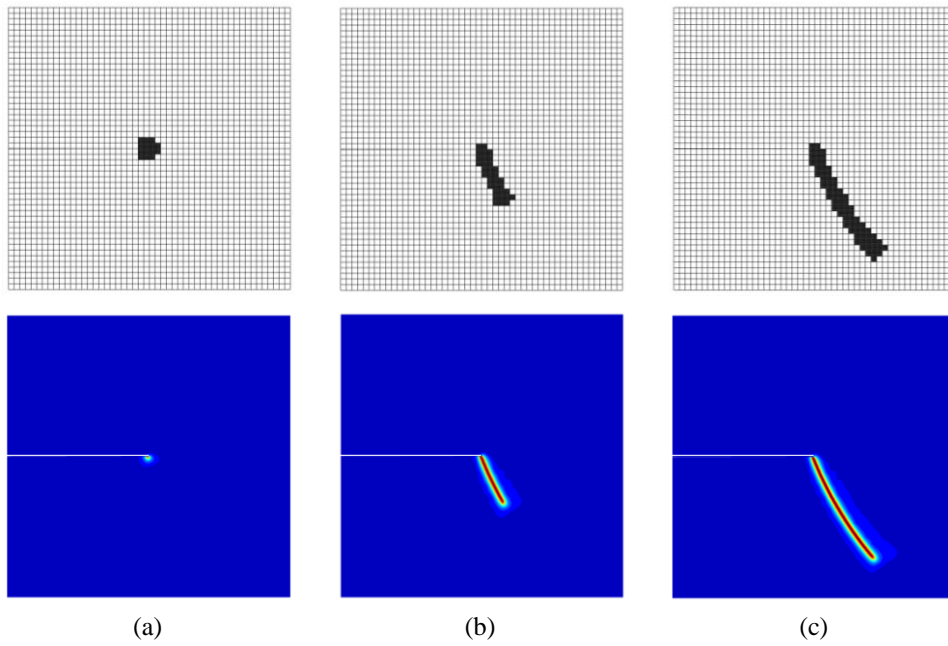


Fig. 5.6. Mesh geometries and crack patterns for the single-edge notched shear problem when (a) $\delta = 0.00869$ mm (3578 nodes and 3382 elements), (b) $\delta = 0.01129$ mm (4838 nodes and 4579 elements) and (c) $\delta = 0.01299$ mm (7225 nodes and 6847 elements).

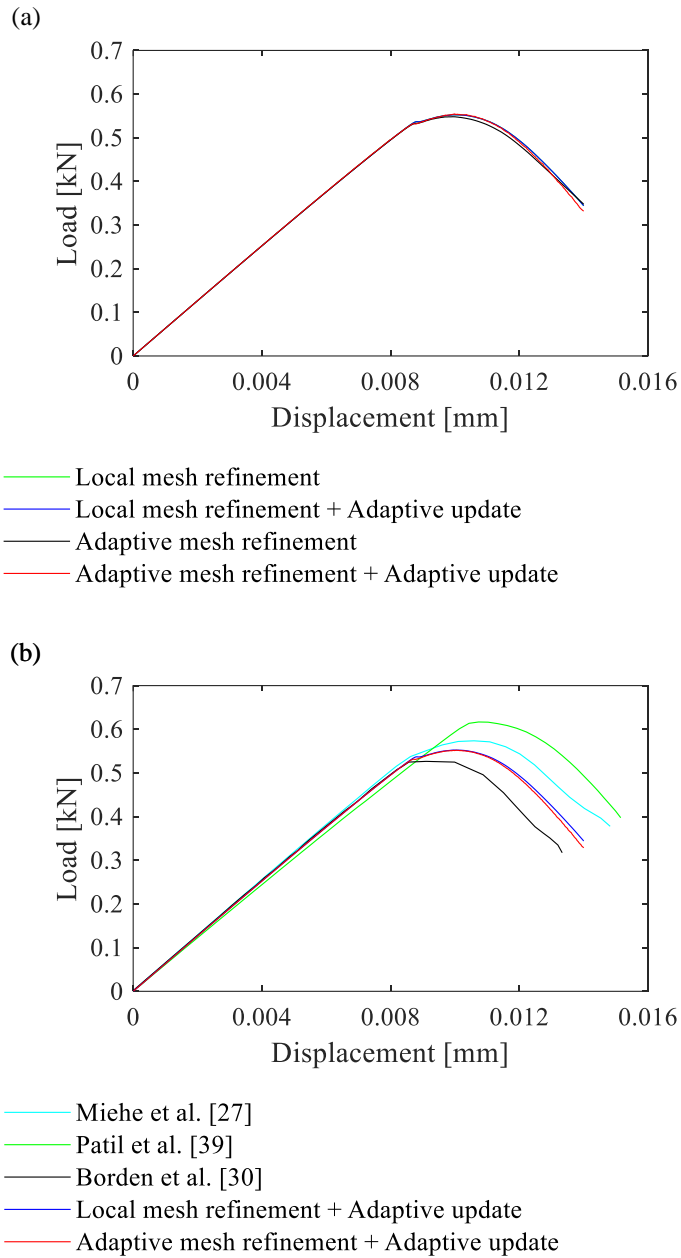


Fig. 5.7. Load-displacement curves on the single-edge notched shear problem: (a) when the adaptive update scheme is used and when it is not used, and (b) when compared with previous results.

Table 5.3. Computation times required for the single-edge notched shear problem in Fig. 5.5.

Numerical schemes applied	Computation time	
	[sec]	Ratio [%]
Local mesh refinement	25661.54	100.00
Local mesh refinement + Adaptive update	17699.75	68.97
Adaptive mesh refinement	3572.66	100.00
Adaptive mesh refinement + Adaptive update	2037.74	57.04

We additionally compare the computational efficiency of the proposed schemes with previous numerical results presented in Refs. [39, 42, 43]. Two analysis cases are considered using uniform $N \times N$ meshes: when no adaptive scheme is employed and when adaptive schemes are adopted. Computation time ratios between both cases are shown in Table 5.4 and Fig. 5.8. The computation times measured without adaptive scheme are considered 100%. Note that initial meshes are provided in the table when adaptive schemes are used.

Table 5.4. Computation time ratios for the single-edge notched shear problem in Fig. 5.5.

	No adaptive scheme used	Adaptive schemes used	Computation time ratio [%]
	Number of elements (N)	Number of elements	
Patil et al. [39]	62500 (250)	2450	73.38
Hirshikesh et al. [42]	20164 (142)	1060	35.83
Tian et al. [43]	78400 (280)	1225	6.02
Adaptive mesh refinement	10000 (100)	2500	31.28
	40000 (200)	2500	7.77
	90000 (300)	2500	3.37
Adaptive mesh refinement + Adaptive update	10000 (100)	2500	17.84
	40000 (200)	2500	4.43
	90000 (300)	2500	1.92

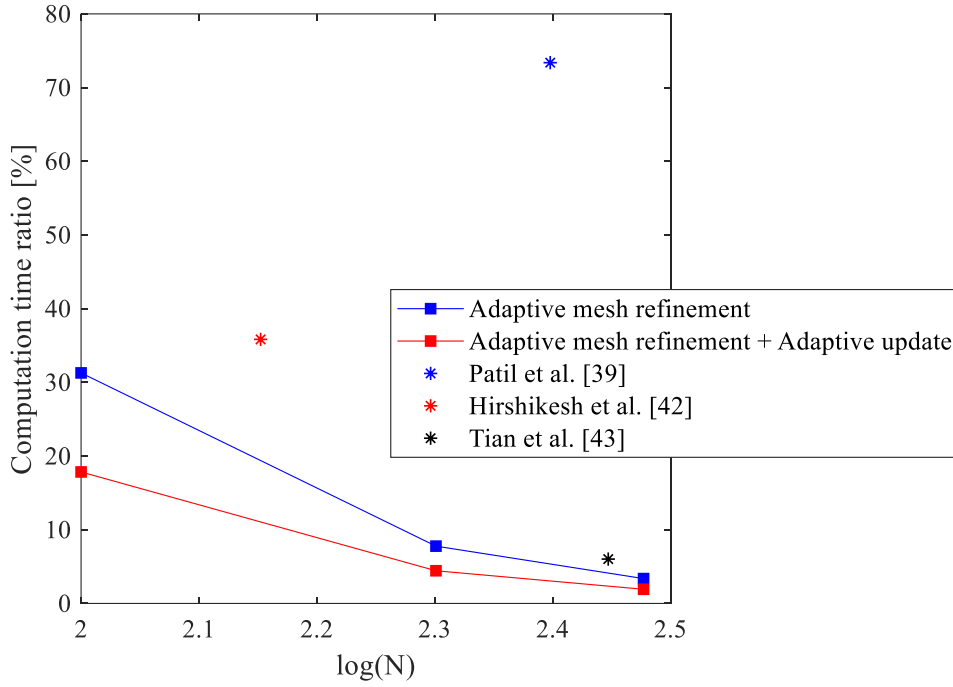


Fig. 5.8. Computational efficiency curves for the single-edge notched shear problem in Fig. 5.5.

5.3.3. Symmetric three-point bending problem

The third problem is a symmetric three-point bending test on a notched specimen [27, 41, 48, 60]. The geometry and boundary conditions are depicted in Fig. 5.9(a). The prescribed displacement δ is applied at point A. Lamé's constants are $\lambda = 12.0$ GPa and $\mu = 8.0$ GPa, and the critical energy release rate is $G_c = 0.5 \times 10^{-3}$ kN/mm. The regularization parameter is $l_0 = 0.03$ mm, and the radius of the near-tip domain R_c is 0.2 mm.

We consider a mesh of 9127 elements in Fig. 5.9(b) for the local mesh refinement scheme, and a mesh of 1560 elements in Fig. 5.9(c) for the adaptive mesh refinement scheme. For displacement control, δ increases up to 0.065 mm. We use 2900 incremental load steps with the load parameter function $\beta(t)$ shown in Fig. 5.9(d).

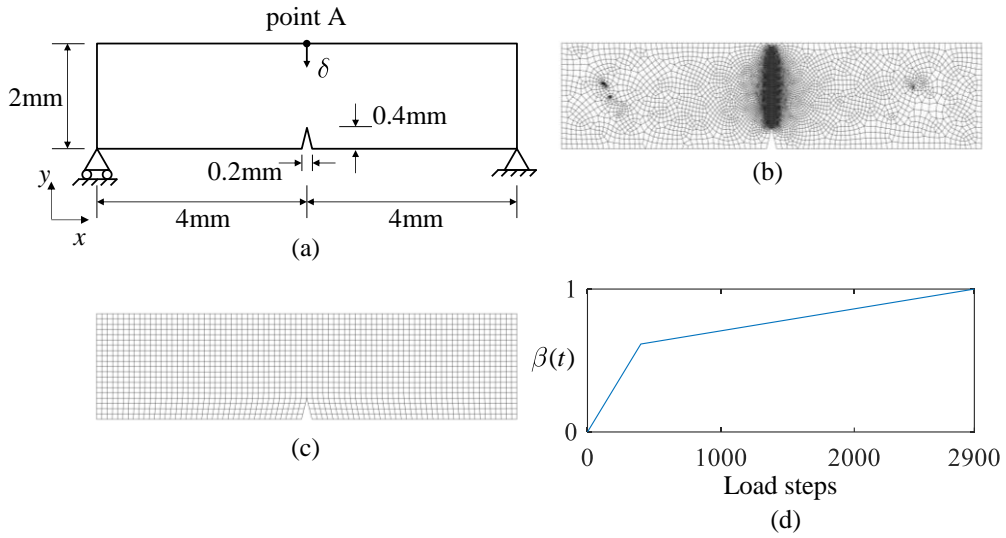


Fig. 5.9. Symmetric three-point bending problem: (a) geometry and boundary conditions, (b) mesh geometry for the local mesh refinement scheme, (c) initial geometry for the adaptive mesh refinement scheme, and (d) load history curve.

Fig. 5.10 illustrates the mesh geometries and crack patterns created by the adaptive mesh refinement scheme during crack propagation. Fig. 5.11(a) presents the load-displacement curves for the four analysis cases. In the curves, the load is the reaction force in the y -direction at point A. Fig. 5.11(b) displays the load-displacement curves calculated by Miehe et al. [27], Goswami et al. [41] and Ambati et al. [60]. Table 5.5 gives the computation times with and without the adaptive update scheme together with the local and adaptive mesh refinement schemes. The proposed adaptive update scheme provides improved computational efficiency as observed in the previous numerical examples.

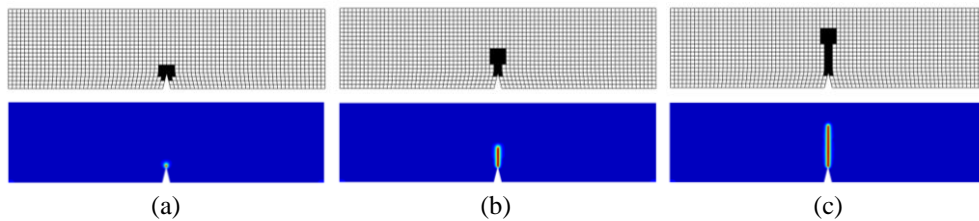


Fig. 5.10. Mesh geometries and crack patterns for the symmetric three-point bending problem when (a) $\delta = 0.04699$ mm (2615 nodes and 2442 elements), (b) $\delta = 0.04799$ mm (3133 nodes and 2946 elements) and (c) $\delta = 0.05439$ mm (3798 nodes and 3576 elements).

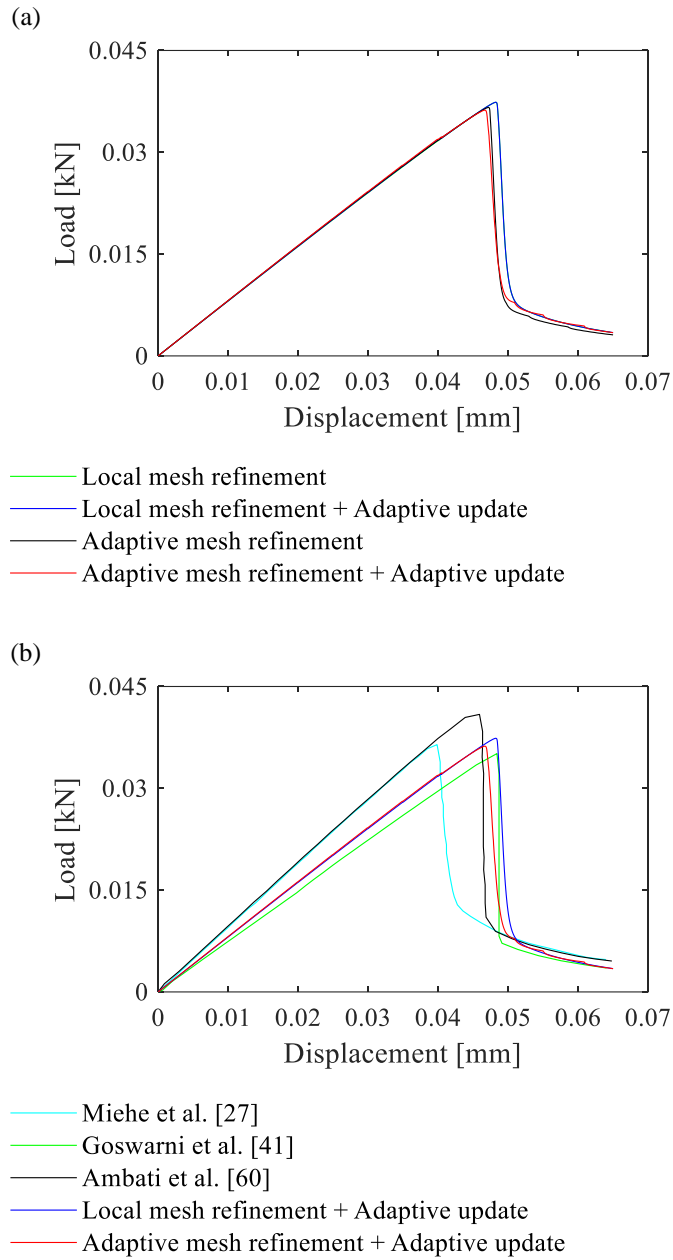


Fig. 5.11. Load-displacement curves on the symmetric three-point bending problem: (a) when the adaptive update scheme is used and when it is not used, and (b) when compared with previous results.

Table 5.5. Computation times required for the symmetric three-point bending problem in Fig. 5.9.

Numerical schemes applied	Computation time	
	[sec]	Ratio [%]
Local mesh refinement	21770.49	100.00
Local mesh refinement + Adaptive update	13861.82	63.67
Adaptive mesh refinement	5496.56	100.00
Adaptive mesh refinement + Adaptive update	2959.41	53.84

5.3.4. Notched plate with three holes

In this section, we consider a notched plate with three holes, whose geometry and boundary conditions are shown in Fig. 5.12 [39, 43, 44, 48, 60]. There are three holes: top, middle and bottom. A vertical displacement is prescribed along the perimeter of the top hole, and the perimeter of the bottom hole is fixed. Material properties are given as Lamé's constants $\lambda = 1.94$ GPa and $\mu = 2.45$ GPa, and the critical energy release rate $G_c = 2.28 \times 10^{-3}$ kN/mm. The regularization parameter is $l_0 = 0.5$ mm. The near-tip domain radius R_c is 4 mm.

For the local mesh refinement scheme, the mesh geometry (7512 elements) used is shown in Fig. 5.12(b). For the adaptive mesh refinement scheme, the initial mesh geometry (2223 elements) shown in Fig. 5.12(c) is used. For displacement control, the prescribed displacement δ is increased up to 1.10 mm. The number of the total incremental load step is 1100 and $\beta(t)$ increases uniformly.

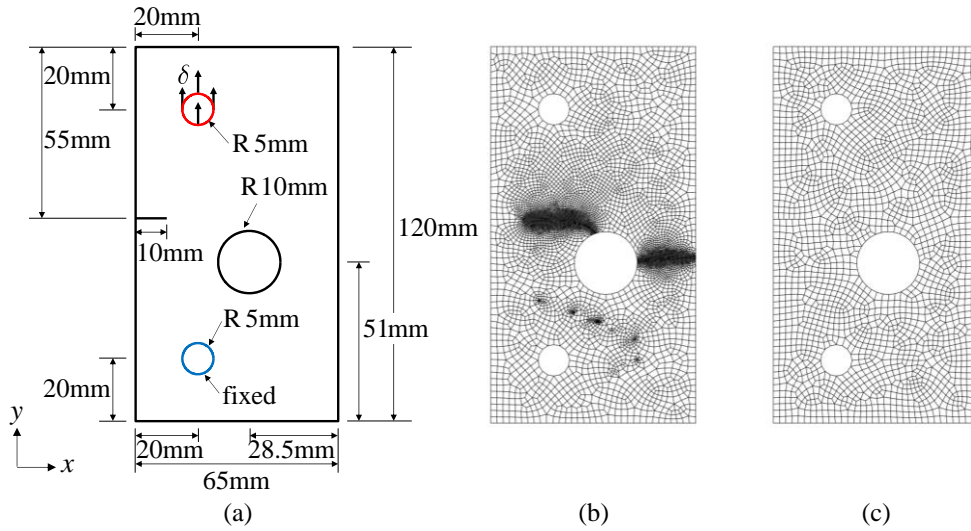


Fig. 5.12. Notched plate with three holes: (a) geometry and boundary conditions, (b) mesh geometry for the local mesh refinement scheme, and (c) initial mesh geometry for the adaptive mesh refinement scheme.

When the adaptive mesh refinement scheme is adopted, the mesh geometries and crack patterns vary during crack propagation, as depicted in Fig. 5.13. The load-displacement curves are shown in Fig. 5.14 for the four analysis cases. In the curves, the load is the total reaction force in the y-direction along the perimeter of the top hole. Fig. 5.15 gives the load-displacement curves compared with results in previous studies [39, 43, 44, 60]. It is observed that the curves obtained using the proposed scheme are similar with the most recent result [44] but different from the others. Fig. 5.16 shows the calculated crack path compared with the numerical and experimental results by Ambati et al. [60]. Note that the other studies also show very similar crack paths. Table 5.6 presents the computation times for the analysis cases. The improved computational efficiency by the adaptive update scheme is consistently observed.

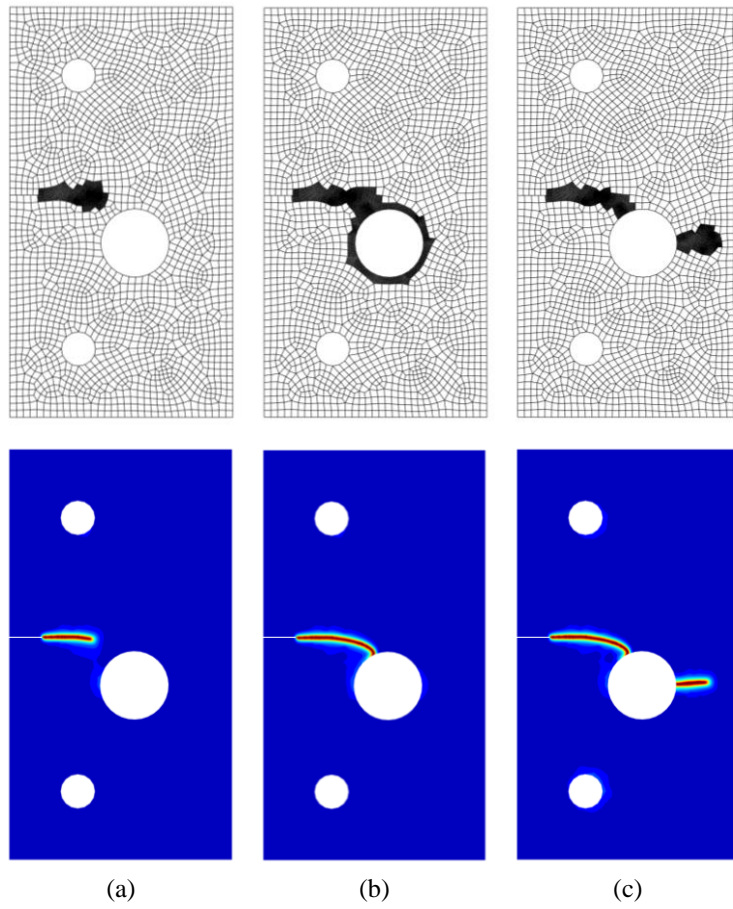


Fig. 5.13. Mesh geometries and crack patterns for the notched plate with three holes when (a) $\delta = 0.379$ mm (4794 nodes and 4554 elements), (b) $\delta = 0.599$ mm (7699 nodes and 7200 elements), and (c) $\delta = 1.039$ mm (6985 nodes and 6633 elements).

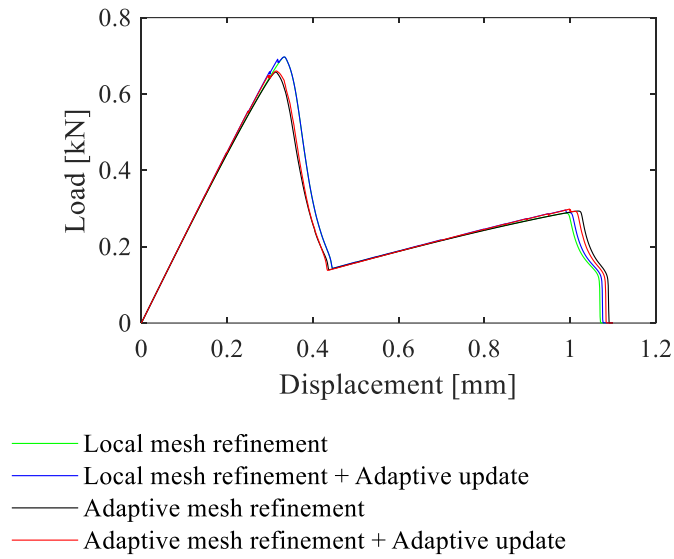


Fig. 5.14. Load-displacement curves on the notched plate with three holes when the adaptive update scheme is used and when it is not used.

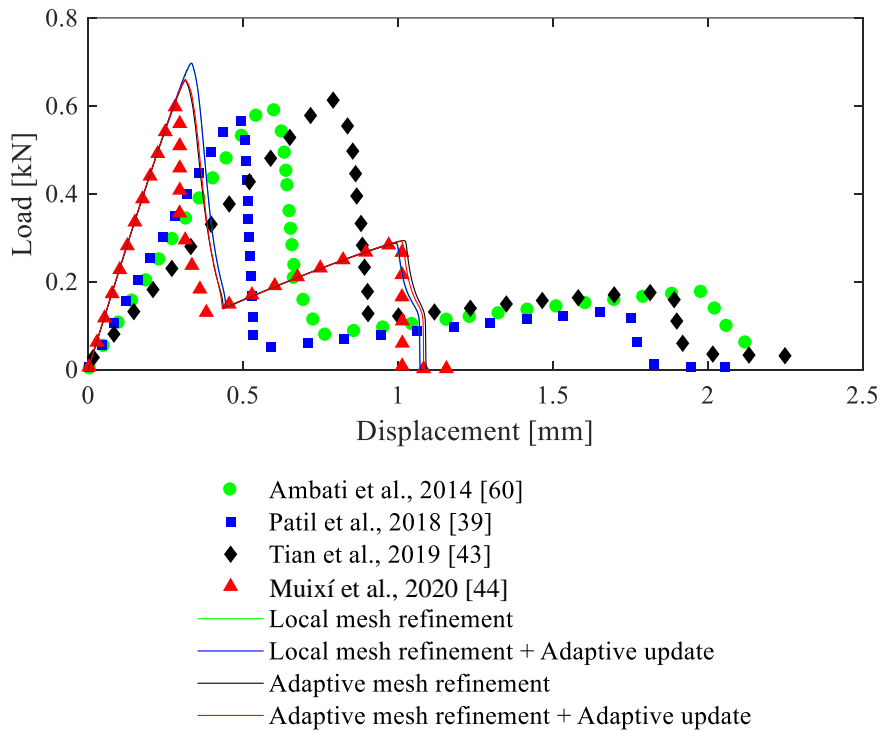


Fig. 5.15. Load-displacement curves on the notched plate with three holes when compared with results in previous studies.

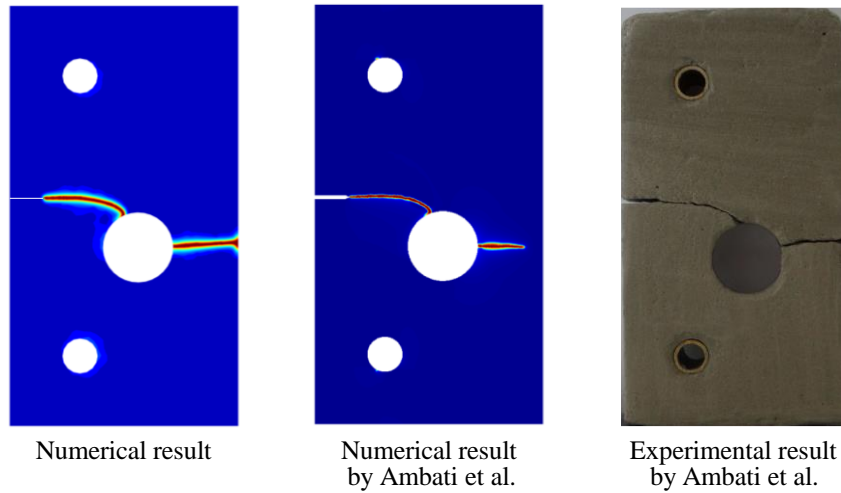


Fig. 5.16. Calculated crack path compared with the numerical and experimental results by Ambati et al. [60]. The numerical solution is obtained by using the adaptive update scheme with the adaptive mesh refinement scheme.

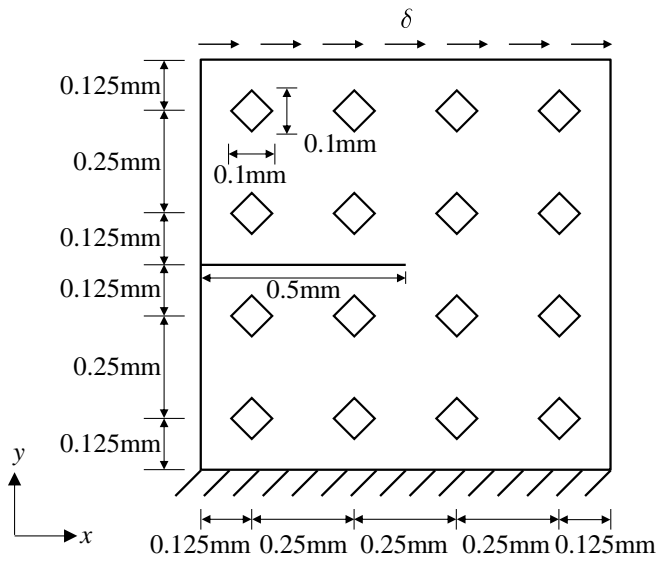
Table 5.6. Computation times required for the notched plate with three holes in Fig. 5.12.

Numerical schemes applied	Computation time	
	[sec]	Ratio [%]
Local mesh refinement	6917.37	100.00
Local mesh refinement + Adaptive update	4565.42	66.00
Adaptive mesh refinement	4146.08	100.00
Adaptive mesh refinement + Adaptive update	2359.78	56.92

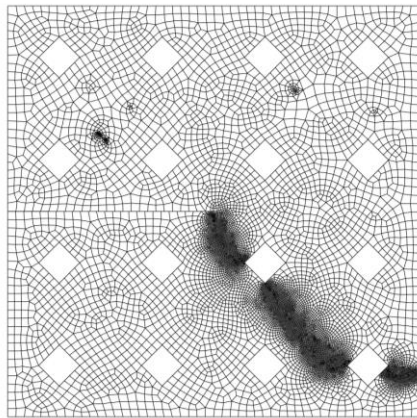
5.3.5. Single-edge notched shear plate with diamond-shaped holes

Let us consider a square plate including a single-edge crack with diamond-shaped holes as described in Fig. 5.17(a) [48]. The plate is subjected to a prescribed horizontal displacement along the top edge, and its bottom edge is fixed. Young's modulus, Poisson's ratio, and the critical energy release rate are $E = 210$ GPa, $\nu = 0.3$, and $G_c = 2.7 \times 10^{-3}$ kN/mm, respectively. The regularization parameter is $l_0 = 0.0075$ mm. The near-tip domain radius R_c is 0.04 mm.

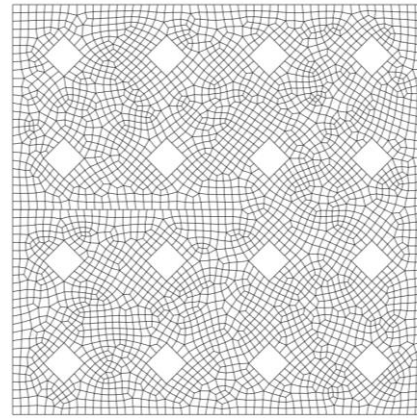
The mesh geometry (10922 elements) used for the local mesh refinement scheme is shown in Fig. 5.17(b), and the initial mesh geometry (3231 elements) used for the adaptive mesh refinement scheme is shown in Fig. 5.17(c). The prescribed displacement δ increases up to 0.015 mm. The number of the total incremental load step is 1500 and $\beta(t)$ uniformly increases.



(a)



(b)



(c)

Fig. 5.17. Single-edge notched shear plate with diamond-shaped holes: (a) geometry and boundary conditions, (b) mesh geometry for the local mesh refinement scheme, and (c) initial geometry for the adaptive mesh refinement scheme.

Fig. 5.18 describes the mesh geometries and crack patterns formed by the adaptive mesh refinement scheme. For the four analysis cases, the load-displacement curves are drawn in Fig. 5.19. The load is the total reaction force along the top edge in the x -direction. The computation times required for the four cases are presented in Table 5.7. It is clearly shown that the adaptive update scheme reduces the computation time by about 40% to 50% with almost no change in the solutions.

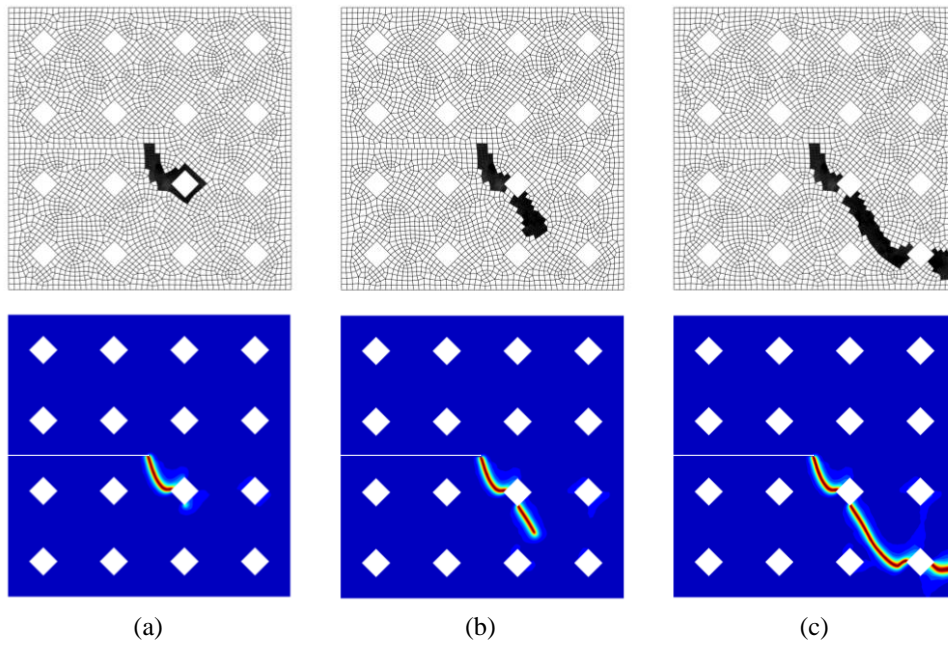


Fig. 5.18. Mesh geometries and crack patterns for the single-edge notched shear plate with diamond-shaped holes when (a) $\delta = 0.01139$ mm (6933 nodes and 6457 elements), (b) $\delta = 0.01249$ mm (7941 nodes and 7465 elements) and (c) $\delta = 0.01449$ mm (12771 nodes and 12064 elements).

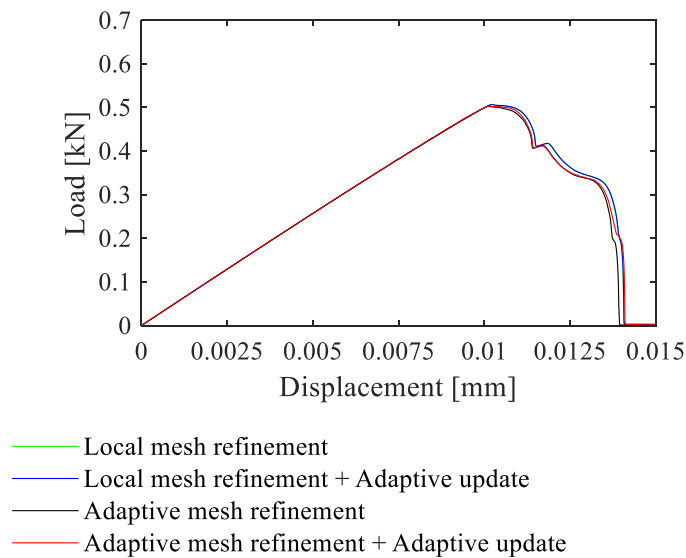


Fig. 5.19. Load-displacement curves on the single-edge notched shear plate with diamond-shaped holes when the adaptive update scheme is used and when it is not used.

Table 5.7. Computation times required for the single-edge notched shear with diamond-shaped holes in Fig. 5.17.

Numerical schemes applied	Computation time	
	[sec]	Ratio [%]
Local mesh refinement	14624.72	100.00
Local mesh refinement + Adaptive update	8907.93	60.91
Adaptive mesh refinement	5043.26	100.00
Adaptive mesh refinement + Adaptive update	2928.41	58.07

5.3.6. L-shaped panel

An L-shaped panel is considered as illustrated in Fig. 5.20(a) [40, 42, 48, 71]. The prescribed displacement δ is applied at point B. Young's modulus, Poisson's ratio, and the critical energy release rate are given by $E = 25.85$ GPa, $\nu = 0.18$, and $G_c = 95$ N/m, respectively. The regularization parameter is $l_0 = 2$ mm. The radius to determine the near-tip domain (R_c) is 15mm.

For the local mesh refinement scheme, the mesh geometry (19501 elements) used is shown in Fig. 5.20(b). For the adaptive mesh refinement scheme, the initial mesh geometry (3718 elements) shown in Fig. 5.20(c) is used. The prescribed displacement δ_0 is applied until 1mm, the number of the total incremental load step is 2000, and increases uniformly.

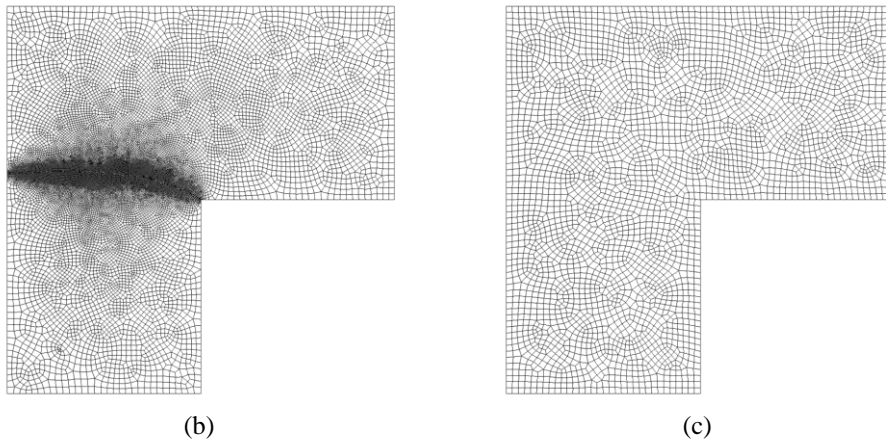
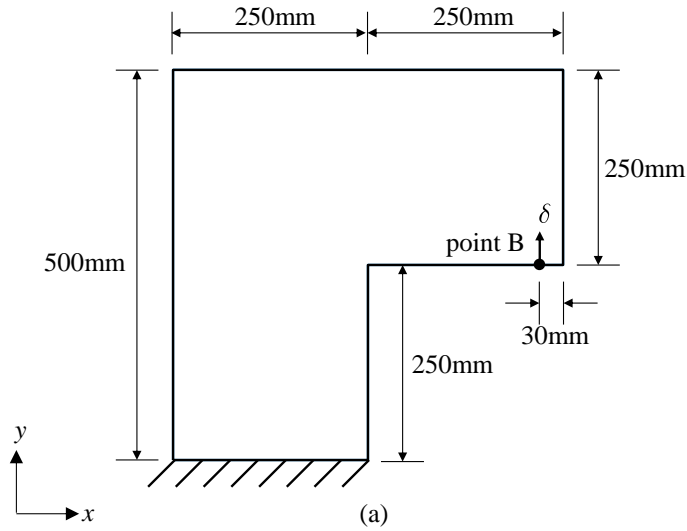


Fig. 5.20. L-shaped panel: (a) geometry and boundary conditions, (b) mesh geometry for the local mesh refinement scheme and (c) initial mesh geometry for the adaptive mesh refinement scheme.

Fig. 5.21 illustrates the mesh geometries and crack patterns created by the adaptive mesh refinement scheme during crack propagation. Fig. 5.22(a) presents the load-displacement curves for the four analysis cases. In the curves, the load is the reaction force in the y-direction at point B. Fig. 5.22(b) displays the load-displacement curves calculated by Patil et al. [40] and Hirshikesh et al. [42]. Fig. 5.23 shows the calculated crack path compared with the experimental result by Winkler [71]. Table 5.8 gives the computation times with and without the adaptive update scheme together with the local and adaptive mesh refinement schemes. The proposed adaptive update scheme provides improved computational efficiency as observed in the previous numerical examples.

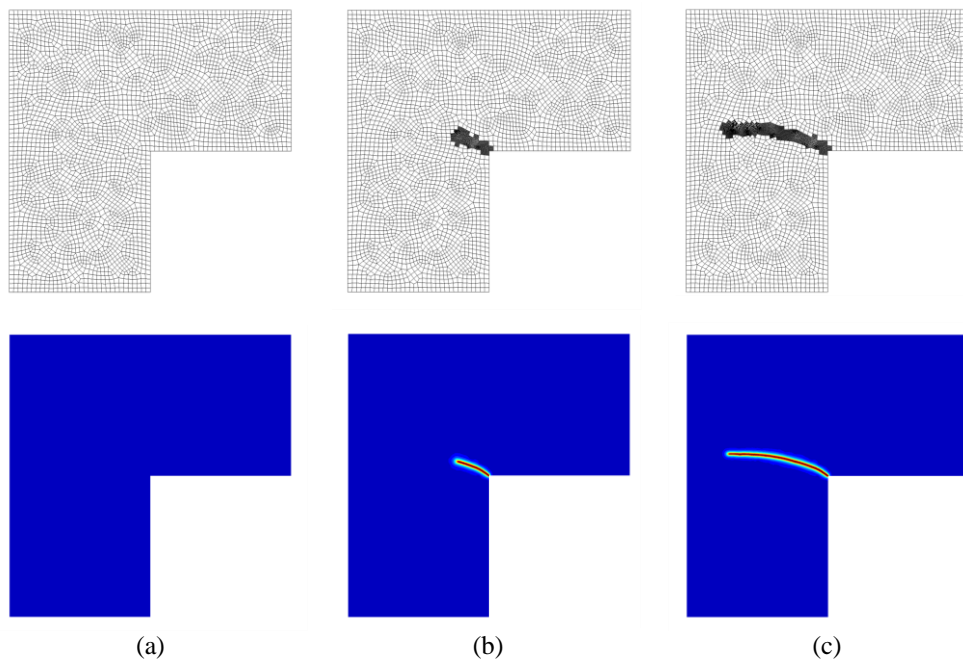
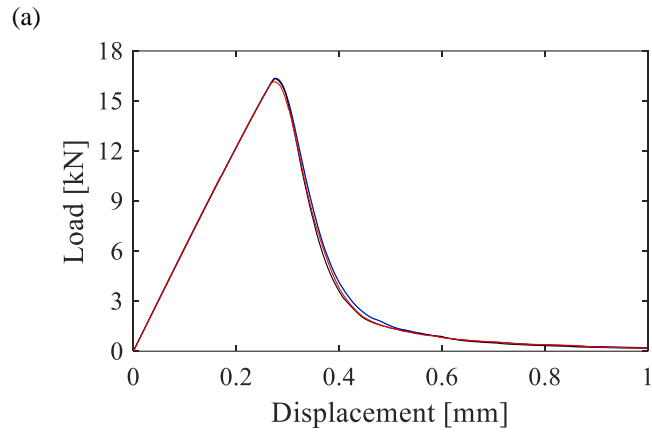
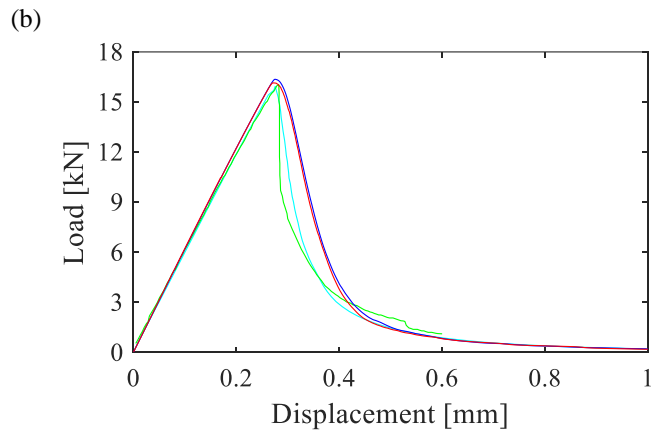


Fig. 5.21. Mesh geometries and crack patterns for the L-shaped panel when (a) $\delta = 0.0995$ mm (3847 nodes and 3718 elements), (b) $\delta = 0.3245$ mm (5982 nodes and 5734 elements), and (c) $\delta = 0.4495$ mm (10224 nodes and 9830 elements).



- Local mesh refinement
- Local mesh refinement + Adaptive update
- Adaptive mesh refinement
- Adaptive mesh refinement + Adaptive update



- Patil et al. [40]
- Hirshikesh et al. [42]
- Local mesh refinement + Adaptive update
- Adaptive mesh refinement + Adaptive update

Fig. 5.22. Load-displacement curves on the L-shaped panel: (a) when the adaptive update scheme is used and when it is not used, and (b) when compared with previous results.

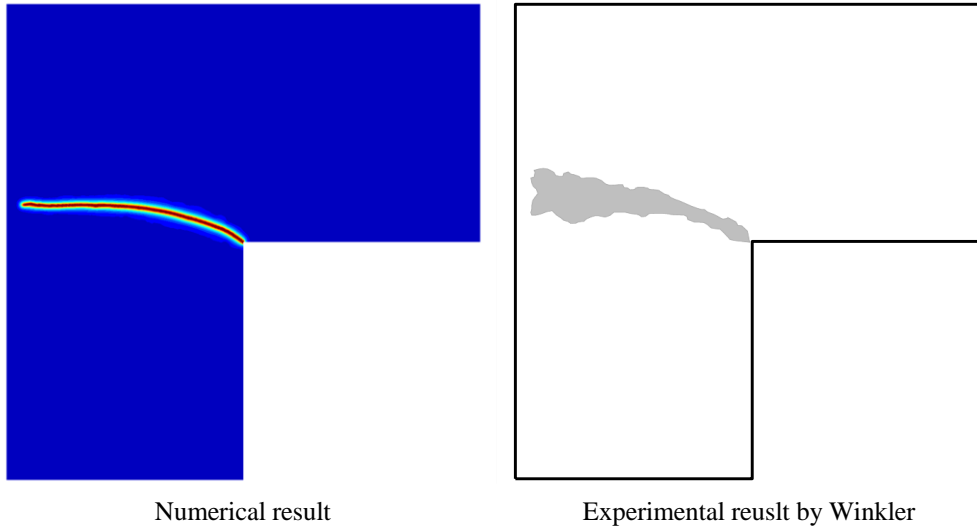


Fig. 5.23. Calculated crack path compared with the experimental result [71]. The numerical solution is obtained by using the adaptive update scheme with the adaptive mesh refinement scheme.

Table 5.8. Computation times required for the L-shaped panel in Fig. 5.20.

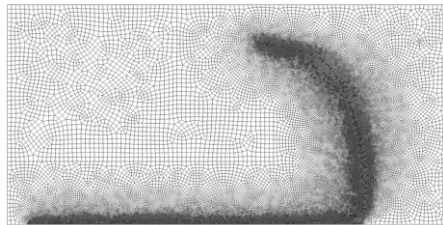
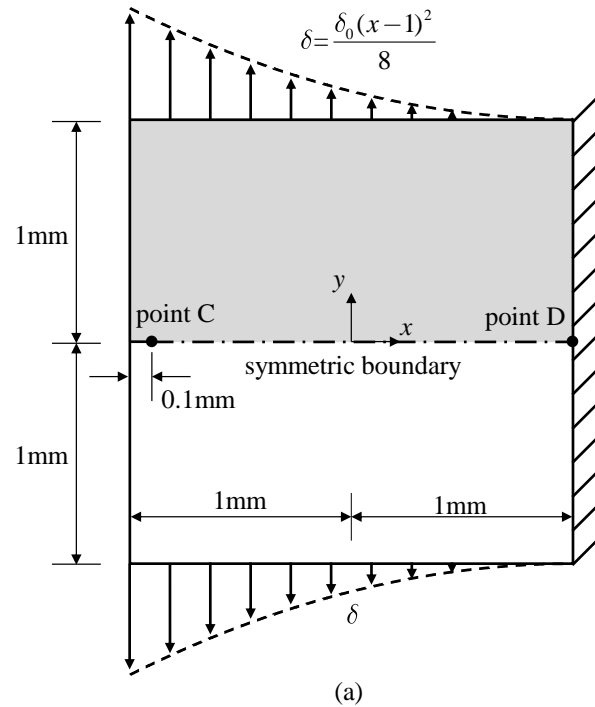
Numerical schemes applied	Computation time	
	[sec]	Ratio [%]
Local mesh refinement	33347.53	100.00
Local mesh refinement + Adaptive update	21775.64	65.30
Adaptive mesh refinement	9719.60	100.00
Adaptive mesh refinement + Adaptive update	5733.24	58.99

5.3.7. Single-edged notched branching problem

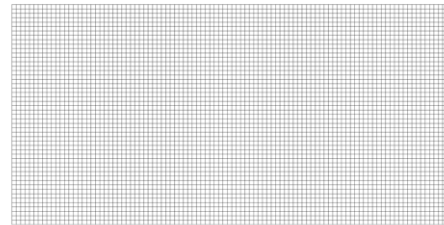
Finally, the single-edged notched branching problem proposed by Muixí et al. [44-46, 48] is solved. Consider a square plate with a single-edge crack of 0.1mm as shown in Fig. 5.24(a). The prescribed displacement $\delta = \frac{\delta_0(x-1)^2}{8}$ is applied along the top and bottom edges of the plate, and the right edge of the plate is fixed. Due to symmetry, we model only one-half of the plate with symmetric boundary conditions along point CD as depicted in Fig. 5.24 (a). Young's modulus, Poisson's ratio, and the critical energy release rate are $E = 20$ GPa, $\nu = 0.3$, and $G_c = 8.9 \times 10^{-5}$ kN/mm, respectively. The regularization parameter is $l_0 = 0.005$ mm. The near-tip domain radius R_c is 0.04mm.

The mesh geometry (54625 elements) in Fig. 5.24(b) is used for the local mesh refinement scheme, and the regular

mesh of 50×100 elements in Fig. 5.24(c) is used for the adaptive mesh refinement scheme. The prescribed displacement δ_0 increases up to 0.1mm for displacement control. The number of the total incremental load step is 1000 and $\beta(t)$ uniformly increases.



(b)



(c)

Fig. 5.24. Single-edge notched branching problem: (a) geometry and boundary conditions, (b) mesh geometry for the local mesh refinement scheme and (c) initial mesh geometry for the adaptive mesh refinement scheme.

Fig. 5.25 describes the mesh geometries and crack patterns formed by the adaptive mesh refinement scheme. Fig. 5.26 shows the crack paths calculated by the full and half models compared with the path of the full model solution in Refs. [44, 46]. Note that the half and full model solutions calculated using the proposed scheme are identical and similar with the recent result in Ref. [46]. The load-displacement curves for the four analysis cases are drawn in Fig. 5.27. The only previously published load-displacement curve in Ref. [44] is plotted together although it does not well match with our results. The load is the total reaction force along the top edge in the y-direction and

the displacement is considered as δ . The computation times required for the four cases are presented in Table 5.9. It is clearly shown that the adaptive update scheme reduces the computation time by about 40% to 50% with almost no change in the solutions.

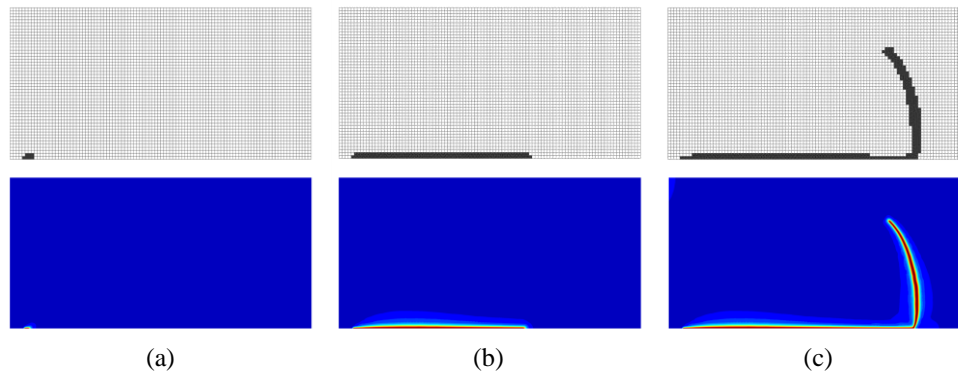


Fig. 5.25. Mesh geometries and crack patterns for the single-edge notched branching problem when (a) $\delta_0 = 0.0099$ mm (5634 nodes and 5441 elements), (b) $\delta_0 = 0.0299$ mm (12830 nodes and 12245 elements), and (c) $\delta_0 = 0.0849$ mm (22679 nodes and 21632 elements).

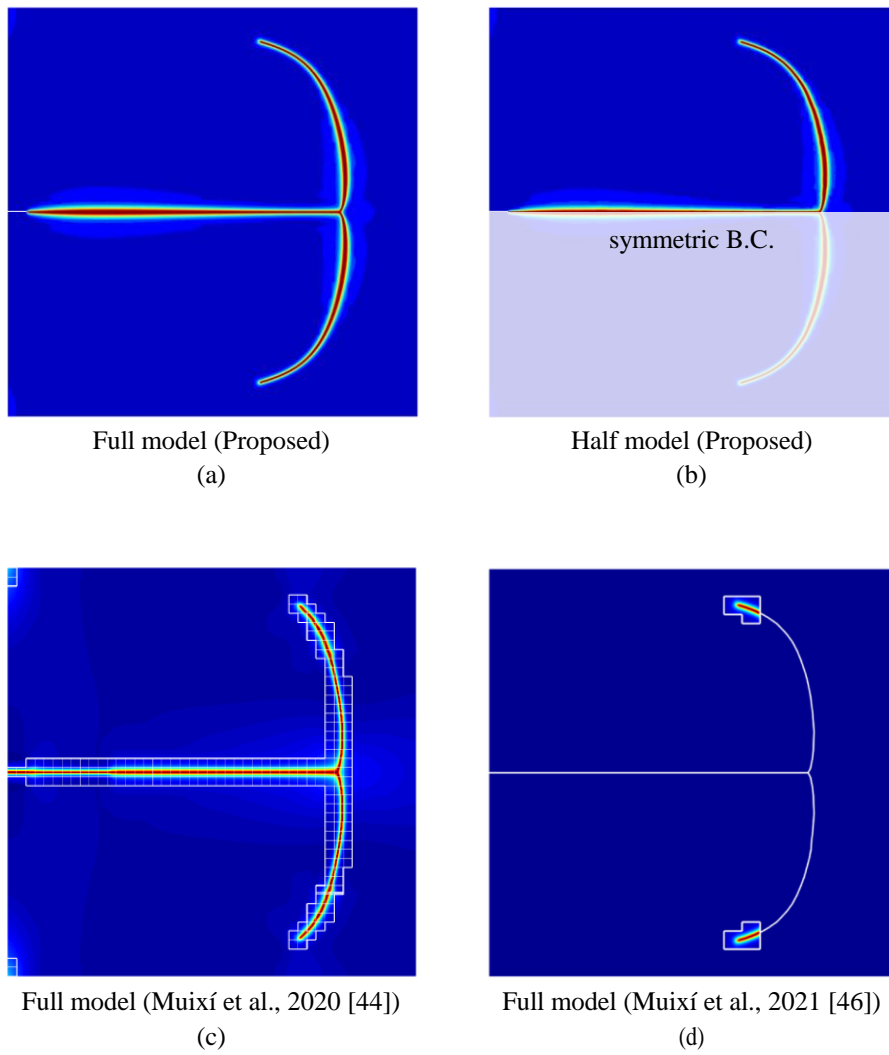


Fig. 5.26. Crack paths calculated by (a) the full model and, (b) the half model with symmetric boundary conditions compared with those by the full models by Muixí et al. in (c) Ref. [44] and (d) Ref. [46]. The crack paths with the proposed method are obtained by using the adaptive update scheme with the adaptive mesh refinement scheme.

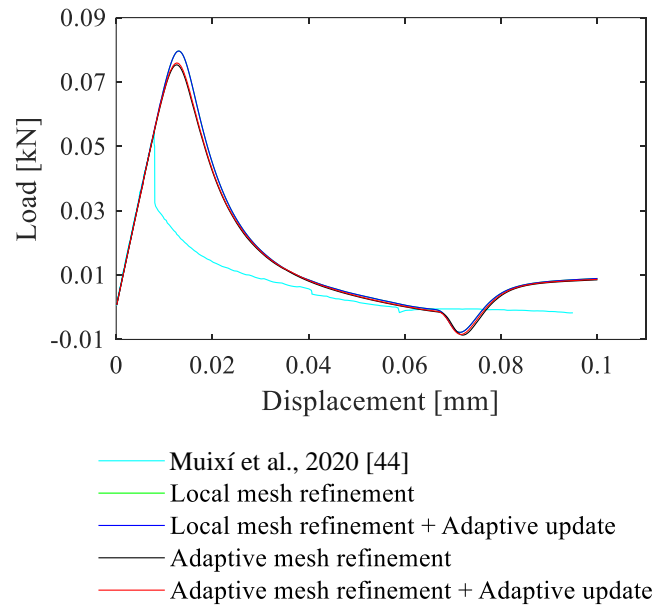


Fig. 5.27. Load-displacement curves on the single-edge notched branching problem when the adaptive update scheme is used and when it is not used.

Table 5.9. Computation times required for the single-edge notched branching problem in Fig. 5.24.

Numerical schemes applied	Computation time	
	[sec]	Ratio [%]
Local mesh refinement	31231.21	100.00
Local mesh refinement + Adaptive update	21358.76	68.39
Adaptive mesh refinement	10910.54	100.00
Adaptive mesh refinement + Adaptive update	6454.63	59.16

Chapter 6. Mesh coarsening using the phantom-node method in the phase field model

In this section, we briefly review the phantom-node method. We then present a method to adaptively coarsen mesh in the domain where a crack already propagated by applying the phantom-node method to the phase field model.

6.1. Review of the phantom-node method

The phantom-node method is proposed by Hansbo and Hansbo [75], which is widely used and has successfully expanding to smoothed FEM [76], shell problem [77] and so on [20, 21]. The main advantage is that cracks can be modeled without re-meshing and additional nodes.

As illustrated in Fig. 6.1, a fully cracked element (Ω^{E0}) is decomposed into two superimposed elements (E1 and E2) having two real domains (Ω_R^{E1} and Ω_R^{E2}) and two virtual domains (Ω_V^{E1} and Ω_V^{E2}), respectively. Doing so, the displacement field of the cracked element can be expressed as

$$\mathbf{u}_{cr}^{(m)} = \begin{cases} \mathbf{u}_R^{E1} & \text{in } \Omega_R^{E1} \\ \mathbf{u}_R^{E2} & \text{in } \Omega_R^{E2} \end{cases}, \quad (6.1)$$

where \mathbf{u}_R^{E1} and \mathbf{u}_R^{E2} are the displacement field of the two superimposed elements (E1 and E2) in Ω_R^{E1} and Ω_R^{E2} , respectively.

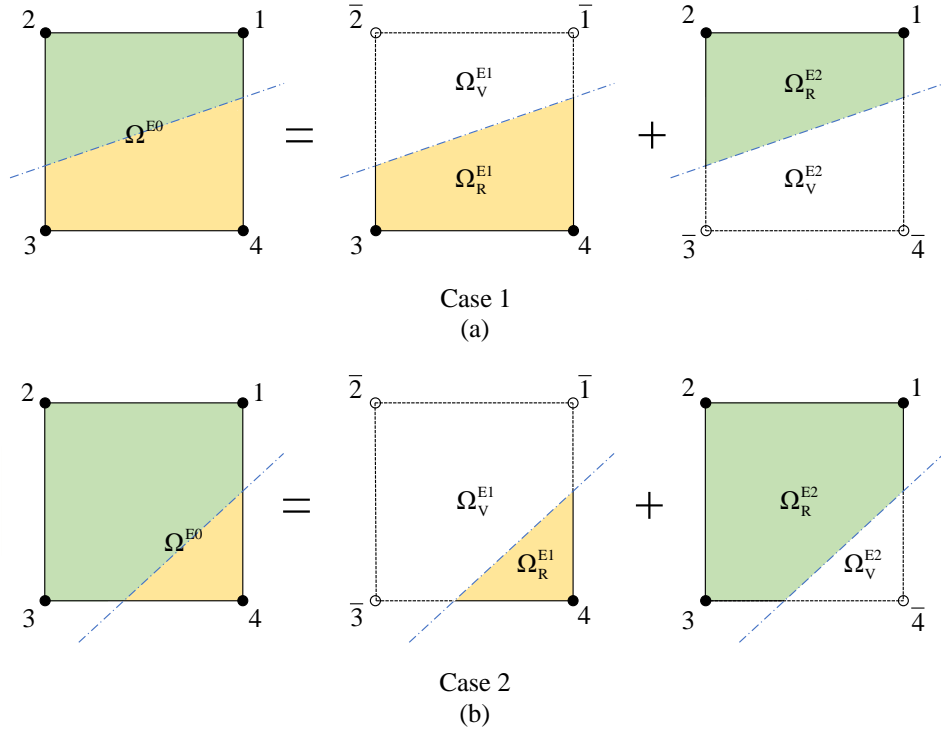


Fig. 6.1. Two superimposed elements having (E1 and E2) two real domains (Ω_R^{E1} and Ω_R^{E2}) and two virtual domains (Ω_V^{E1} and Ω_V^{E2}), respectively.

In case that the cracked element is divided two quadrilateral domains as shown in Fig. 6.1(a), $N1 \in \{\bar{1}, \bar{2}, 3, 4\}$ is the node set of E1 and $N2 \in \{1, 2, \bar{3}, \bar{4}\}$ is the node set of E2. Note that bar over number (e.g. $\bar{1}, \bar{2}, \bar{3}, \bar{4}$) denotes the phantom nodes additionally introduced to represent the displacement fields separated by two superimposed elements. Fig. 6.1(b) illustrates a case in which the element is divided into one pentagonal domain and one triangular domain.

The phase field of the cracked element is also expressed as in the same manner

$$\phi_{cr}^{(m)} = \begin{cases} \sum_{i \in N1} h_i \phi_i & \text{in } \Omega_R^{E1} \\ \sum_{i \in N2} h_i \phi_i & \text{in } \Omega_R^{E2} \end{cases}, \quad (6.2)$$

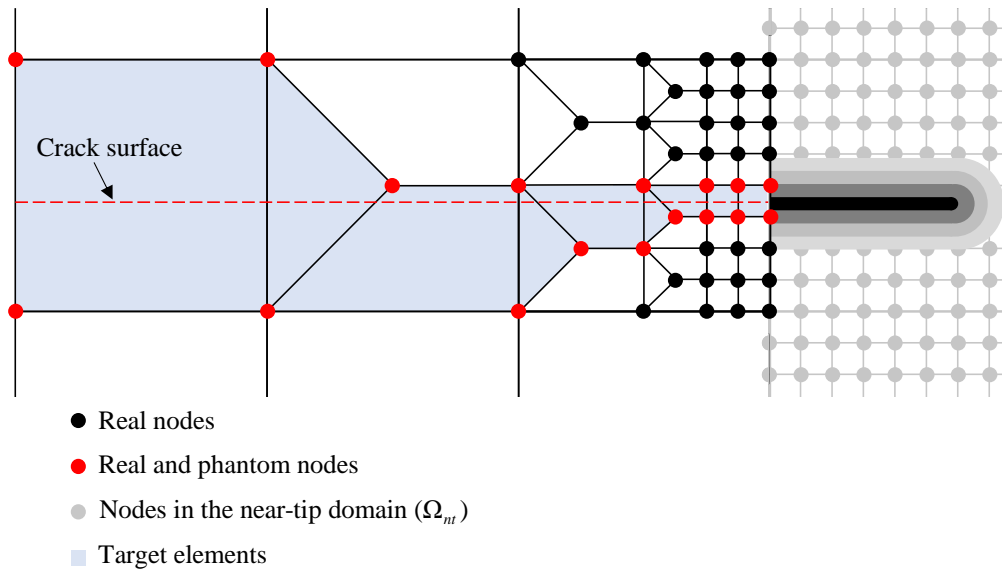


Fig. 6.3. Schematics of mesh connection modeled by the phantom-node method and phase field model, respectively.

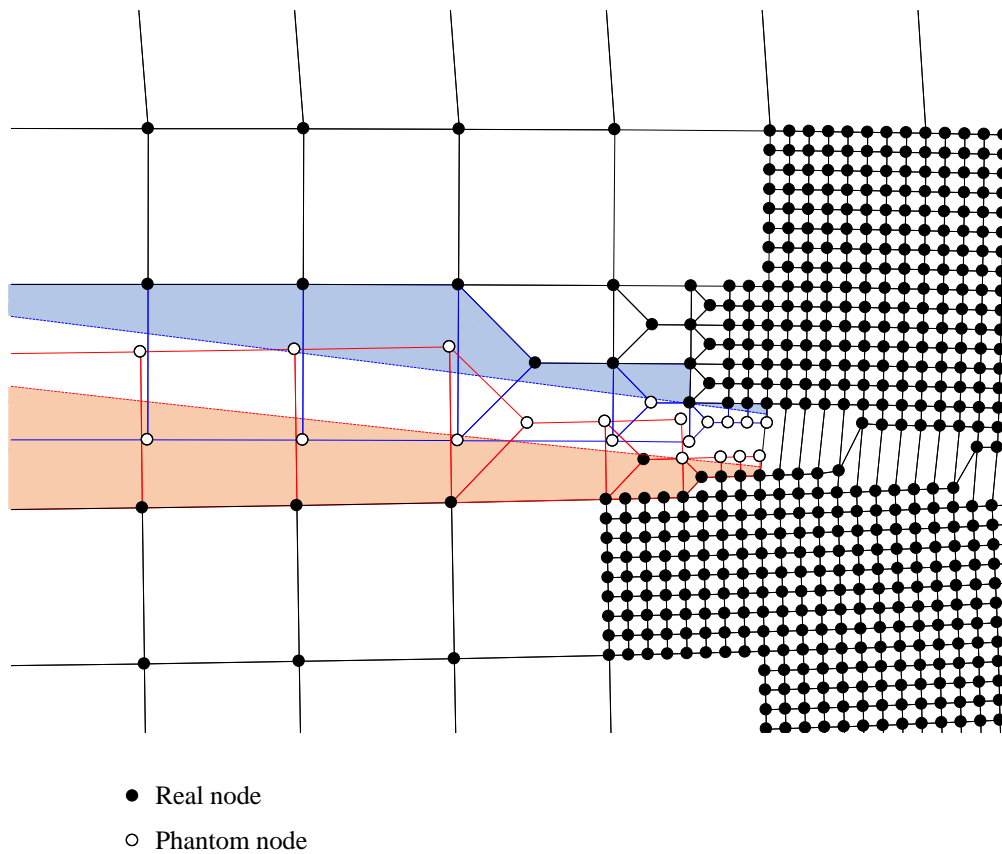


Fig. 6.4. Schematics of superimposed elements model by phantom-nodes.

6.3. Numerical examples

In this section, we investigate the performance of the proposed method through various numerical examples: the single-edge notched tension problem, the L-shaped panel, the notched cruciform plate, and the double-edged notched tension problem.

Ref. [48] reports that the use of both adaptive update and adaptive mesh refinement schemes maximizes the computational efficiency in the phase field model. We here investigate additional improvement in computational efficiency when the mesh coarsening method is adopted with the both adaptive schemes. Doing so, we consider two analysis cases:

- (Case 1) Both adaptive update and adaptive mesh refinement schemes are adopted without the mesh coarsening method. The adaptively refined mesh still remains where cracks already passed.
- (Case 2) Both adaptive update and adaptive mesh refinement schemes are adopted with the mesh coarsening method. Therefore, the fine mesh where cracks passed is restored to the coarse mesh.

We consider the plane strain condition in the numerical examples. The error tolerances for the displacement and phase fields (ε_u and ε_ϕ) are adjusted to 10^{-5} . We use the critical damage parameter $\phi_c = 0.5$. To detect crack initiation timely and to refine the mesh in the domain of crack initiation, the critical damage parameter $\phi_c = 0.1$ is used until the crack propagates, see Ref. [48]. The critical damage parameter $\phi_c = 0.5$ is after identification of the crack initiation domain.

In the phase field model, the element size should be determined to guarantee the solution accuracy. The following conditions are adopted as recommended in Ref. [28]:

$$l_e = 4.0l_0 \quad \text{for initial coarse mesh,} \quad (6.3)$$

$$l_e \leq 0.5l_0 \quad \text{for adaptive mesh refinement,} \quad (6.4)$$

where l_e represents the element size ($l_e = \sqrt{A_e}$ with an element area A_e).

The numerical procedure was implemented in MATLAB 2017a and the computation was performed on a PC with an Intel(R) Core(TM) i7-7700 CPU @ 3.60GHz and 64GB RAM.

6.3.1. Single-edged notched tension problem

Let us consider a square plate with a single-edge crack as described in Fig. 6.5(a) [27, 39, 43, 48]. The plate is subjected to a prescribed vertical displacement along the top edge, and the bottom edge of the plate is fixed. Young's modulus, Poisson's ratio, and the critical energy release rate are given by $E = 210 \text{ GPa}$, $\nu = 0.3$, and $G_c = 2.7 \times 10^{-3} \text{ kN/mm}$, respectively. The regularization parameter is $l_0 = 0.0075 \text{ mm}$. The radius R_c to determine the near-tip domain is 0.04 mm .

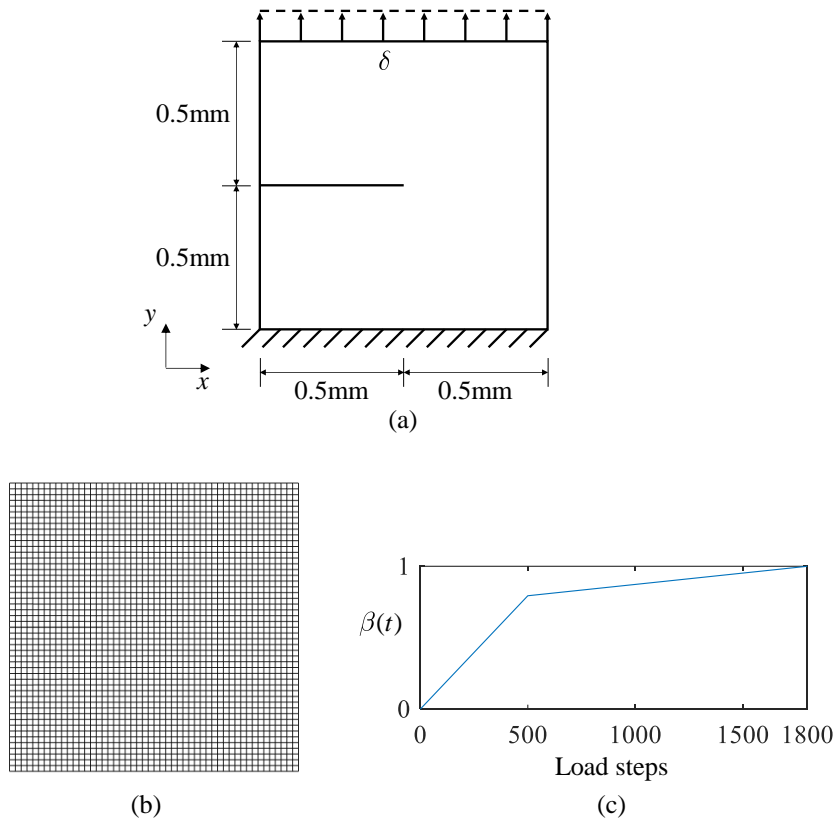


Fig. 6.5. Single-edge notched tension problem: (a) geometry and boundary conditions, (b) initial mesh geometry, and (c) load history curve.

We use the regular mesh of 50×50 elements in Fig. 6.5(b). The prescribed displacement δ increases up to 0.0063 mm for displacement control. The number of the total incremental load step is 1800 and the load parameter function $\beta(t)$ is given in Fig. 6.5(c).

When the mesh coarsening method is adopted (Case 2), changes in mesh geometry and crack pattern during crack propagation are illustrated in Fig. 6.6. Fig. 13 shows the mesh geometries without and with adopting the mesh

coarsening method. Unlike Fig. 6.7(a), Fig. 6.7(b) presents that the fine mesh where cracks passed is restored to the coarse mesh. For the two analysis cases, the load-displacement curves are plotted in Fig 6.8. In the curves, the load is the total reaction force in the y-direction along the top edge. The previous results of Miehe et al. [27], Patil et al. [39], and Tian et al. [43] are plotted together.

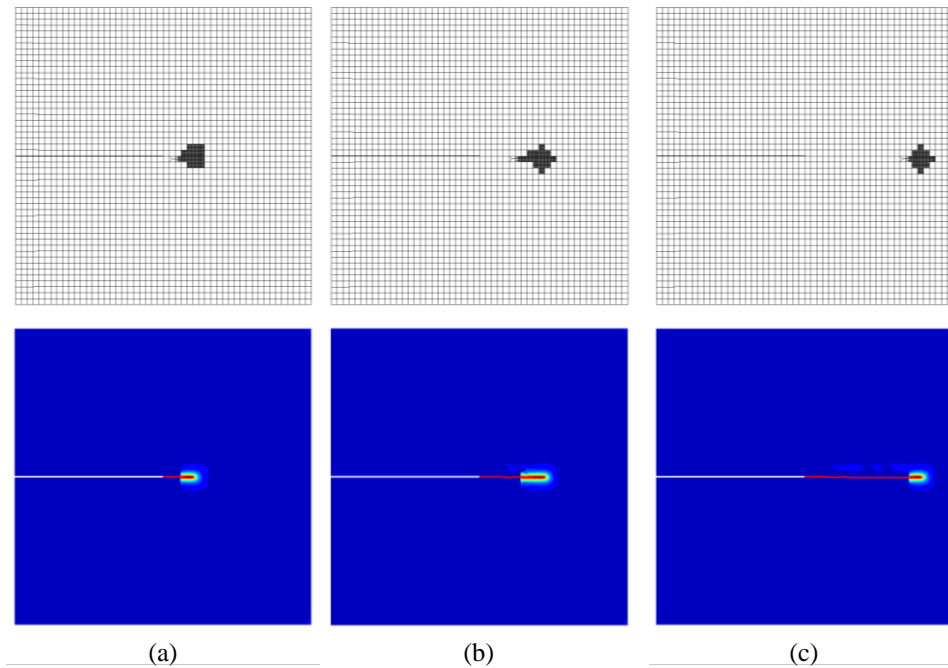


Fig. 6.6. Mesh geometries and crack patterns for the single-edge notched tension problem when (a) $\delta = 0.00555$ mm, (b) $\delta = 0.0057$ mm, and (c) $\delta = 0.0059$ mm.

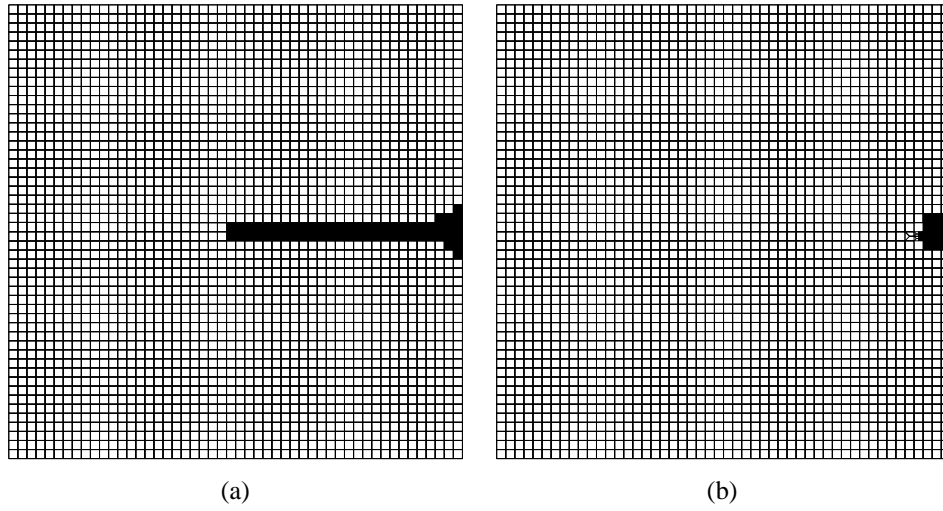


Fig. 6.7. Mesh geometries: (a) without and (b) with mesh coarsening.

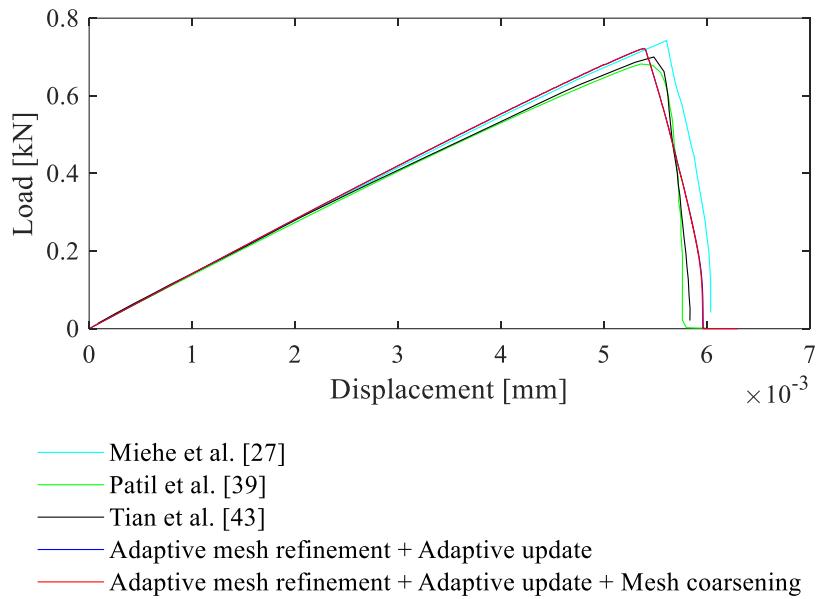


Fig. 6.8. Load-displacement curves on the single-edge notched tension problem.

Table 6.1 shows the normalized computation times comparing Case 1 with Case 2. After crack propagation, reduction in computational time is more noticeable. In particular, computation time required to solve Eqs. (2.24) and (2.25) are significantly reduced.

Table 6.1. Normalized computation times required for the single-edge notched tension problem in Fig. 6.5. (Case 1) Adaptive mesh refinement + Adaptive update, (Case 2) Adaptive mesh refinement+ Adaptive update+ Mesh coarsening.

Cases	Whole time step		After crack propagation	
	Total	Equation solving	Total	Equation solving
Case 1	100 %	100 %	100 %	100 %
Case 2	88.78 %	69.37 %	83.55 %	63.36 %

6.3.2. L-shaped panel

An L-shaped panel is considered as illustrated in Fig. 6.9(a) [40, 42, 48, 71]. The prescribed displacement δ is applied at point B. Young's modulus $E = 25.85$ GPa, Poisson's ratio $\nu = 0.18$, and the critical energy release rate $G_c = 95$ N/m. The regularization parameter is $l_0 = 2$ mm. The radius to determine the near-tip domain (R_c) is 15 mm.

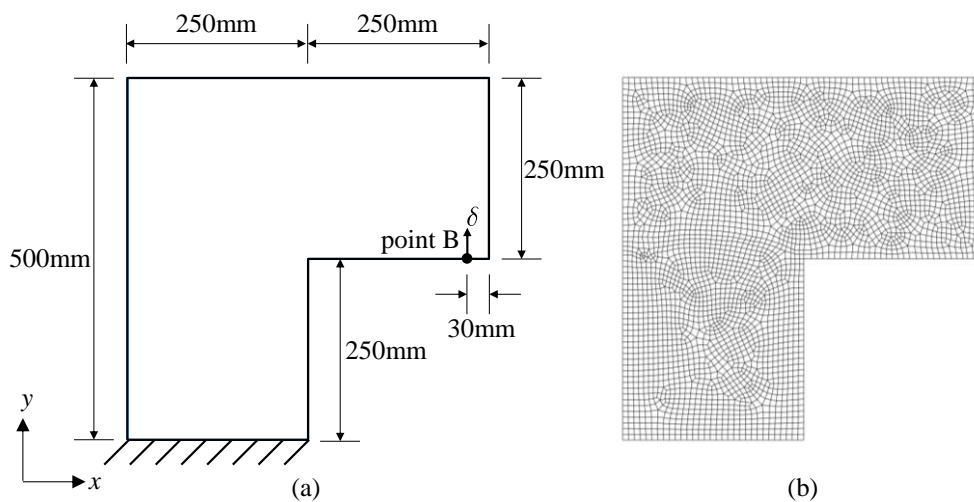


Fig. 6.9. L-shaped panel: (a) geometry and boundary conditions and (b) initial mesh geometry.

The initial mesh geometry (3718 elements) used is shown in Fig. 6.9(b). The prescribed displacement δ is applied until 1mm, the number of the total incremental load step is 2000, and $\beta(t)$ increases uniformly.

Fig. 6.10 illustrates the mesh geometries and crack patterns during crack propagation when the mesh coarsening

method is applied. Fig. 6.11 presents the load-displacement curves for the two analysis cases compared with those by Patil et al. [40] and Hirshikesh et al. [42]. The load is the reaction force in the y -direction at point B. Fig. 6.12 shows the calculated crack path compared with the experimental result by Winkler [71].

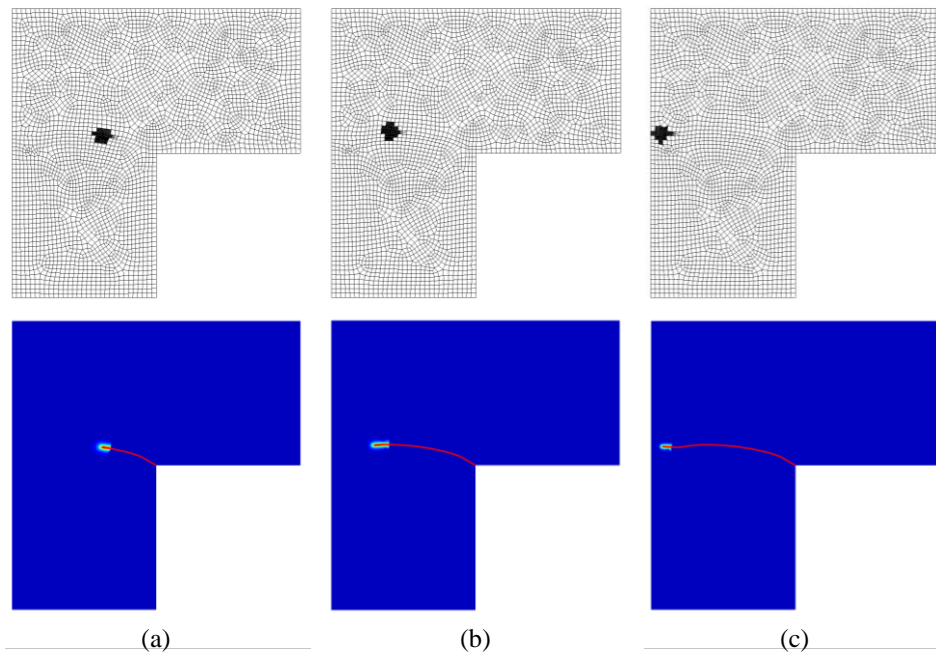


Fig. 6.10. Mesh geometries and crack patterns for the L-shaped panel when (a) $\delta = 0.35$ mm, (b) $\delta = 0.4$ mm, and (c) $\delta = 0.95$ mm.

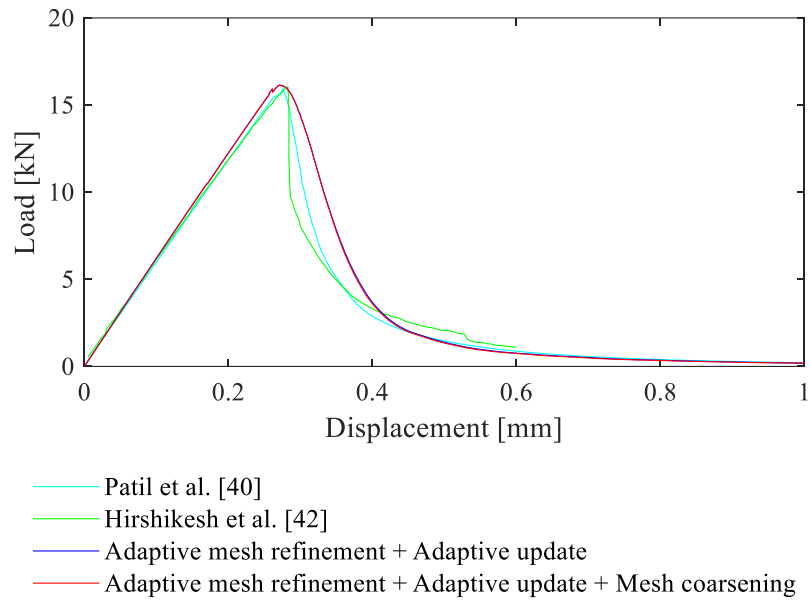


Fig. 6.11. Load-displacement curves on the L-shaped panel.

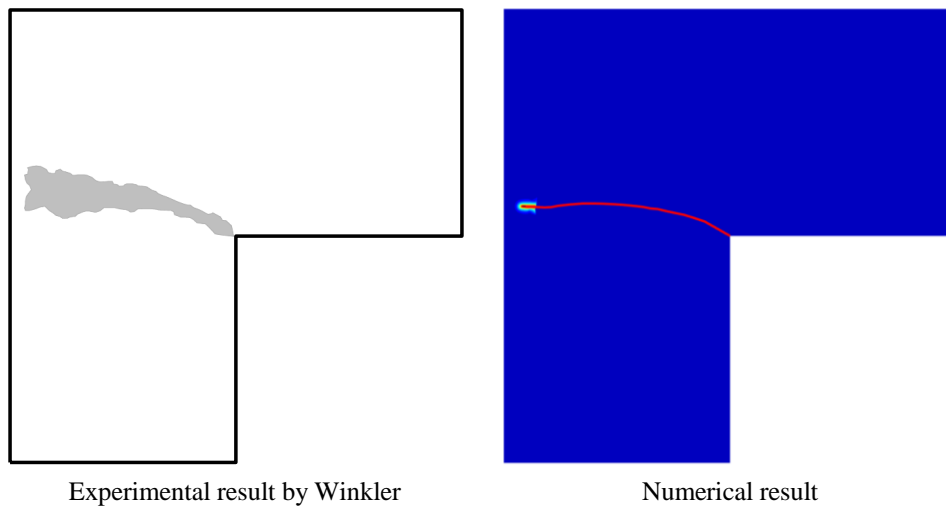


Fig. 6.12. Calculated crack path compared with the experimental result [71]. The numerical solution is obtained by mesh coarsening with the adaptive update and mesh refinement schemes.

Table 6.2 gives the normalized computation times without and with adopting the mesh coarsening method. As expected, the mesh coarsening method improves computational efficiency in the phase field model. In addition, Fig. 6.13 shows the total number of degrees of freedom required during simulation for the two cases. After a crack initiates, the required number of DOFs significantly decreases.

Table 6.2. Normalized computation times required for the L-shaped panel in Fig. 6.9. (Case 1) Adaptive mesh refinement + Adaptive update, (Case 2) Adaptive mesh refinement+ Adaptive update+ Mesh coarsening.

Cases	Whole time step		After crack propagation	
	Total	Equation solving	Total	Equation solving
Case 1	100 %	100 %	100 %	100 %
Case 2	77.54 %	54.66 %	69.25 %	48.23 %

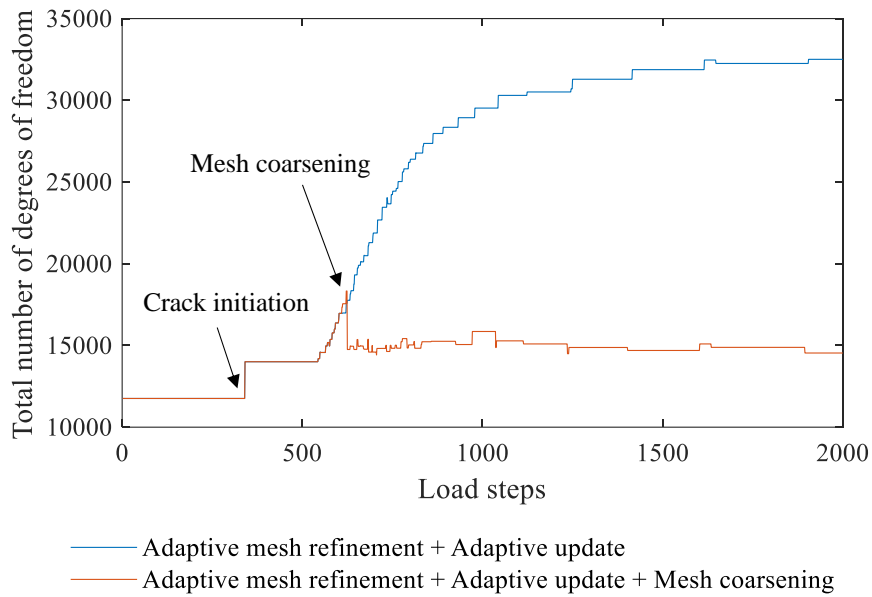


Fig. 6.13. Histories of the total number of degrees of freedom for the L-shaped panel.

6.3.3. Notched cruciform plate

A notched cruciform plate is considered as shown in Fig. 6.14(a) [48, 78, 79, 80]. A vertical displacement is uniformly applied along the top edge of the plate. The bottom edge of the plate is fixed in the y -direction. The left and right edges of the plate are fixed in the x -direction. Young's modulus, Poisson's ratio, and the critical energy release rate are given: $E = 0.2184 \text{ MPa}$, $\nu = 0.2$, and $G_c = 2.0 \times 10^{-10} \text{ kN/mm}$. The regularization parameter is $l_0 = 0.625 \text{ mm}$. The radius to determine the near-tip domain (R_c) is 5mm.

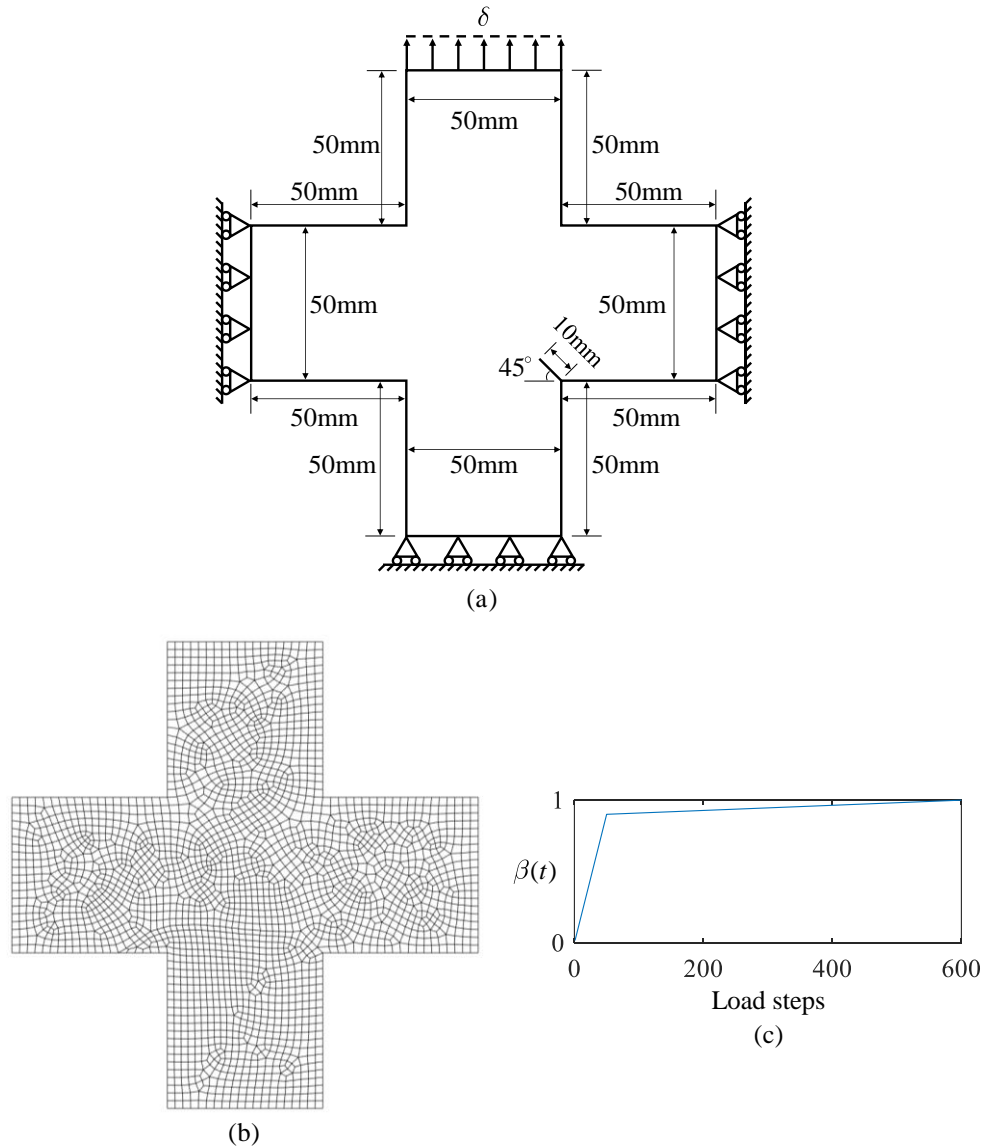


Fig. 6.14. Notched cruciform plate: (a) geometry and boundary conditions, (b) initial mesh geometry, and (c) load history curve.

The initial mesh geometry (2527 elements) shown in Fig. 6.14(b) is used. The prescribed displacement δ is applied until 0.0278 mm, the number of the total incremental load step is 600, and $\beta(t)$ is given in Fig. 6.14(c).

Adopting mesh coarsening, the mesh geometries and crack patterns formed during crack propagation are presented in Fig. 6.15. Fig. 6.16 shows the load-displacement curves obtained for the two analysis cases, in which the load is the total reaction force in the x -direction along the top edge. Fig. 6.17 shows the calculated crack path compared with the numerical results obtained by Hirshikesh et al. [79] and Mandal et al. [80]. The normalized computation times for the two analysis cases (Case 1 and Case 2) are listed in Table 6.3. The histories of the total number of

degrees of freedom required for two analysis cases are shown in Fig. 6.18. When mesh coarsening is employed, the computation time is reduced but there is almost no change in solutions.

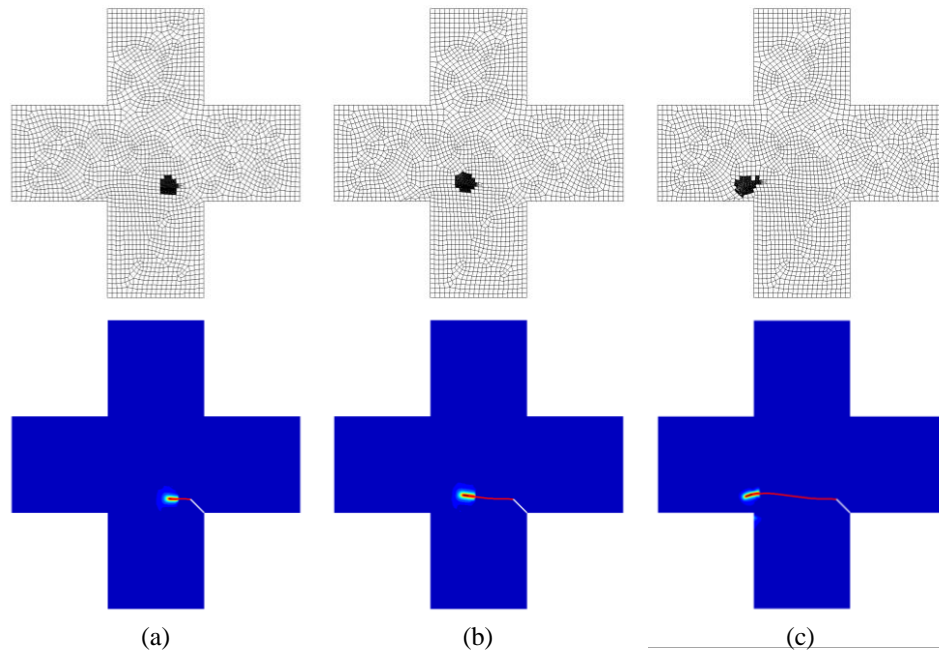


Fig. 6.15. Mesh geometries and crack patterns for the notched cruciform plate when (a) $\delta = 0.02625$ mm, (b) $\delta = 0.02645$ mm, and (c) $\delta = 0.02685$ mm.

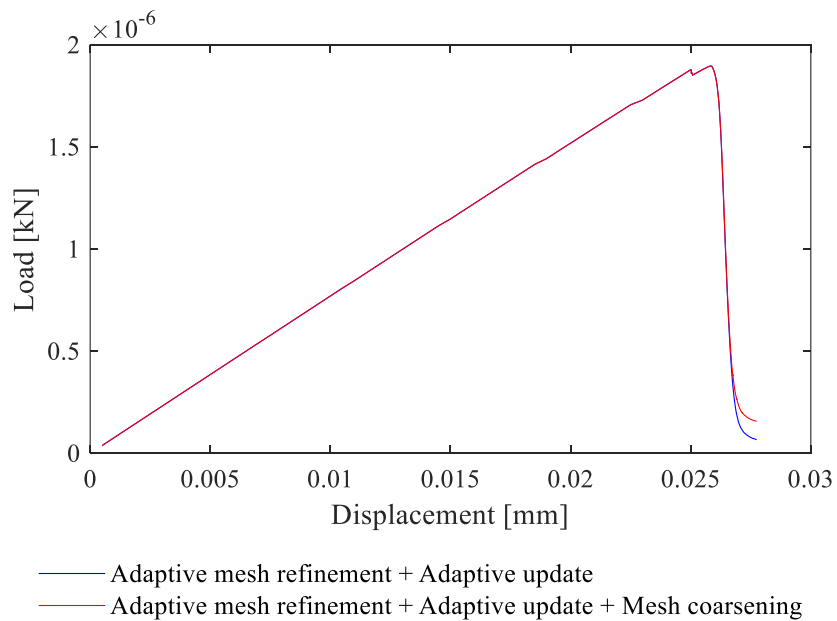


Fig. 6.16. Load-displacement curves on the notched cruciform plate.

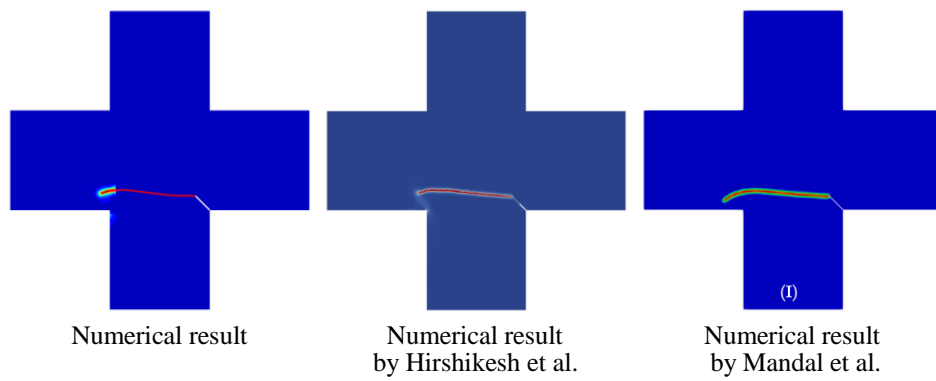


Fig. 6.17. Calculated crack path compared with the numerical results by Hirshikesh et al. [79] and Mandal et al. [80]. The numerical solution is obtained by mesh coarsening with the adaptive update and mesh refinement schemes.

Table 6.3. Normalized computation times required for the notched cruciform plate in Fig. 6.12. (Case 1) Adaptive mesh refinement + Adaptive update, (Case 2) Adaptive mesh refinement+ Adaptive update+ Mesh coarsening.

Cases	Whole time step		After crack propagation	
	Total	Equation solving	Total	Equation solving
Case 1	100 %	100 %	100 %	100 %
Case 2	77.86 %	65.83 %	69.62 %	56.13 %

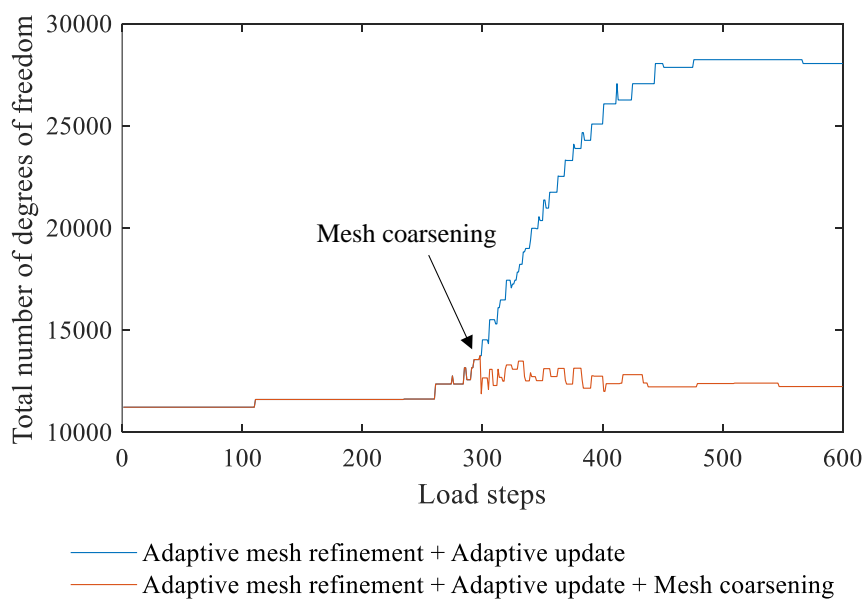


Fig. 6.18. Histories of the total number of degrees of freedom for the notched cruciform plate.

6.3.4. Double-edged notched tension problem

Finally, we consider a rectangular plate including two cracks as shown in Fig. 6.19(a). The bottom edge of the plate is fixed, and a vertical displacement is prescribed along the top edge of the plate. Young's modulus $E = 210$ GPa, Poisson's ratio $\nu = 0.3$, and the critical energy release rate $G_c = 2.7 \times 10^{-3}$ kN/mm. The regularization parameter and the radius to determine the near-tip domain are $l_0 = 0.025$ mm and $R_c = 0.25$ mm, respectively.

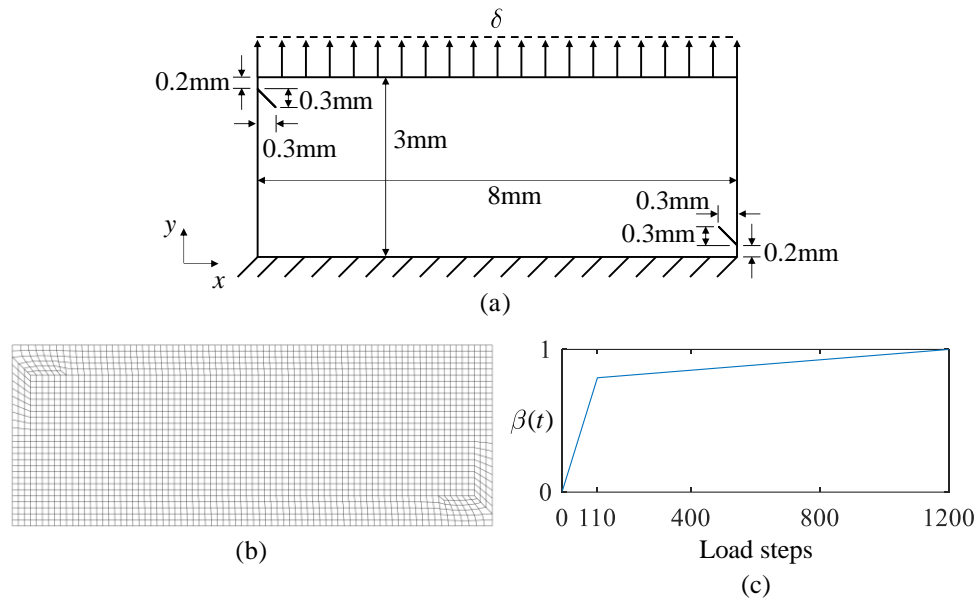


Fig. 6.19. Double-edged notched tension problem: (a) geometry and boundary conditions, (b) initial mesh geometry, and (c) load history curve.

The initial mesh geometry of 2392 elements used is shown in Fig. 6.19(b). For displacement control, δ increases up to 0.013725mm. We use 1200 incremental load steps with the load parameter function $\beta(t)$, see Fig. 6.19(c).

When mesh coarsening is employed, the mesh geometries and crack patterns are formed during crack propagation as shown in Fig. 6.20. Fig. 6.21 shows the load-displacement curves obtained for the two analysis cases, in which the load is the total reaction force in the y -direction along the top edge. Fig. 6.22 shows the calculated crack paths calculated for Case 1 and Case 2. The curves and crack paths are almost the same regardless of mesh coarsening.

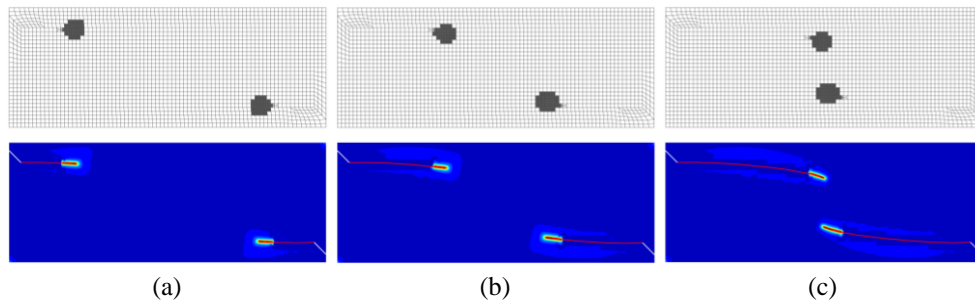


Fig. 6.20. Mesh geometries and crack patterns for the double-edged notched tension problem when (a) $\delta = 0.0121975$ mm, (b) $\delta = 0.0125225$ mm, and (c) $\delta = 0.0134725$ mm.

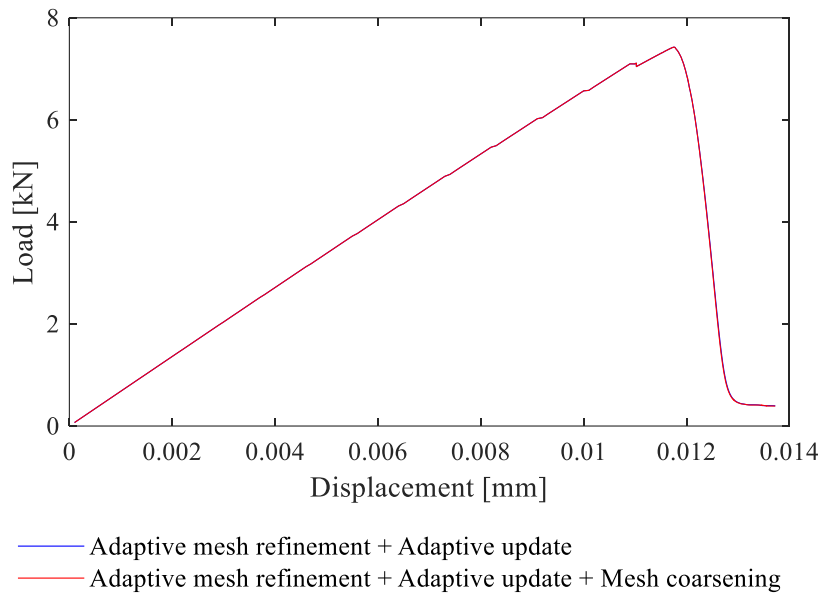


Fig. 6.21. Load-displacement curves on the double-edged notched tension problem.

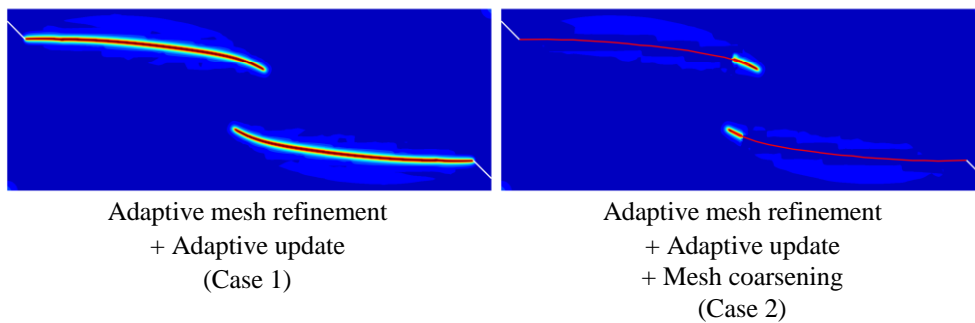


Fig. 6.22. Calculated crack paths in Case 1 (Adaptive mesh refinement + Adaptive update) and Case 2 (Adaptive mesh refinement + Adaptive update + Mesh coarsening).

The normalized computation times for the two analysis cases (Case 1 and Case 2) are listed in Table 6.4. The computation time is the most reduced among the numerical examples considered in this study. Table 6.5 shows computational times for five analysis cases: Case 1, Case 2 and three additional cases. The five cases are composed of combinations of 4 numerical schemes: local mesh refinement, adaptive mesh refinement, adaptive update, and mesh coarsening. The mesh geometries used for the local and adaptive mesh refinements are as shown in Fig. 6.23. The combination of the mesh coarsening, the adaptive mesh refinement scheme and the adaptive update scheme is the most effective.

Table 6.4. Normalized computation times required for the double notched tension problem in Fig. 6.19. (Case 1) Adaptive mesh refinement + Adaptive update, (Case 2) Adaptive mesh refinement+ Adaptive update+ Mesh coarsening.

Cases	Whole time step		After crack propagation	
	Total	Equation solving	Total	Equation solving
Case 1	100 %	100 %	100 %	100 %
Case 2	69.35 %	47.47 %	62.00 %	38.61 %

Table 6.5. Relative computation times for five analysis cases in the double-edged notched tension problem.

Combinations of numerical schemes applied	Ratio [%]
Local mesh refinement	100 %
Local mesh refinement + Adaptive update	73.54 %
Adaptive mesh refinement	21.10 %
Adaptive mesh refinement + Adaptive update (Case 1)	11.47 %
Adaptive mesh refinement + Adaptive update + Mesh coarsening (Case 2)	7.95 %

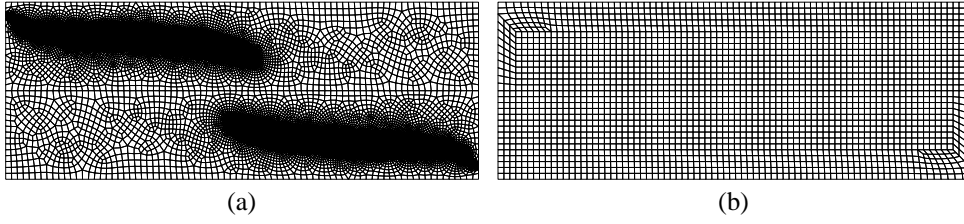


Fig. 6.23. Mesh geometries used for five analysis cases in Table 6.5: (a) the local mesh refinement and (b) the adaptive mesh refinement.

Chapter 7. Conclusions

In this dissertation, new numerical methods to improve the computational efficiency of the phase field model were proposed. Using a damage parameter as a nodal degree of freedom allows the model to easily handle complex crack behaviors without crack tracking algorithms. This is indeed the most advantageous feature of the phase field model. However, it requires an iterative procedure to solve nonlinear equations such as Newton-Raphson method, and mesh refinement to deal with high gradient values in the phase field transition zone, which largely increase the computational cost.

We firstly proposed the adaptive update scheme. The computational efficiency can be greatly improved without mesh refinement, and can be further improved when used in conjunction with the adaptive mesh refinement schemes. In this numerical scheme, the entire domain is divided into two domains: one near the crack tip and one far from the crack tip. Since structural properties such as stiffness, strain energy, and damage rarely vary in the domain far from the crack tip, those properties are occasionally updated in the iterative solution procedure. To maximize the computational efficiency, the local and adaptive mesh refinement schemes can be adopted together. The adaptive update scheme reduced computation time by 40% to 50% while maintaining the desired solution accuracy.

Secondly, the phantom-node method was applied to the phase field model to convert the fine mesh into the coarse mesh in the domain where a crack has already propagated. The mesh in the domain where a crack has already passed is still fine. To convert the fine mesh into the coarse mesh in that domain, we apply the phantom-node method, which is widely used [21- 22, 75-77]. In doing so, the total number of degrees of freedom is significantly reduced. Using the phantom-node method, it is possible to extend to 3D and shell problems. The adaptive mesh refinement scheme based on variable-node elements [48] is adopted in this study. To additionally improve the computational efficiency, the adaptive update scheme [48] is also employed.

In the future, implementation of the phase field model incorporated with the strain smoothing method [72] and enriched finite element method [73]. In addition, it is important to extend the 3D or shell problems [74].

Bibliography

- [1] A.A. Griffith, The phenomena of rupture and flow in solids, *Philos. Trans. R. Soc. London.* 221 (1920) 163–198.
- [2] G.R. Irwin, Analysis of stresses and strains near the end of a crack traversing a plate, *Trans. ASME, Ser. E, J, Appl. Mech.* 24 (1957) 361–364.
- [3] O.C. Zienkiewicz, R.L Taylor, *The Finite Element Method: Basic Formulation and Linear Problems*, McGraw-Hill, New York, NY (1989).
- [4] K.J. Bathe, *Finite Element Procedures*, Prentice Hall, Upper Saddle River, NJ (2006).
- [5] T.J.R. Hughes, *The Finite Element Method: Linear Static and Dynamic Finite Element Analysis*, Dover Publications, Mineola, NY (2000).
- [6] S.K. Chan, I.S. Tuba, W.K. Wilson, On the finite element method in linear fracture mechanics, *Eng. Fract. Mech.* 2 (1970) 1–17.
- [7] N. Levy, P. V. Marcal, W.J. Ostergren, J.R. Rice, Small scale yielding near a crack in plane strain: A finite element analysis, *Int. J. Fract. Mech.* 7 (1971) 143–156.
- [8] D.M. Tracey, Finite elements for determination of crack tip elastic stress intensity factors, *Eng. Fract. Mech.* 3 (1971) 255–265.
- [9] T. Pin, T.H.H. Pian, On the convergence of the finite element method for problems with singularity, *Int. J. Solids Struct.* 9 (1973) 313–321.
- [10] R.D. Henshell, K.G. Shaw, Crack tip finite elements are unnecessary, *Int. J. Numer. Methods Eng.* 9 (1975) 495–507.
- [11] R.S. Barsoum, On the use of isoparametric finite elements in linear fracture mechanics, *Int. J. Numer. Methods Eng.* 10 (1976) 25–37.

- [12] C.F. Shih, H.G. de Lorenzi, M.D. German, Crack extension modeling with singular quadratic isoparametric elements, *Int. J. Fract.* 12 (1976) 647–651.
- [13] R.S. Barsoum, Triangular quarter-point elements as elastic and perfectly-plastic crack tip elements, *Int. J. Numer. Methods Eng.* 11 (1977) 85–98.
- [14] T. Belytschko, L. Gu, Y.Y. Lu, Fracture and crack growth by element free Galerkin methods, *Model. Simul. Mater. Sci. Eng.* 2 (1994) 519–534.
- [15] T. Belytschko, Y.Y. Lu, L. Gu, Element-free Galerkin methods, *Int. J. Numer. Methods Eng.* 37 (1994) 229–256.
- [16] Y.Y. Lu, T. Belytschko, L. Gu, A new implementation of the element free Galerkin method, *Comput. Methods Appl. Mech. Engrg.* 113 (1994) 397–414.
- [17] T. Belytschko, T. Black, Elastic crack growth in finite elements with minimal remeshing, *Int. J. Numer. Methods Eng.* 45 (1999) 601–620.
- [18] N. Moës, J. Dolbow, T. Belytschko, A finite element method for crack growth without remeshing, *Int. J. Numer. Methods Eng.* 46 (1999) 131–150.
- [19] N. Sukumar, N. Moës, B. Moran, T. Belytschko, Extended finite element method for three-dimensional crack modelling, *Int. J. Numer. Methods Eng.* 48 (2000) 1549–1570.
- [20] J.H. Song, P.M.A. Areias, T. Belytschko, A method for dynamic crack and shear band propagation with phantom nodes, *Int. J. Numer. Methods Eng.* 67 (2006) 868–893.
- [21] T. Rabczuk, G. Zi, A. Gerstenberger, W.A. Wall, A new crack tip element for the phantom-node method with arbitrary cohesive cracks, *Int. J. Numer. Methods Eng.* 75 (2008) 577–599.
- [22] S.A. Silling, Reformulation of elasticity theory for discontinuities and long-range forces, *J. Mech. Phys. Solids.* 48 (2000) 175–209.
- [23] T. Rabczuk, T. Belytschko, Cracking particles: A simplified meshfree method for arbitrary evolving cracks, *Int. J. Numer. Methods Eng.* 61 (2004) 2316–2343.

- [24] G.A. Francfort, J.J. Marigo, Revisiting brittle fracture as an energy minimization problem, *J. Mech. Phys. Solids*. 46 (1998) 1319–1342.
- [25] B. Bourdin, G.A. Francfort, J.J. Marigo, Numerical experiments in revisited brittle fracture, *J. Mech. Phys. Solids*. 48 (2000) 797–826.
- [26] C. Kuhn, R. Müller, A phase field model for fracture, *Proc. Appl. Math. Mech.* 8 (2008) 10223–10224.
- [27] C. Miehe, M. Hofacker, F. Welschinger, A phase field model for rate-independent crack propagation: Robust algorithmic implementation based on operator splits, *Comput. Methods Appl. Mech. Eng.* 199 (2010) 2765–2778.
- [28] C. Miehe, F. Welschinger, M. Hofacker, Thermodynamically consistent phase-field models of fracture: Variational principles and multi-field FE implementations, *Int. J. Numer. Methods Eng.* 83 (2010) 1273–1311.
- [29] M. Ambati, T. Gerasimov, L. De Lorenzis, Phase-field modeling of ductile fracture, *Comput. Mech.* 55 (2015) 1017–1040.
- [30] M.J. Borden, C. V. Verhoosel, M.A. Scott, T.J.R. Hughes, C.M. Landis, A phase-field description of dynamic brittle fracture, *Comput. Methods Appl. Mech. Eng.* 217–220 (2012) 77–95.
- [31] T. Nguyen, D. Waldmann, T.Q. Bui, Computational chemo-thermo-mechanical coupling phase-field model for complex fracture induced by early-age shrinkage and hydration heat in cement-based materials, *Comput. Methods Appl. Mech. Eng.* 348 (2019) 1–28.
- [32] T.Q. Bui, X. Hu, A review of phase-field models, fundamentals and their applications to composite laminates, *Eng. Fract. Mech.* 248 (2021) 107705.
- [33] D.H. Doan, T.Q. Bui, N.D. Duc, K. Fushinobu, Hybrid phase field simulation of dynamic crack propagation in functionally graded glass-filled epoxy, *Compos. Part B Eng.* 99 (2016) 266–276.
- [34] D.H. Doan, T.Q. Bui, T. Van Do, N.D. Duc, A rate-dependent hybrid phase field model for dynamic crack propagation, *J. Appl. Phys.* 122 (2017).

- [35] H. Badnava, M.A. Msekh, E. Etemadi, T. Rabczuk, An h-adaptive thermo-mechanical phase field model for fracture, *Finite Elem. Anal. Des.* 138 (2018) 31–47.
- [36] S. Nagaraja, M. Elhaddad, M. Ambati, S. Kollmannsberger, L. De Lorenzis, E. Rank, Phase-field modeling of brittle fracture with multi-level hp-FEM and the finite cell method, *Comput. Mech.* 63 (2019) 1283–1300.
- [37] Hirshikesh, A.L.N. Pramod, R.K. Annabattula, E.T. Ooi, C. Song, S. Natarajan, Adaptive phase-field modeling of brittle fracture using the scaled boundary finite element method, *Comput. Methods Appl. Mech. Eng.* 355 (2019) 284–307.
- [38] R.U. Patil, B.K. Mishra, I. V. Singh, T.Q. Bui, A new multiscale phase field method to simulate failure in composites, *Adv. Eng. Softw.* 126 (2018) 9–33.
- [39] R.U. Patil, B.K. Mishra, I. V. Singh, An adaptive multiscale phase field method for brittle fracture, *Comput. Methods Appl. Mech. Eng.* 329 (2018) 254–288.
- [40] R.U. Patil, B.K. Mishra, I. V. Singh, A local moving extended phase field method (LMXPFM) for failure analysis of brittle materials, *Comput. Methods Appl. Mech. Eng.* 342 (2018) 674–709.
- [41] S. Goswami, C. Anitescu, T. Rabczuk, Adaptive phase field analysis with dual hierarchical meshes for brittle fracture, *Eng. Fract. Mech.* 218 (2019) 106608.
- [42] Hirshikesh, C. Jansari, K. Kannan, R.K. Annabattula, S. Natarajan, Adaptive phase field method for quasi-static brittle fracture using a recovery based error indicator and quadtree decomposition, *Eng. Fract. Mech.* 220 (2019) 106599.
- [43] F. Tian, X. Tang, T. Xu, J. Yang, L. Li, A hybrid adaptive finite element phase-field method for quasi-static and dynamic brittle fracture, *Int. J. Numer. Methods Eng.* 120 (2019) 1108–1125.
- [44] A. Muixí, S. Fernández-Méndez, A. Rodríguez-Ferran, Adaptive refinement for phase-field models of brittle fracture based on Nitsche’s method, *Comput. Mech.* 66 (2020) 69–85.
- [45] A. Muixí, A. Rodríguez-Ferran, S. Fernández-Méndez, A hybridizable discontinuous Galerkin phase-field model for brittle fracture with adaptive refinement, *Int. J. Numer. Methods Eng.* 121 (2020) 1147–1169.

- [46] A. Muixí, O. Marco, A. Rodríguez-Ferran, S. Fernández-Méndez, A combined XFEM phase-field computational model for crack growth without remeshing, *Comput. Mech.* 67 (2021) 231–249.
- [47] N. Noii, F. Aldakheel, T. Wick, P. Wriggers, An adaptive global-local approach for phase-field modeling of anisotropic brittle fracture, *Comput. Methods Appl. Mech. Eng.* 361 (2020) 112744.
- [48] G. Kim, P.S. Lee, Towards improving the computational efficiency of the phase field model, *Comput. Struct.* (2023), accepted.
- [49] T. Yu, T.Q. Bui, Numerical simulation of 2-D weak and strong discontinuities by a novel approach based on XFEM with local mesh refinement, *Comput. Struct.* 196 (2018) 112–133.
- [50] J.H. Lim, D. Sohn, J.H. Lee, S. Im, Variable-node finite elements with smoothed integration techniques and their applications for multiscale mechanics problems, *Comput. Struct.* 88 (2010) 413–425.
- [51] Y.S. Cho, S. Jun, S. Im, H.G. Kim, An improved interface element with variable nodes for non-matching finite element meshes, *Comput. Methods Appl. Mech. Eng.* 194 (2005) 3022–3046.
- [52] Y.S. Cho, S. Im, MLS-based variable-node elements compatible with quadratic interpolation. Part I: formulation and application for non-matching meshes, *Int. J. Numer. Methods Eng.* 65 (2006) 494–516.
- [53] Y.S. Cho, S. Im, MLS-based variable-node elements compatible with quadratic interpolation. Part II: application for finite crack element, *Int. J. Numer. Methods Eng.* 65 (2006) 517–547.
- [54] J.H. Lim, S. Im, Y.S. Cho, MLS (moving least square)-based finite elements for three-dimensional nonmatching meshes and adaptive mesh refinement, *Comput. Methods Appl. Mech. Eng.* 196 (2007) 2216–2228.
- [55] J.H. Lim, S. Im, Y.-S. Cho, Variable-node elements for non-matching meshes by means of MLS (moving least-square) scheme, *Int. J. Numer. Methods Eng.* 72 (2007) 835–857.
- [56] J.H. Lim, D. Sohn, S. Im, Variable-node element families for mesh connection and adaptive mesh computation, *Struct. Eng. Mech.* 43 (2012) 349–370.

- [57] L. Ambrosio, V.M. Tortorelli, Approximation of functional depending on jumps by elliptic functional via t -convergence, *Commun. Pure Appl. Math.* 43 (1990) 999–1036.
- [58] L. Ambrosio, V.M. Tortorelli, On the approximation of free discontinuity problems, *Boll. Unione Mat. Ital.* B (7) 6 (1) (1992) 105-123.
- [59] T. Linse, P. Hennig, M. Kästner, R. de Borst, A convergence study of phase-field models for brittle fracture, *Eng. Fract. Mech.* 184 (2017) 307–318.
- [60] M. Ambati, T. Gerasimov, L. De Lorenzis, A review on phase-field models of brittle fracture and a new fast hybrid formulation, *Comput. Mech.* 55 (2014) 383–405.
- [61] H. Amor, J.J. Marigo, C. Maurini, Regularized formulation of the variational brittle fracture with unilateral contact: Numerical experiments, *J. Mech. Phys. Solids.* 57 (2009) 1209–1229.
- [62] J. Storm, D. Supriatna, M. Kaliske, The concept of representative crack elements for phase-field fracture: Anisotropic elasticity and thermo-elasticity, *Int. J. Numer. Methods Eng.* 121 (2020) 779–805.
- [63] B. Yin, J. Storm, M. Kaliske, Viscoelastic phase-field fracture using the framework of representative crack elements, *Int. J. Fract.* (2021).
- [64] J. Storm, M. Kaliske, Phase-field Fracture with Representative Crack Elements for Non-linear Material Behaviour, *Pamm.* 20 (2021).
- [65] J. Storm, B. Yin, M. Kaliske, The concept of Representative Crack Elements (RCE) for phase-field fracture: transient thermo-mechanics, *Comput. Mech.* (2022).
- [66] S. May, J. Vignollet, R. De Borst, A numerical assessment of phase-field models for brittle and cohesive fracture: Γ -Convergence and stress oscillations, *Eur. J. Mech. ASolids.* 52 (2015) 72–84.
- [67] M. Strobl, T. Seelig, A novel treatment of crack boundary conditions in phase field models of fracture, *Pamm.* 15 (2015) 155–156.
- [68] A. Schlüter, Phase field modeling of dynamic brittle fracture, Dissertation, Technische Universität Kaiserslautern (2018).

- [69] C. Steinke, M. Kaliske, A phase-field crack model based on directional stress decomposition, *Comput. Mech.* 63 (2019) 1019–1046.
- [70] D. Sohn, J.H. Lim, S. Im, An efficient scheme for coupling dissimilar hexahedral meshes with the aid of variable-node transition elements, *Adv. Eng. Softw.* 65 (2013) 200–215.
- [71] B. Winkler, *Traglastuntersuchungen von unbewehrten und bewehrten Betonstrukturen auf der Grundlage eines objektiven Werkstoffgesetzes für Beton*, Dissertation, University of Innsbruck (2001).
- [72] C. Lee, P.S. Lee, A new strain smoothing method for triangular and tetrahedral finite elements, *Comput. Methods Appl. Mech. Eng.* 341 (2018) 939–955.
- [73] S. Kim, P.S. Lee, A new enriched 4-node 2D solid finite element free from the linear dependence problem, *Comput. Struct.* 202 (2018) 25–43.
- [74] Y. Ko, P.S. Lee, K.J. Bathe, The MITC4+ shell element and its performance, *Comput. Struct.* 169 (2016) 57–68.
- [75] A. Hansbo, P. Hansbo, A finite element method for the simulation of strong and weak discontinuities in solid mechanics, *Comput. Methods Appl. Mech. Eng.* 193 (2004) 3523–3540.
- [76] N. Vu-Bac, H. Nguyen-Xuan, L. Chen, C.K. Lee, G. Zi, X. Zhuang, G.R. Liu, T. Rabczuk, A phantom-node method with edge-based strain smoothing for linear elastic fracture mechanics, *J. Appl. Math.* 2013 (2013).
- [77] T. Chau-Dinh, G. Zi, P.S. Lee, T. Rabczuk, J.H. Song, Phantom-node method for shell models with arbitrary cracks, *Comput. Struct.* 92–93 (2012) 242–256.
- [78] N.N. V. Prasad, M.H. Aliabadi, D.P. Rooke, Incremental crack growth in thermoelastic problems, *Int. J. Fract.* 66 (1994) R45–R50.
- [79] Hirshikesh, S. Natarajan, R.K. Annabattula, A FEniCS implementation of the phase field method for quasi-static brittle fracture, *Front. Struct. Civ. Eng.* 13 (2019) 380–396.
- [80] T.K. Mandal, V.P. Nguyen, J.Y. Wu, C. Nguyen-Thanh, A. de Vaucorbeil, Fracture of thermo-elastic solids:

Phase-field modeling and new results with an efficient monolithic solver, *Comput. Methods Appl. Mech. Eng.* 376 (2021) 113648.

Appendix A. Phase field formulations

We here briefly review three phase field formulations [60]: Isotropic formulation, anisotropic formulation and hybrid formulation.

A.1. Isotropic formulation

The isotropic formulation is given as

$$\boldsymbol{\sigma} = [(1-\phi)^2 + k] \frac{\partial \psi_e(\boldsymbol{\epsilon})}{\partial \boldsymbol{\epsilon}}, \quad (\text{A.1})$$

$$\left[\frac{G_c}{l_0} + 2\psi_e \right] \phi - G_c l_0 \nabla \phi \cdot \nabla \phi = 2\psi_e, \quad (\text{A.2})$$

$$-l_0^2 \nabla \phi + \phi = \frac{2l_0}{G} (1-\phi) H, \quad (\text{A.3})$$

$$H(\mathbf{x}, t) = \max_{s \in [0, t]} \psi_e(\boldsymbol{\epsilon}(\mathbf{x}, s)), \quad (\text{A.4})$$

In this formulation, the entire degradation of the strain energy is adopted. This formulation is simple but has some limitation such as overestimated crack driving force, crack surface penetration and crack propagation at compression.

A.2. Anisotropic formulation

The anisotropic formulation is written as

$$\boldsymbol{\sigma} = [(1-\phi)^2 + k] \frac{\partial \psi_e^+(\boldsymbol{\epsilon})}{\partial \boldsymbol{\epsilon}} + \frac{\partial \psi_e^-(\boldsymbol{\epsilon})}{\partial \boldsymbol{\epsilon}}, \quad (\text{A.5})$$

$$\left[\frac{G_c}{l_0} + 2\psi_e^+ \right] \phi - G_c l_0 \nabla \phi \cdot \nabla \phi = 2\psi_e^+, \quad (\text{A.6})$$

$$-l_0^2 \nabla \phi + \phi = \frac{2l_0}{G} (1-\phi) H^+, \quad (\text{A.7})$$

$$H(\mathbf{x}, t) = \max_{s \in [0, t]} \psi_e^+(\boldsymbol{\epsilon}(\mathbf{x}, s)), \quad (\text{A.8})$$

In this formulation, the strain energy term is decomposed and the degradation is only applied on the split strain energy. This formulation has an issue of non-physical prediction [66, 67, 69] and additional studies have been performed [63, 65, 69].

A.3. Hybrid formulation

The hybrid formulation proposed by Ambati et al. [60] is a combination of splitting in crack evolution equation and not decomposing in the degradation function controlling the strain energy. The hybrid formulation is expressed as

$$\boldsymbol{\sigma} = [(1-\phi)^2 + k] \frac{\partial \psi_e(\boldsymbol{\varepsilon})}{\partial \boldsymbol{\varepsilon}}, \quad (\text{A.9})$$

$$\left[\frac{G_c}{l_0} + 2\psi_e^+ \right] \phi - G_c l_0 \nabla \phi \cdot \nabla \phi = 2\psi_e^+, \quad (\text{A.10})$$

$$-l_0^2 \nabla \phi + \phi = \frac{2l_0}{G} (1-\phi) H^+, \quad (\text{A.11})$$

$$H(\mathbf{x}, t) = \max_{s \in [0, t]} \psi_e^+(\boldsymbol{\varepsilon}(\mathbf{x}, s)), \quad (\text{A.12})$$

Appendix B. Patch test of variable-node finite elements

To apply adaptive mesh refinement scheme using variable-node finite elements to the phase field model, the performance of variable-node finite elements should be examined. For the use of variable-node finite elements, patch test of variable-node finite elements is performed. geometry and boundary condition of the patch test is given as shown in Fig. B.1(a). In Fig. B.1(a), 4-node quadrilateral finite elements and variable-node finite element are used in Ω_1 and Ω_2 , respectively. Young's modulus and Poisson's ratio are considered as 210×10^6 and 0.3, respectively. The mesh geometries for 11-node, 18-node and 25-node variable-node finite elements are shown in Fig. B.1(b), (c) and (d), respectively. Fig. B.2 shows the stress distribution (σ_{11}) of for 11-node, 18-node, 25-node variable-node finite elements. It is observed that variable-node finite elements pass the patch test.

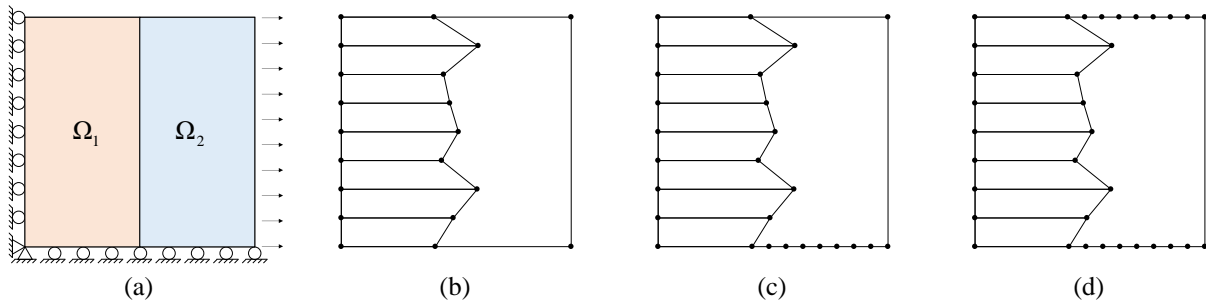


Fig. B.1. Patch test of variable-node finite elements: (a) geometry and boundary conditions and (b) mesh geometries for (b) 11-node, (c) 18-node and (d) 25-node variable-node finite elements.

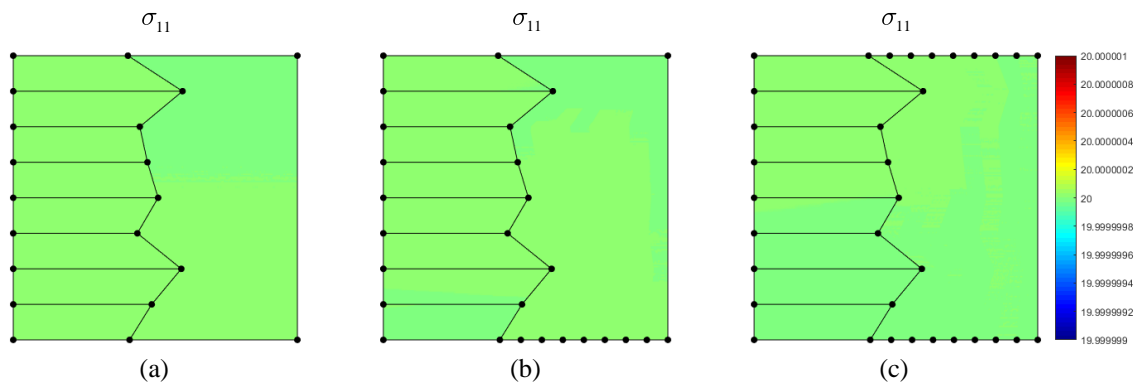


Fig. B.2. Stress distributions of the patch test for (a) 11-node, (b) 18-node and (c) 25-node variable-node finite elements.

Appendix C. Study on the update parameter

The adaptive update scheme proposed in this study needs the update criteria in Eq. (4.2). The computation time required for the adaptive update scheme varies depending on the update parameter η . To find the appropriate η , a parametric study is performed.

Computation times are measured through the numerical example described in Section 5.3.4 with varying η . The adaptive update scheme is adopted with the adaptive mesh refinement scheme. Table C.1 lists computation times required for seven different update parameters from 1.25 to 100. Fig. C.1 shows the load-displacement curves according to the update parameter η for the notched plate with three holes. The computation time is the shortest when $\eta = 10$ is used. Note that very similar solutions are obtained in all calculation cases.

Table C.1. Computation times required according to the update parameter η for the notched plate with three holes.

Update parameter η	Computation time [sec]
1.25	2438.45
2.5	2418.36
5	2391.33
10	2359.78
20	2472.99
50	2589.36
100	2668.58

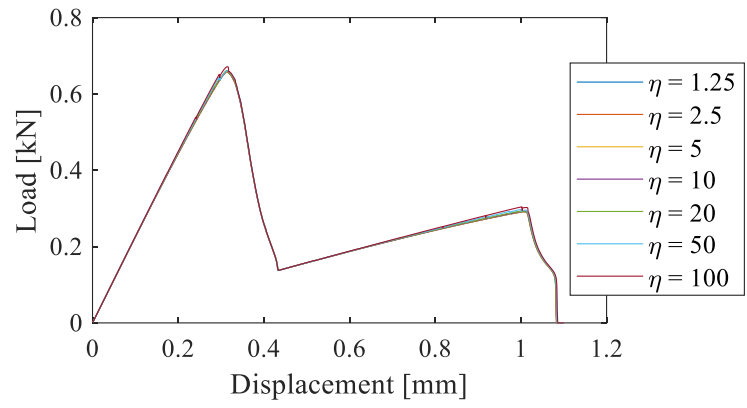


Fig. C.1. Load-displacement curves according to the update parameter η for the notched plate with three holes.

Appendix D. Study on the critical damage parameter in the case of crack initiation

The phase field model is based on a variational approach, in which a brittle fracture problem can be solved by minimizing the potential energy functional. The phase field model can be simulated without any additional criteria for when/where cracks initiate, grow, and how much and in what direction they propagate.

In the case of crack initiation, taking the critical damage parameter as $\phi_c = 0.5$ may give inaccurate solutions due to late identification of the crack initiation domain. To obtain an accurate solution, it is necessary to identify the crack initiation domain early. A parametric study must be performed to obtain appropriate ϕ_c in the case of crack initiation.

Load-displacement curves are plotted through the numerical example illustrated in Section 5.3.6 with varying ϕ_c . The proposed adaptive update scheme is adopted. Fig D.1 gives load-displacement curves for four different ϕ_c from 0.1 to 0.4 until the crack propagates. When $\phi_c = 0.1$ is used, the load-displacement curve is the most similar to the curve when fine meshes are preset in the crack initiation domain. Note that after the crack initiation domain is identified, the critical damage parameter is taken as $\phi_c = 0.5$ again.

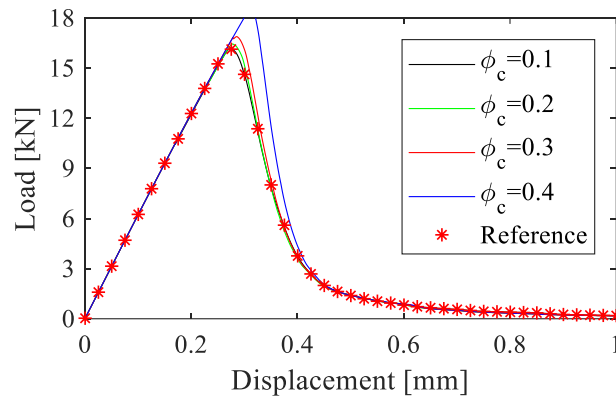


Fig. D.1. Load-displacement curves for the L-shaped panel for four different ϕ_c from 0.1 to 0.4.